Politecnico di Torino

Politecnico di Torino

Corso di Laurea Magistrale in Ingegneria Aerospaziale

A.a. 2024/2025

Sessione di laurea: 11 Dicembre 2025

Stability and Control Analysis of a Hypersonic Re-entry Vehicle

Relatori:

Elisa Capello

Christophe Roux

Candidato:

Vincenzo Gullo

The research presented in this thesis was carried out in collaboration with Avio S.p.A., within the framework of an industrial–academic study on hypersonic re-entry vehicle dynamics and control.

La ricerca descritta in questa tesi è stata svolta in collaborazione con Avio S.p.A., nell'ambito di uno studio congiunto tra mondo accademico e industriale sulla dinamica e il controllo di velivoli ipersonici da rientro.

Ringraziamenti

Grazie,

A mia madre Marcella per non essersi mai accontentata e avermi spinto oltre,

A mio padre Donato per avermi sempre compreso e compatito,

A mia sorella Luisa per aver sempre gioito di ogni mio traguardo,

A zia Maria, Angela e Ferdinando per avermi sempre fatto sentire a casa,

A Spezzano e gli amici che ci trovo per avermi regalato spensieratezza e leggerezza in ogni vacanza,

A Domenico spalla destra nella vita e in questa avventura,

A Nikita compagno di risate e di avventure tra i banchi del politecnico,

A Emanuela per aver camminato insieme a me in questo percorso, per tutte le cure, per tutto l'amore e per tutte le carezze.

«And more, much more than this, i did it my way»

Abstract

In this thesis the stability and control of HORUS2B, a winged hypersonic re-entry vehicle, are analysed along a nominal trajectory reconstructed by digitalising a reference mission profile. The full nonlinear 6-DOF model is linearised along the trajectory and represented as a sequence of LTI systems; pitch equilibrium is ensured by a trim law based on the body flap and, when required, symmetric elevon deflection. Open-loop eigenvalue and eigenvector analysis is used to track the evolution of the characteristic modes (short period, phugoid, lateral oscillation and aperiodic modes) and shows good qualitative and quantitative agreement with classical reference results.

A central, original contribution of this work is the application of literal (closed-form) approximations to this type of hypersonic lifting vehicle and flight regime. These approximations are used to interpret the parametric dependence of the longitudinal and lateral–directional modes, and in particular to demonstrate that the dynamics can be captured with good accuracy even when aerodynamic damping derivatives are set to zero, so that the modal damping can be used to back out the missing damping derivatives. For the lateral–directional dynamics, the Bihrle–Weissman diagram is constructed by computing the dynamic directional stability parameter and the LCDP along the trajectory. The resulting loci indicate lateral instability over significant flight segments and are consistent with the need to employ the reaction-control system (RCS) to initiate and complete the required manoeuvres.

In the final part of the thesis a LQR attitude controller is designed along the reference trajectory to stabilise the critical modes and improve lateral–directional coordination. Although the controller is synthesised for attitude and angular-rate regulation, its impact on the full 6-DOF motion is assessed through nonlinear simulations. The resulting vehicle ground track shows that the controlled vehicle reaches the vicinity of Kourou, meeting the end-of-mission objective of the adopted reference scenario.

Sommario

In questa tesi si studiano la stabilità e il controllo di HORUS2B, un velivolo alato per il rientro ipersonico, lungo una traiettoria nominale ottenuta digitalizzando (OCR) un profilo di missione di riferimento. Il modello non lineare completo a sei gradi di libertà viene linearizzato lungo la traiettoria e descritto come una sequenza di sistemi LTI; l'equilibrio in beccheggio è garantito da una legge di trim che utilizza il body flap e, quando necessario (saturazione bodyflap), una deflessione simmetrica degli elevon. L'analisi in open loop degli autovalori e degli autovettori consente di seguire l'evoluzione dei modi caratteristici (short period, phugoid, oscillazione laterale e modi aperiodici), mostrando una buona coerenza qualitativa e quantitativa con i risultati classici disponibili in letteratura.

L'aspetto più originale del lavoro è l'impiego di approssimazioni letterali (in forma chiusa) per descrivere il comportamento dinamico di un velivolo ipersonico alare in questo specifico regime di volo. Tali approssimazioni vengono sfruttate per interpretare la dipendenza parametrica dei modi longitudinali e latero–direzionali e, in particolare, per mostrare che la dinamica può essere ricostruita con buona accuratezza anche ponendo a zero le derivate aerodinamiche di smorzamento, utilizzando lo smorzamento modale per ricavare a posteriori le derivate mancanti. Per la dinamica latero–direzionale viene inoltre costruito il diagramma di Bihrle–Weissman, calcolando lungo la traiettoria il parametro di stabilità direzionale dinamica e l'LCDP. I risultati ottenuti evidenziano instabilità laterale in porzioni significative del volo e risultano coerenti con la necessità di impiegare il Reaction Control System (RCS) per avviare e completare le manovre richieste.

Nella parte finale della tesi viene progettato un controllore LQR d'assetto, schedulato lungo la traiettoria di riferimento, con l'obiettivo di stabilizzare i modi critici e migliorare la coordinazione latero–direzionale. Sebbene il controllore sia progettato per la regolazione dell'assetto e delle velocità angolari, il suo effetto sull'intero moto a sei gradi di libertà viene analizzato tramite simulazioni non lineari. Il ground track risultante mostra che il velivolo controllato raggiunge le vicinanze di Kourou, soddisfacendo l'obiettivo finale di missione dello scenario di riferimento adottato.

Indice

Elenco delle figure

Capitolo 1

Introduction

Hypersonic flight refers to atmospheric flight at extremely high speeds, conventionally defined as Mach 5 or higher, i.e. more than five times the local speed of sound around (1,225–1,235 km/h at sea level under standard conditions). Although this threshold is somewhat arbitrary, it marks the onset of a regime in which strong shock waves, extreme aerodynamic heating, and real-gas effects dominate the physics of flight. In this regime, the flow becomes highly compressible, boundary-layer transition and separation play a crucial role, and the aerodynamic forces are strongly coupled with the thermal and structural response of the vehicle.

This type of flight is being actively developed both to drastically reduce global travel times—through concepts such as hypersonic transport and reusable spaceplanes—and for military applications, including hypersonic cruise missiles and boost-glide vehicles. The main technical challenges go far beyond simply "flying faster": they include the development of suitable propulsion systems (e.g. rocket engines, air-breathing scramjets) and the management of the very high temperatures generated by aerodynamic heating, which can severely affect both the internal structure and the external thermal protection system (TPS).

From a systems point of view, hypersonic vehicles require a genuinely integrated design approach. Aerothermodynamics, flight mechanics, guidance and control, and TPS design cannot be treated as independent disciplines, because design choices in one area have immediate consequences in the others. For example, the shaping of the re-entry trajectory to satisfy flight-mechanics and guidance requirements directly determines the heat load on the structure; the layout and sizing of control surfaces must ensure not only sufficient control authority, but also acceptable thermal and mechanical loads; TPS thickness and materials, in turn, influence the mass distribution and thus the vehicle's stability characteristics. This tight coupling makes the analysis, design, and operation of hypersonic vehicles particularly challenging and motivates the development of unified frameworks capable of capturing these interactions.

1.1 Reference vehicles

The development of hypersonic vehicles has a long history. Early experimental programmes such as the X-15 provided the first systematic exploration of controlled, crewed flight at hypersonic speeds. The X-15, a rocket-powered research aircraft, routinely flew above Mach 6 and reached altitudes at the edge of space, generating invaluable data on aerothermodynamics, stability and control, and structural loads in extreme flight conditions.[1] «In general, the X-15 (Fig.1.1) had solid aerodynamic stability and control. The aircraft had positive directional stability at all speeds and attitudes; it also always had a stable Dutch Roll mode; pilot comments were all favorable. At high true airspeed, aerodynamic damping would diminish; making the use of a "stability augmentation system" to provide synthetic damping desirable. On Flight 191, where that system failed in a manner where it destabilized the aircraft, the aircraft lost control, overstressed its structure, and disintegrated mid-air killing pilot Michael Adams.»[1]

Figura 1.1: North American X-15

A major step change came with the Space Shuttle Orbiter (Fig.1.2), the first operational reusable hypersonic vehicle. The Shuttle was designed to perform an orbital mission, survive atmospheric re-entry, and execute a precision landing on a runway. Its mission profile involved de-orbit from low Earth orbit, hypersonic entry with large cross-range capability to reach alternate landing sites, a long supersonic and transonic glide, and a final flare and touchdown. Despite its success, the Shuttle also highlighted several limitations of first-generation reusable hypersonic design. The aerodynamic configuration exhibited strong coupling between longitudinal and lateral-directional dynamics, making the design and validation of guidance and control laws particularly demanding. The need to rely on RCS jets deep into the atmosphere, where their use is undesirable from both operational and structural-load perspectives, reflected the challenges of maintaining sufficient control authority

Figura 1.2: Space Shuttle

and stability margins over the full entry trajectory.[1]

In the last two decades, the focus has therefore shifted from Shuttle-era concepts to a new generation of reusable hypersonic vehicles and lifting re-entry demonstrators. Programmes such as **Space Rider** (Fig.1.3) embody a different design philosophy: smaller, uncrewed, with more integrated and automated guidance, navigation, and control (GNC), and with a stronger emphasis on operability and cost-effective reusability.

Figura 1.3: Space Rider

In this thesis, the HORUS-2B configuration is adopted as the reference hypersonic vehicle.[2] Building on the work carried out of Prof. Erwin Mooij, HORUS-2B is documented by an extensive benchmark data set, including aerodynamics, mass properties, nominal re-entry trajectory and GNC architecture, which provides sufficient fidelity and coverage to support detailed analyses and numerical simulations.

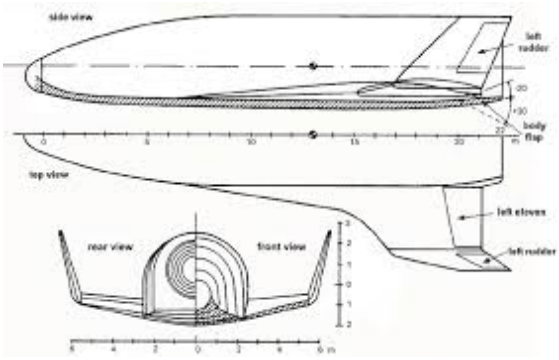

Figura 1.4: The Horus2B reference vehicle

1.2 Thesis objectives and contributions

In this thesis, the first step is the analysis of the **open-loop stability** of the reference vehicle, in line with previous studies by Mooij[3][4]. The objective is to identify and characterise the main dynamic modes along the reference re-entry trajectory and to determine the flight conditions at which the vehicle becomes dynamically critical.

The **original contribution** of this work is the implementation and assessment of **literal (closed-form) approximations** of the dynamic modes available in the literature, tailored to this specific configuration and hypersonic flight regime. These approximations are derived, adapted and compared against the "exact" linearised models along the trajectory in order to evaluate their accuracy, range of validity and practical usefulness for the preliminary design and stability assessment of Shuttle-class, Space-Rider-class vehicles such as HORUS-2B.

In the final part of the thesis, an **LQR-based attitude controller** is designed for the reference vehicle, following the general control architecture already proposed by Mooij[3] but adopting an alternative tuning and scheduling of the controller gains. Although the controller explicitly acts only on the attitude dynamics, its effects are analysed within a **full 6-DOF simulation framework**. In particular, the resulting vehicle ground track is examined, showing that the controlled vehicle reaches the vicinity of Kourou, which is the terminal objective of the reference mission. This allows the attitude-control study to be consistently interpreted in terms of its implications for the overall trajectory and mission performance.

Capitolo 2

Mathematical Model

This chapter presents the flight-mechanics framework adopted in this work. First, the reference frames and associated kinematic quantities used to describe the vehicle motion are introduced, together with the notation and sign conventions. On this basis, the complete set of nonlinear equations of motion is formulated in a consistent manner and expressed in a form suitable for subsequent trajectory, stability, and control analyses. All the frames definitions are referred to Mooij[3].

2.1 Reference Frames

Inertial Planetocentric Reference Frame, Index I

The inertial reference frame $\mathcal{F}_\mathcal{I}$ is defined with its origin at the centre of mass of the central body. Its $X_I Y_I$ plane coincides with the equatorial plane, while the Z_I-axis is aligned with the rotation axis of the central body and oriented north. The X_I-axis is fixed by the reference meridian at zero longitude and zero time, and the Y_I-axis is chosen so that the triad forms a right-handed coordinate system.

Rotating Planetocentric Reference Frame, Index R

The rotating planetocentric frame, $\mathcal{F}_R$, is attached to the central body and coincides with $\mathcal{F}_I$ at the initial time (and again after each complete revolution of the body). The Z_R-axis points towards the north, the X_R-axis lies on the equator at zero longitude, and the Y_R-axis is chosen to complete a right-handed triad.

Body Reference Frame, Index B

The body frame, $\mathcal{F}_\mathcal{B}$, is rigidly attached to the vehicle. The X_B-axis lies in

the symmetry plane and points forward, while the Z_B-axis also lies in the symmetry plane and points downward. The Y_B-axis is chosen such that the triad forms a right-handed coordinate system.

Trajectory Reference Frame (Groundspeed Based), Index TG

The axes of $\mathcal{F}_{TG}$ are defined as follows: the X_{TG}-axis is aligned with the velocity vector relative to $\mathcal{F}_R$; the Z_{TG}-axis lies in the vertical plane and is directed downward; the Y_{TG}-axis is chosen to complete a right-handed coordinate system.

Trajectory Reference Frame (Airspeed Based), Index TA

The axes of the airspeed-based trajectory frame, $\mathcal{F}_{TA}$, are defined analogously to those of $\mathcal{F}_{TG}$, with a single essential difference. The X_{TA}-axis is now aligned with the velocity vector relative to the atmosphere (airspeed) instead of the groundspeed. Consequently, the absolute orientation of the Y_{TA}- and Z_{TA}-axes changes, although their definition remains unchanged: the Z_{TA}-axis lies in the vertical plane and points downward, and the Y_{TA}-axis completes a right-handed coordinate system.

2.2 State-Variable Definitions

2.2.1 Position and Velocity

The state of the vehicle is described by its position and velocity vectors, which in principle may be expressed in different coordinate systems. Although classical orbital elements are widely used in orbital mechanics, they are not employed in the present work. Instead, position and velocity are represented exclusively in spherical coordinates, so that the state is written in terms of radius and angular components within the previously and following reference frames.

Spherical Components

With spherical components, position and velocity (here defined with respect to $\mathcal{F}_R$) are written as (Fig.2.1):

$$\text{Position}: \ R,\ \tau,\ \delta, \quad \text{Velocity}: V_g,\ \gamma_g,\ \chi_g.$$

The longitude τ is measured positively to the east, with $0° \leq \tau < 360°$. The latitude δ is measured along the meridian starting at the equator, positive towards the north and negative towards the south, so that $-90° \leq \delta \leq 90°$. The distance R

denotes the separation between the centre of mass of the central body and that of the vehicle. The groundspeed V_g is the magnitude of the velocity vector $\vec{V}$ relative to the rotating planetocentric frame. The flight–path angle γ_g is the angle between $\vec{V}$ and the local horizontal plane; it ranges from $-90°$ to $+90°$ and is negative when $\vec{V}$ is below the local horizon. The heading χ_g specifies the direction of the projection of $\vec{V}$ onto the local horizontal plane with respect to the local north and ranges from $-180°$ to $+180°$. For $\chi_g = +90°$, the vehicle moves parallel to the equator towards the east.

2.2.2 Attitude and angular rates

Attitude

The attitude of a vehicle, or in more mathematical terms, the orientation of a body fixed reference frame with respect to another one, can be expressed in several ways. Here, we restrict ourselves to one definition, which will be used along the thesis (Fig.2.2):

Aerodynamic angles are defined as the angle of attack α, the sideslip angle β, and the bank angle σ. The angle of attack α satisfies $-180° \leq \alpha < 180°$ and is positive for a nose–up attitude. The sideslip angle β satisfies $-90° \leq \beta \leq 90°$ and is positive for a nose–left attitude. The bank angle σ satisfies $-180° \leq \sigma < 180°$ and is positive for a bank to the right. When these angles are used in the equations of motion, they describe the attitude of the vehicle with respect to the groundspeed and carry the subscript g. Alternatively, they may be defined with respect to the airspeed, in which case the subscript a is used. The triplet α, β, and σ forms a set of Euler angles corresponding to a Type–1 rotation sequence[3] with order 2–3–1.

Angular rates

The body angular rate is defined as the angular velocity of the body frame with respect to the inertial frame, expressed in components along the body axes. The angular–velocity vector $\boldsymbol{\omega}$ is therefore composed of the roll rate p, the pitch rate q, and the yaw rate r (see Fig.2.3).

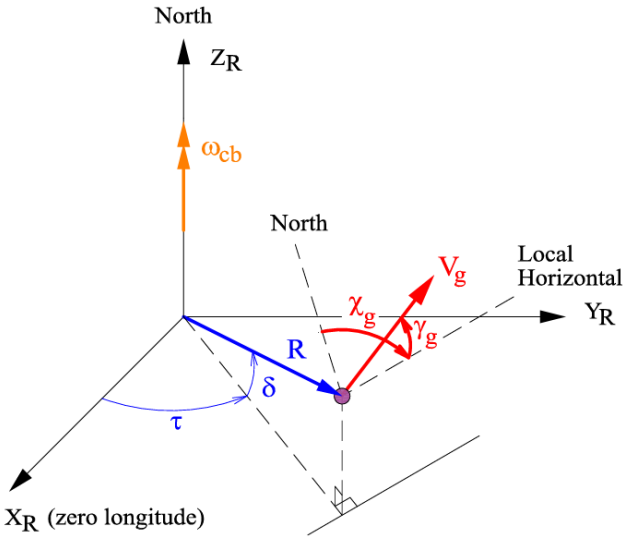

Figura 2.1: Definition of the six spherical flight parameters, the position (R, τ, δ) and velocity (V_g, γ_g, χ_g). Here, both τ, δ, γ_g and χ_g are positive[3]

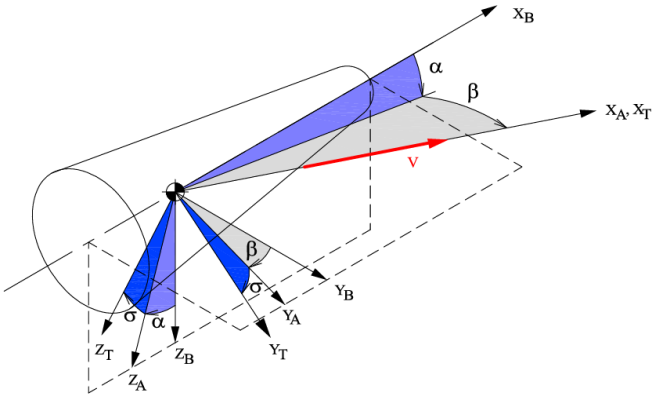

Figura 2.2: Definition of the aerodynamic attitude angles α, β and σ. The three related reference frames are the body frame (index B), the aerodynamic frame (index A) and the trajectory frame (index T). Here, both α, β and σ are positive.[3]

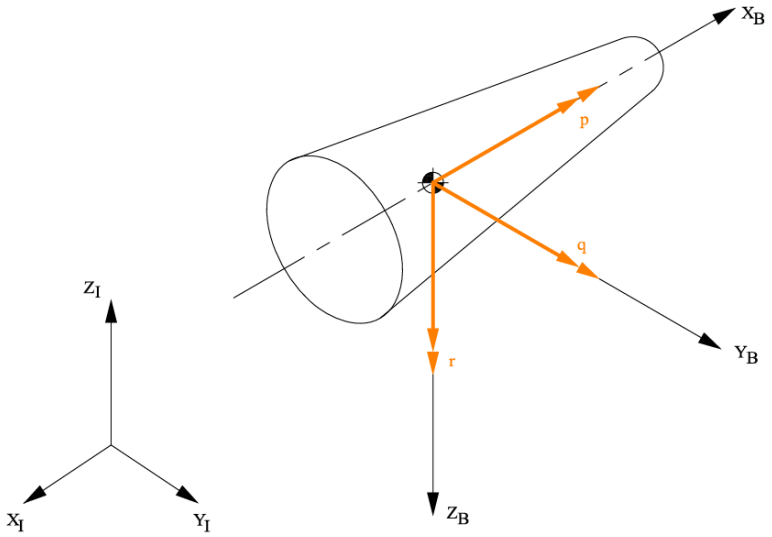

Figura 2.3: Definition of the angular rate of the vehicle, $\omega = (p, q, r)^T$. Relevant frames are $\mathcal{F}_I$, which has its origin in the c.o.m. of the central body, and the body-fixed frame $\mathcal{F}_B$, with its origin in the c.o.m. of the vehicle[3]

2.3 Equations of motion

At this point the equations of motion can be formulated. A complete derivation is beyond the scope of this thesis, and the interested reader is referred to [3][5] for details. The first step is the choice of state variables, which may be taken, for example, as Cartesian or spherical position and velocity components, or a suitable combination of both. In re-entry studies it is common to employ either inertial Cartesian position and velocity, or spherical position and velocity components in the rotating planetocentric frame $\mathcal{F}_R$. Since the latter choice greatly facilitates the physical interpretation of the results, it is adopted here as the basis for the subsequent linearisation, although its full derivation is rather lengthy and will not be repeated.

In the previous section the translational state variables have been introduced. The position is given by the distance R, longitude τ and latitude δ, while the velocity is described by its magnitude V and two direction angles, namely the flight–path angle γ and the heading χ. Because wind is neglected, no distinction between airspeed- and groundspeed-based quantities is required.

For the rotational motion, the Euler equations are employed. The vehicle is assumed to possess a plane of mass symmetry (the $X_B Y_B$-plane), implying $I_{xy} = I_{yz} = 0$. Instead of the classical Euler angles ϕ, θ and ψ, the attitude is parameterised by the aerodynamic angles: angle of attack α, sideslip angle β, and bank angle σ. These are, in principle, defined with respect to the groundspeed direction, but in the absence of wind they coincide with their airspeed-based counterparts (no subscript is added to differentiate between air- and groundspeed). The angular rate of the body is defined as the angular velocity of the body frame with respect to the inertial frame, resolved along the body axes; its components are the roll rate p, pitch rate q, and yaw rate r.

Summarising, the nonlinear dynamic equations of translational motion can be written as

$$\dot{V} = -\frac{D}{m} - g\sin\gamma + \omega_{cb}^2 R\cos\delta\left(\sin\gamma\cos\delta - \cos\gamma\sin\delta\cos\chi\right), \tag{2.1}$$

$$\begin{aligned} V\dot{\gamma} = {} & \frac{L\cos\sigma}{m} - g\cos\gamma + +2\omega_{cb}V\cos\delta\sin\chi + \frac{V^2}{R}\cos\gamma \\ & + \omega_{cb}^2 R\cos\delta\left(\cos\delta\cos\gamma + \sin\gamma\sin\delta\cos\chi\right), \end{aligned} \tag{2.2}$$

$$\begin{aligned} V\cos\gamma\,\dot{\chi} = {} & \frac{L\sin\sigma}{m} + 2\omega_{cb}V\left(\sin\delta\cos\gamma - \cos\delta\sin\gamma\cos\chi\right) + \frac{V^2}{R}\cos^2\gamma\tan\delta\sin\chi \\ & + \omega_{cb}^2 R\cos\delta\sin\delta\sin\chi. \end{aligned} \tag{2.3}$$

whereas the kinematic position equations are given by

$$\dot{R} = \dot{h} = V \sin\gamma, \tag{2.4}$$

$$\dot{\tau} = \frac{V \sin\chi \cos\gamma}{R \cos\delta}, \tag{2.5}$$

$$\dot{\delta} = \frac{V \cos\chi \cos\gamma}{R}. \tag{2.6}$$

The Euler equations of rotational motion are defined by:

$$\dot{\boldsymbol{\omega}} = \mathbf{I}^{-1}\left(\tilde{\boldsymbol{M}}_{\mathrm{cm}} - \boldsymbol{\omega} \times \mathbf{I}\boldsymbol{\omega}\right), \tag{2.7}$$

with

$$\tilde{\boldsymbol{M}}_{\mathrm{cm}} = (M_x,\, M_y,\, M_z)^{\mathrm{T}}$$

sum of external, Coriolis and relative moments about the c.o.m.,

$$\boldsymbol{I} = \begin{bmatrix} I_{xx} & -I_{xy} & -I_{xz} \\ -I_{xy} & I_{yy} & -I_{yz} \\ -I_{xz} & -I_{yz} & I_{zz} \end{bmatrix}$$

inertia tensor of the re-entry vehicle, referenced to the body frame,

$$\boldsymbol{\omega} = (p,\, q,\, r)^{\mathrm{T}}$$

rotation vector of the body frame w.r.t. the inertial frame, expressed in components along the body axes.
Solving the above equations formally requires the inversion of the inertia tensor. Writing the solution explicitly in terms of the body–rate derivatives, e.g. $\dot{p} = \ldots$, is algebraically tedious. Closed-form analytical expressions for $\dot{p}$, $\dot{q}$ and $\dot{r}$ can be found in the literature. In many practical cases, however, Eq.2.7 can be simplified so that the resulting equations are straightforward to use. This is true, for instance, for a mass-symmetric vehicle, which is the case for the winged re-entry configuration considered here, where two of the three products of inertia vanish. If the plane of symmetry is the $X_B Z_B$-plane, one has $I_{xy} = I_{yz} = 0$, and Eq.2.7 simplifies to

$$\begin{bmatrix} I_{xx} & 0 & -I_{xz} \\ 0 & I_{yy} & 0 \\ -I_{xz} & 0 & I_{zz} \end{bmatrix} \begin{pmatrix} \dot{p} \\ \dot{q} \\ \dot{r} \end{pmatrix} = \begin{pmatrix} M_x \\ M_y \\ M_z \end{pmatrix} - \begin{pmatrix} p \\ q \\ r \end{pmatrix} \times \begin{bmatrix} I_{xx} & 0 & -I_{xz} \\ 0 & I_{yy} & 0 \\ -I_{xz} & 0 & I_{zz} \end{bmatrix} \begin{pmatrix} p \\ q \\ r \end{pmatrix} \tag{2.8}$$

Solving this system of equations for $\dot{p}$, $\dot{q}$ and $\dot{r}$ leads to

$$\dot{p} = \frac{I_{zz}}{I^*} M_x + \frac{I_{xz}}{I^*} M_z + \frac{(I_{xx} - I_{yy} + I_{zz}) I_{xz}}{I^*} pq + \frac{(I_{yy} - I_{zz}) I_{zz} - I_{xz}^2}{I^*} qr, \tag{2.9}$$

$$\dot{q} = \frac{M_y}{I_{yy}} + \frac{I_{xz}}{I_{yy}} \left(r^2 - p^2\right) + \frac{I_{zz} - I_{xx}}{I_{yy}} pr, \tag{2.10}$$

$$\dot{r} = \frac{I_{xz}}{I^*} M_x + \frac{I_{xx}}{I^*} M_z + \frac{(I_{xx} - I_{yy}) I_{xx} + I_{xz}^2}{I^*} pq + \frac{(-I_{xx} + I_{yy} - I_{zz}) I_{xz}}{I^*} qr \tag{2.11}$$

with $I^* = I_{xx} I_{zz} - I_{xz}^2$.

Finally, the kinematic attitude equations are given by[3]

$$\begin{aligned} \dot{\alpha} \cos\beta = & -p \cos\alpha \sin\beta + q \cos\beta - r \sin\alpha \sin\beta \\ & + \sin\sigma \Big[\dot{\chi} \cos\gamma - \dot{\delta} \sin\chi \sin\gamma + (\dot{\tau} + \omega_{cb})(\cos\delta \cos\chi \sin\gamma - \sin\delta \cos\gamma)\Big] \\ & - \cos\sigma \Big[\dot{\gamma} - \dot{\delta} \cos\chi - (\dot{\tau} + \omega_{cb}) \cos\delta \sin\chi\Big], \end{aligned} \tag{2.12}$$

$$\begin{aligned} \dot{\beta} = & \; p \sin\alpha - r \cos\alpha \\ & + \sin\sigma \Big[\dot{\gamma} - \dot{\delta} \cos\chi - (\dot{\tau} + \omega_{cb}) \cos\delta \sin\chi\Big] \\ & + \cos\sigma \Big[\dot{\chi} \cos\gamma - \dot{\delta} \sin\chi \sin\gamma + (\dot{\tau} + \omega_{cb})(\cos\delta \cos\chi \sin\gamma - \sin\delta \cos\gamma)\Big], \end{aligned} \tag{2.13}$$

$$\begin{aligned} \dot{\sigma} = & -p \cos\alpha \cos\beta - q \sin\beta - r \sin\alpha \cos\beta \\ & + \dot{\alpha} \sin\beta - \dot{\chi} \sin\gamma - \dot{\delta} \sin\chi \cos\gamma + (\dot{\tau} + \omega_{cb})(\cos\delta \cos\chi \cos\gamma + \sin\delta \sin\gamma). \end{aligned} \tag{2.14}$$

At this stage, the equations of motion relevant to this thesis have been established. In the next chapter they will be subjected to suitable assumptions and simplifications and used as the basis for the linearisation and eigenmotion analysis. The complete nonlinear set, without any simplifications, will instead be employed in Chapter 5 for the numerical simulations and for the validation of the obtained results.

Capitolo 3

Open-loop behaviour of the re-entry vehicle

An important reference for the study of re-entry vehicle dynamics and control is the work of E. Mooij at Delft University of Technology[3]. This framework provides the foundation for interpreting the dynamic response of the vehicle in terms of physically meaningful motions.

3.1 Introduction

The open-loop analysis characterizes the vehicle's free response about a nominal trajectory. In this section, we aim to reproduce the results reported by Mooij [3] to validate our numerical methodology. Minor discrepancies are expected because the reference trajectory available to us was reconstructed via OCR, which introduces small perturbations that can propagate into the computed eigenvalues and eigenvectors.

Despite these differences, we recover the same qualitative trends in the principal motion characteristics. Moreover, the observed deviations provide insight into the parameter sensitivities that shape the vehicle's response. To isolate and interpret the most influential parameters, the next chapter employs analytical (literal) approximations for the dominant dynamic modes.

3.2 Eigenvalues and eigenmotion

Before analyzing in detail the stability of the vehicle, it is useful to recall the relation between eigenvalues and eigenmotions. The dynamics of a re-entry configuration can be interpreted in analogy with conventional subsonic aircraft, since the system

exhibits characteristic motions in certain flight regimes. These eigenmotions can be studied at discrete time points along the trajectory, and their behavior illustrates the open-loop stability properties of the vehicle.

Once the eigenvalues and corresponding eigenvectors are computed, they can be directly related to the physical motion of the vehicle. In fact, while the eigenvalue describes the temporal behavior of a mode (whether it is stable, unstable, oscillatory, or aperiodic), the eigenvector provides the spatial structure of that mode. Each eigenvector specifies the relative contribution of the state variables (e.g., angle of attack, sideslip, angular rates, Euler angles) to the eigenmotion. In other words, the eigenvector indicates **how the different states participate in a given mode**, and therefore which physical variables dominate the motion. This information is essential to identify, for example, whether an instability is primarily due to lateral-directional dynamics (yaw/roll) or longitudinal dynamics (pitch/angle of attack).

- **Complex eigenvalues** occurring as conjugate pairs, represent *oscillatory* modes such as the Dutch roll or phugoid, typically associated with periodic motion.
- **Real eigenvalues** on the other hand, indicate aperiodic modes, corresponding to motions such as spiral divergence or roll subsidence.

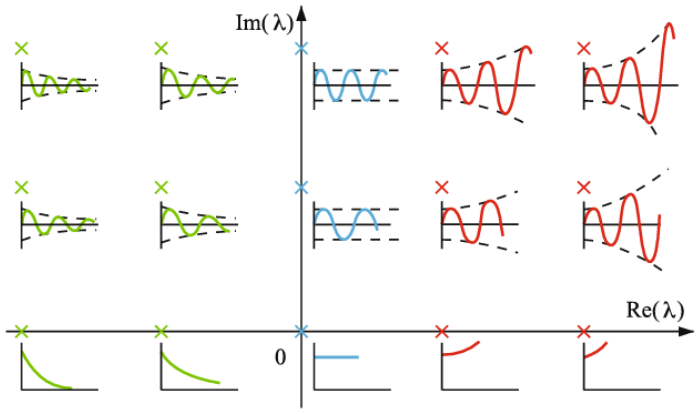

Figura 3.1: Impulse responses for various eigenvalue locations in the complex plane, where the con jugate eigenvalues are omitted[3]

Looking at figure 3.1 the **real** part of an eigenvalue defines the stability of the motion: a negative real part implies a decaying (stable) mode, while a positive real part indicates a growing (unstable) disturbance. If the real part is exactly zero,

the oscillation persists with constant amplitude. The **imaginary part** defines the oscillation frequency of periodic modes.

According to Mooij[4], the dynamics of a re-entry vehicle can be expressed as a set of time-varying differential equations. To apply classical stability and control theory, the nominal trajectory is discretized into a sequence of time intervals. Within each interval, the vehicle states and system parameters are considered constant, so that the dynamics can be approximated by a **Linear Time-Invariant (LTI) system**.
The homogeneous part of the state equation can be written as

$$\dot{\boldsymbol{x}} = A\boldsymbol{x} \tag{3.1}$$

where $\mathbf{x}$ is the state vector and A is the system matrix. The eigenvalues λ and the eigenvectors μ of the system are obtained by solving the eigenvalue problem

$$A\boldsymbol{\mu} = \lambda\boldsymbol{\mu} \tag{3.2}$$

This leads to

$$(A\lambda - I)\boldsymbol{\mu} = 0 \tag{3.3}$$

which admits non-trivial solutions if the determinant condition

$$|A - \lambda I| = 0 \tag{3.4}$$

is satisfied.
Once the eigenvalues and eigenvectors are determined, the corresponding **eigenmotions** can be described. For each mode, the solution is given by

$$\boldsymbol{x}_\lambda(t) = e^{\lambda t}\boldsymbol{\mu}_\lambda \quad , \tag{3.5}$$

while the general solution for an n-state system is a linear combination of all eigenmodes:

$$\boldsymbol{x}(t) = \sum_{i=1}^{n} c_i e^{\lambda_i t}\boldsymbol{\mu}_i \tag{3.6}$$

The constants c_i are determined by the initial conditions, for example by a perturbation of the nominal trajectory. This formulation allows for the decomposition of vehicle dynamics into distinct eigenmotions, each associated with a specific pair of eigenvalues - eigenvectors.
To characterise the eigenmotion we compute some specific coefficients, i.e., the *period* P, when a pair of complex conjugate eigenvalues represents a periodic motion, defined as[4]

$$P = \frac{2\pi}{Im(\lambda)} \tag{3.7}$$

An aperiodic motion does not have a period, which also follows from the fact that the imaginary part of the eigenvalue is zero.
Next, we define the *halving time*[4] $T_{1/2}$, indicating the time interval when the amplitude of the motion has become half its original value,

$$T_{1/2} = \frac{\ln(1/2)}{Re(\lambda)} \tag{3.8}$$

However, when the real part of the eigenvalue is positive, the halving time becomes negative. In that case it is better to speak of the *doubling time* of the (diverging) eigenmotion[4]:

$$T_2 = \frac{\ln(2)}{Re(\lambda)} \tag{3.9}$$

The *damping ratio* ζ for periodic eigenmotion (complex eigenvalues) can be computed with

$$\zeta = -\frac{Re(\lambda)}{\sqrt{Re(\lambda)^2 + Im(\lambda)^2}} \tag{3.10}$$

In the case of damped eigenmotion, ζ is positive (a negative damping ratio is in principle an amplification ratio). For aperiodic motion, ζ is not defined.
Finally, the *natural frequency* ω_n for periodic eigenmotion is defined to be

$$\omega_n = \sqrt{Re(\lambda)^2 + Im(\lambda)^2} \tag{3.11}$$

The natural frequency is the theoretical frequency of the eigenmotion when the energy of the system is constant during that motion, which means that the amplitude is constant. Again, for aperiodic motion ω_n is not defined. It should be noted that the natural frequency is more a mathematical notion rather than a physical one[4].
The relation between the period, the damping ratio and the natural frequency is

$$P = \frac{2\pi}{\omega_n\sqrt{1-\zeta^2}} \tag{3.12}$$

Up to this point, we have only examined the stability characteristics of the eigenmotions, without addressing in which state variables these motions actually manifest. To answer this question, it is necessary to study the eigenvectors. By computing the magnitude of each (complex) component of an eigenvector, one can readily identify the dominant states involved in the motion. Moreover, evaluating the argument (phase) of each component provides insight into the relative phase relationships among the contributing variables.
In mathematical terms, the modulus z of a complex number λ is defined to be

$$z = \sqrt{Re(\lambda)^2 + Im(\lambda)^2} \tag{3.13}$$

and the argument θ is

$$\theta = \arctan\left(\frac{Im(\lambda)}{Re(\lambda)}\right) \tag{3.14}$$

Note that the argument of a real number is always 0 or π ($\lambda < 0$).

3.3 Linearisation of Equations of Motion

«However, the eigenvalues and eigenvectors can only be obtained when the time derivatives of the states are given as a linear combination of the states. In other words: the equations of motion have to be linearised.»[3]. Following the literature tow assumptions are made:

- We will considering a non-rotating Earth ($\omega_{cb} = 0\,\text{rad/s}$. This assumption is allowed since the rotation of the local horizontal plane is of a much higher frequency than the Earth's one
- The vehicle is assumed to be rotationally symmetric (with respect to mass) around the X_B-axis. This means all the products of inertia are zero.

At this point the equations of Chapter 2 become

$$\begin{aligned}
\dot{V} &= -\frac{D}{m} - g\sin\gamma, \\
\dot{\gamma} &= \left(\frac{V}{R} - \frac{g}{V}\right)\cos\gamma + \frac{L\cos\sigma - S\sin\sigma}{mV}, \\
\dot{\chi} &= \frac{V}{R}\cos\gamma\tan\delta\sin\chi - \frac{L\sin\sigma + S\cos\sigma}{mV\cos\gamma}, \\
\dot{R} &= V\sin\gamma, \\
\dot{\tau} &= \frac{V\cos\gamma\sin\chi}{R\cos\delta}, \\
\dot{\delta} &= \frac{V}{R}\cos\gamma\cos\chi, \\
\dot{p} &= \frac{M_x}{I_{xx}} + (I_{yy} - I_{zz})\,qr, \\
\dot{q} &= \frac{M_y}{I_{yy}} + (I_{zz} - I_{xx})\,pr, \\
\dot{r} &= \frac{M_z}{I_{zz}} + (I_{xx} - I_{yy})\,pq.
\end{aligned}$$

In order to further simplify the kinematic attitude equations, the vehicle is assumed to follow a trajectory parallel to the equator, that is ($\delta = 0\,^\circ$ and $\chi = 90\,^\circ$), and remains this way ($\dot{\delta} = 0\,^\circ/\mathrm{s}$):

$$\begin{aligned}
\dot{\alpha} &= q - (p\cos\alpha + r\sin\alpha)\tan\beta - \frac{L - mg\cos\gamma\cos\sigma}{mV\cos\beta},\\
\dot{\beta} &= p\sin\alpha - r\cos\alpha - \frac{S + mg\cos\gamma\sin\sigma}{mV},\\
\dot{\sigma} &= -\frac{p\cos\alpha + r\sin\alpha}{\cos\beta} - \frac{L - mg\cos\gamma\cos\sigma}{mV}\tan\beta + \frac{L\sin\sigma + S\cos\sigma}{mV}\tan\gamma.
\end{aligned}$$

As we can see the equation for χ, τ and δ are no longer coupled with the other equaitons, so 9-degrees-of-freedom linearised model can be derived. To clarify the linearisation procedure, we introduce **small perturbations** about a steady reference condition. Each state variable is written as the sum of an equilibrium value and a small deviation . The vehicle is assumed to be unpowered (no fuel consumption), so that the mass properties remain constant during the motion. Hence, the states are expressed as

$$\begin{aligned}
V &= V_0 + \Delta V, & \gamma &= \gamma_0 + \Delta\gamma, & R &= R_0 + \Delta R,\\
p &= p_0 + \Delta p, & q &= q_0 + \Delta q, & r &= r_0 + \Delta r,\\
\alpha &= \alpha_0 + \Delta\alpha, & \beta &= \beta_0 + \Delta\beta = \Delta\beta, & \sigma &= \sigma_0 + \Delta\sigma.
\end{aligned}$$

The equilibrium points follow from the nominal mission explained in the next sections, which leave us with three unknown parameters: p_0, q_0 an r_0 that can be derived from the attitude kinematics with the condition

$$\dot{\alpha} = \dot{\beta} = \dot{\sigma} = 0.$$

For all the mathematical detail we refer to Mooij[3]. By neglecting small terms of higher order the final form of the equations is:

$$\Delta\dot{V} = -\frac{\Delta D}{m} + 2\frac{g_0}{R_0}\sin\gamma_0\,\Delta R - g_0\cos\gamma_0\,\Delta\gamma,$$

$$\Delta\dot{\gamma} = \left(-\dot{\gamma}_0 + 2\frac{V_0}{R_0}\cos\gamma_0\right)\frac{\Delta V}{V_0} + \left(2\frac{g_0}{R_0} - \frac{V_0^2}{R_0^2}\right)\frac{\cos\gamma_0}{V_0}\,\Delta R - \left(\frac{V_0^2}{R_0} - g_0\right)\frac{\sin\gamma_0}{V_0}\,\Delta\gamma - \frac{L_0}{mV_0}\sin\sigma_0\,\Delta\sigma + \frac{\cos\sigma_0}{mV_0}\,\Delta L - \frac{\sin\sigma_0}{mV_0}\,\Delta S,$$

$$\Delta\dot{R} = \sin\gamma_0\,\Delta V + V_0\cos\gamma_0\,\Delta\gamma,$$

$$\Delta\dot{p} = \frac{\Delta M_x}{I_{xx}},$$

$$\Delta\dot{q} = \frac{\Delta M_y}{I_{yy}},$$

$$\Delta\dot{r} = \frac{\Delta M_z}{I_{zz}},$$

$$\Delta\dot{\alpha} = \Delta q - \frac{1}{mV_0}\,\Delta L - \frac{g_0}{V_0}\cos\gamma_0\sin\sigma_0\,\Delta\sigma + \left(\frac{L_0}{mV_0^2} - \frac{g_0}{V_0^2}\cos\gamma_0\cos\sigma_0\right)\Delta V - \frac{g_0}{V_0}\sin\gamma_0\cos\sigma_0\,\Delta\gamma - 2\frac{g_0}{R_0V_0}\cos\gamma_0\cos\sigma_0\,\Delta R,$$

$$\Delta\dot{\beta} = \sin\alpha_0\,\Delta p - \cos\alpha_0\,\Delta r - \frac{\Delta S}{mV_0} - \frac{g_0}{V_0}\cos\gamma_0\cos\sigma_0\,\Delta\sigma + \frac{g_0}{V_0^2}\cos\gamma_0\sin\sigma_0\,\Delta V + 2\frac{g_0}{R_0V_0}\cos\gamma_0\sin\sigma_0\,\Delta R + \frac{g_0}{V_0}\sin\gamma_0\sin\sigma_0\,\Delta\gamma,$$

$$\Delta\dot{\sigma} = -\cos\alpha_0\,\Delta p - \sin\alpha_0\,\Delta r - \left(\frac{L_0}{mV_0} - \frac{g_0}{V_0}\cos\gamma_0\cos\sigma_0\right)\Delta\beta + \frac{L_0}{mV_0}\sin\sigma_0\,\Delta\gamma + \frac{\tan\gamma_0}{mV_0}\left(\sin\sigma_0\,\Delta L + \cos\sigma_0 L_0\,\Delta\sigma + \cos\sigma_0\,\Delta S - \frac{L_0}{V_0}\sin\sigma_0\,\Delta V\right).$$

3.4 Eigenmotion of Winged Entry Vehicles

Before we can study the open-loop eigenmotion of the winged re-entry vehicle HORUS, the linearised equations obtained in the previous section has to be put into state-space form.

3.4.1 State-space model

In order to analyze the eigenvalues of the dynamic system we want the equation in the state-space form:

$$\dot{\mathbf{x}} = \mathbf{A}\mathbf{x} + \mathbf{B}\mathbf{u} \tag{3.15}$$

where A is the $n \times n$ state matrix, x is the $n \times 1$ state vector, B is the $n \times m$ control matrix and u is the $m \times 1$ control vector. The state vector is obvious and comes from the above sections

$$x = (\Delta V, \Delta\gamma, \Delta R, \Delta p, \Delta q, \Delta r, \Delta\alpha, \Delta\beta, \Delta\sigma)^T \tag{3.16}$$

while for the control vector we use the aerodynamic surface and the thrusthers of Horus2B

$$u = (\Delta\delta_e, \Delta\delta_a, \Delta\delta_r, \Delta M_{T,x}, \Delta M_{T,y}, \Delta M_{T,z})^T \tag{3.17}$$

Where δ_e is the elevon deflection used for the longitudinal control, δ_a is the aileron deflection for the lateral control, δ_r is the rudder deflection for the lateral control and $M_{T,i}$ is the torque generated by the thrusters around the i-axis.
With the above definitions the state space form will be

$$\begin{pmatrix} \Delta\dot{V} \\ \Delta\dot{\gamma} \\ \Delta\dot{R} \\ \Delta\dot{p} \\ \Delta\dot{q} \\ \Delta\dot{r} \\ \Delta\dot{\alpha} \\ \Delta\dot{\beta} \\ \Delta\dot{\sigma} \end{pmatrix} = \begin{bmatrix} a_{VV} & a_{V\gamma} & a_{VR} & a_{Vp} & a_{Vq} & a_{Vr} & a_{V\alpha} & a_{V\beta} & a_{V\sigma} \\ a_{\gamma V} & a_{\gamma\gamma} & a_{\gamma R} & a_{\gamma p} & a_{\gamma q} & a_{\gamma r} & a_{\gamma\alpha} & a_{\gamma\beta} & a_{\gamma\sigma} \\ a_{RV} & a_{R\gamma} & a_{RR} & a_{Rp} & a_{Rq} & a_{Rr} & a_{R\alpha} & a_{R\beta} & a_{R\sigma} \\ a_{pV} & a_{p\gamma} & a_{pR} & a_{pp} & a_{pq} & a_{pr} & a_{p\alpha} & a_{p\beta} & a_{p\sigma} \\ a_{qV} & a_{q\gamma} & a_{qR} & a_{qp} & a_{qq} & a_{qr} & a_{q\alpha} & a_{q\beta} & a_{q\sigma} \\ a_{rV} & a_{r\gamma} & a_{rR} & a_{rp} & a_{rq} & a_{rr} & a_{r\alpha} & a_{r\beta} & a_{r\sigma} \\ a_{\alpha V} & a_{\alpha\gamma} & a_{\alpha R} & a_{\alpha p} & a_{\alpha q} & a_{\alpha r} & a_{\alpha\alpha} & a_{\alpha\beta} & a_{\alpha\sigma} \\ a_{\beta V} & a_{\beta\gamma} & a_{\beta R} & a_{\beta p} & a_{\beta q} & a_{\beta r} & a_{\beta\alpha} & a_{\beta\beta} & a_{\beta\sigma} \\ a_{\sigma V} & a_{\sigma\gamma} & a_{\sigma R} & a_{\sigma p} & a_{\sigma q} & a_{\sigma r} & a_{\sigma\alpha} & a_{\sigma\beta} & a_{\sigma\sigma} \end{bmatrix} \begin{pmatrix} \Delta V \\ \Delta\gamma \\ \Delta R \\ \Delta p \\ \Delta q \\ \Delta r \\ \Delta\alpha \\ \Delta\beta \\ \Delta\sigma \end{pmatrix}$$
$$+ \begin{bmatrix} b_{Ve} & b_{Va} & b_{Vr} & b_{Vx} & b_{Vy} & b_{Vz} \\ b_{\gamma e} & b_{\gamma a} & b_{\gamma r} & b_{\gamma x} & b_{\gamma y} & b_{\gamma z} \\ b_{Re} & b_{Ra} & b_{Rr} & b_{Rx} & b_{Ry} & b_{Rz} \\ b_{pe} & b_{pa} & b_{pr} & b_{px} & b_{py} & b_{pz} \\ b_{qe} & b_{qa} & b_{qr} & b_{qx} & b_{qy} & b_{qz} \\ b_{re} & b_{ra} & b_{rr} & b_{rx} & b_{ry} & b_{rz} \\ b_{\alpha e} & b_{\alpha a} & b_{\alpha r} & b_{\alpha x} & b_{\alpha y} & b_{\alpha z} \\ b_{\beta e} & b_{\beta a} & b_{\beta r} & b_{\beta x} & b_{\beta y} & b_{\beta z} \\ b_{\sigma e} & b_{\sigma a} & b_{\sigma r} & b_{\sigma x} & b_{\sigma y} & b_{\sigma z} \end{bmatrix} \begin{pmatrix} \Delta\delta_e \\ \Delta\delta_a \\ \Delta\delta_r \\ \Delta M_{T,x} \\ \Delta M_{T,y} \\ \Delta M_{T,z} \end{pmatrix}. \tag{3.18}$$

Now in order to get every single coefficient of the matrices A and B we must to analyze the dependencies of each state from every states and of each state from every commands.

All the mathematical details are skipped and we refer to Mooij[3][4] for details. The final form of the equations is

$$\begin{pmatrix} \Delta\dot{V} \\ \Delta\dot{\gamma} \\ \Delta\dot{R} \\ \Delta\dot{p} \\ \Delta\dot{q} \\ \Delta\dot{r} \\ \Delta\dot{\alpha} \\ \Delta\dot{\beta} \\ \Delta\dot{\sigma} \end{pmatrix} = \begin{bmatrix} a_{VV} & a_{V\gamma} & a_{VR} & 0 & 0 & 0 & a_{V\alpha} & 0 & 0 \\ a_{\gamma V} & a_{\gamma\gamma} & a_{\gamma R} & 0 & 0 & 0 & a_{\gamma\alpha} & a_{\gamma\beta} & a_{\gamma\sigma} \\ a_{RV} & a_{R\gamma} & a_{RR} & 0 & 0 & 0 & 0 & 0 & 0 \\ 0 & 0 & 0 & 0 & 0 & 0 & a_{p\alpha} & a_{p\beta} & 0 \\ a_{qV} & 0 & a_{qR} & 0 & 0 & 0 & a_{q\alpha} & 0 & 0 \\ 0 & 0 & 0 & 0 & 0 & 0 & a_{r\alpha} & a_{r\beta} & 0 \\ a_{\alpha V} & a_{\alpha\gamma} & a_{\alpha R} & 0 & a_{\alpha q} & 0 & a_{\alpha\alpha} & 0 & a_{\alpha\sigma} \\ a_{\beta V} & a_{\beta\gamma} & a_{\beta R} & a_{\beta p} & 0 & a_{\beta r} & 0 & a_{\beta\beta} & a_{\beta\sigma} \\ a_{\sigma V} & a_{\sigma\gamma} & a_{\sigma R} & a_{\sigma p} & 0 & a_{\sigma r} & a_{\sigma\alpha} & a_{\sigma\beta} & a_{\sigma\sigma} \end{bmatrix} \begin{pmatrix} \Delta V \\ \Delta\gamma \\ \Delta R \\ \Delta p \\ \Delta q \\ \Delta r \\ \Delta\alpha \\ \Delta\beta \\ \Delta\sigma \end{pmatrix} + \begin{bmatrix} 0 & 0 & 0 & 0 & 0 & 0 \\ 0 & 0 & 0 & 0 & 0 & 0 \\ 0 & 0 & 0 & 0 & 0 & 0 \\ 0 & b_{pa} & 0 & b_{px} & 0 & 0 \\ b_{qe} & 0 & 0 & 0 & b_{qy} & 0 \\ 0 & b_{ra} & b_{rr} & 0 & 0 & b_{rz} \\ 0 & 0 & 0 & 0 & 0 & 0 \\ 0 & 0 & 0 & 0 & 0 & 0 \\ 0 & 0 & 0 & 0 & 0 & 0 \end{bmatrix} \begin{pmatrix} \Delta\delta_e \\ \Delta\delta_a \\ \Delta\delta_r \\ \Delta M_{T,x} \\ \Delta M_{T,y} \\ \Delta M_{T,z} \end{pmatrix}. \tag{3.19}$$

The coefficients of the matrix A are:

$$a_{VV} = -\frac{1}{mV_0}\left(M_0\frac{\partial C_D}{\partial M}\,\bar{q}_0 S_{\text{ref}} + 2D_0\right),$$

$$a_{V\gamma} = -g_0\cos\gamma_0,$$

$$a_{VR} = 2\,\frac{g_0}{R_0}\sin\gamma_0 - \frac{\partial C_D}{\partial M}\,\frac{M_0^2}{mV_0}\,\frac{\mathrm{d}a}{\mathrm{d}h}\,\bar{q}_0 S_{\text{ref}} + \frac{1}{2}\,C_{D,0}S_{\text{ref}}\frac{V_0^2}{m}\,\frac{\mathrm{d}\rho}{\mathrm{d}h},$$

$$a_{V\alpha} = -\frac{1}{m}\,\frac{\partial C_D}{\partial \alpha}\,\bar{q}_0 S_{\text{ref}},$$

$$a_{Vp} = a_{Vq} = a_{Vr} = a_{V\beta} = a_{V\sigma} = 0.$$

$$a_{\gamma V} = \frac{1}{V_0}\left(-\dot{\gamma}_0 + 2\frac{V_0}{R_0}\cos\gamma_0\right) + \frac{\cos\sigma_0}{mV_0^2}\left(M_0\frac{\partial C_L}{\partial M}\,\bar{q}_0 S_{\text{ref}} + 2L_0\right),$$

$$a_{\gamma\gamma} = -\left(\frac{V_0}{R_0} - \frac{g_0}{V_0}\right)\sin\gamma_0,$$

$$a_{\gamma R} = \left(2\frac{g_0}{V_0} - \frac{V_0}{R_0}\right)\frac{\cos\gamma_0}{R_0} + \frac{\cos\sigma_0}{mV_0}\left(\frac{1}{2}C_{L,0}S_{\text{ref}}V_0^2\frac{\mathrm{d}\rho}{\mathrm{d}h} - \frac{\partial C_L}{\partial M}\,\frac{M_0^2}{V_0}\frac{\mathrm{d}a}{\mathrm{d}h}\,\bar{q}_0 S_{\text{ref}}\right),$$

$$a_{\gamma\alpha} = \frac{\cos\sigma_0}{mV_0}\frac{\partial C_L}{\partial \alpha}\,\bar{q}_0 S_{\text{ref}},$$

$$a_{\gamma\beta} = -\frac{\sin\sigma_0}{mV_0}\frac{\partial C_S}{\partial \beta}\,\bar{q}_0 S_{\text{ref}},$$

$$a_{\gamma\sigma} = -\frac{L_0}{mV_0}\sin\sigma_0,$$

$$a_{\gamma p} = a_{\gamma q} = a_{\gamma r} = 0.$$

$$a_{RV} = \sin\gamma_0,$$

$$a_{R\gamma} = V_0\cos\gamma_0,$$

$$a_{RR} = a_{Rp} = a_{Rq} = a_{Rr} = a_{R\alpha} = a_{R\beta} = a_{R\sigma} = 0.$$

$$a_{p\beta} = \frac{1}{I_{xx}}\frac{\partial C_l}{\partial \beta}\,\bar{q}_0 S_{\text{ref}} b_{\text{ref}},$$

$$a_{pV} = a_{p\gamma} = a_{pR} = a_{pp} = a_{pq} = a_{pr} = a_{p\alpha} = a_{p\sigma} = 0.$$

$$a_{qV} = \frac{1}{I_{yy}}\,\frac{M_0}{V_0}\frac{\partial C_m}{\partial M}\,\bar{q}_0 S_{\text{ref}} c_{\text{ref}},$$

$$a_{qR} = -\frac{1}{I_{yy}}\,\frac{M_0^2}{V_0}\frac{\partial C_m}{\partial M}\,\bar{q}_0 S_{\text{ref}} c_{\text{ref}}\frac{\mathrm{d}a}{\mathrm{d}h},$$

$$a_{q\alpha} = \frac{1}{I_{yy}} \frac{\partial C_m}{\partial \alpha} \bar{q}_0 S_{\text{ref}} c_{\text{ref}},$$

$$a_{q\gamma} = a_{qp} = a_{qq} = a_{qr} = a_{q\beta} = a_{q\sigma} = 0.$$

$$a_{r\beta} = \frac{1}{I_{zz}} \frac{\partial C_n}{\partial \beta} \bar{q}_0 S_{\text{ref}} b_{\text{ref}},$$

$$a_{rV} = a_{r\gamma} = a_{rR} = a_{rp} = a_{rq} = a_{rr} = a_{r\alpha} = a_{r\sigma} = 0.$$

$$a_{\alpha V} = -\frac{g_0}{V_0^2} \cos\gamma_0 \cos\sigma_0 - \frac{1}{mV_0^2} \left(M_0 \frac{\partial C_L}{\partial M} + C_L \right) \bar{q}_0 S_{\text{ref}},$$

$$a_{\alpha\gamma} = -\frac{g_0}{V_0} \sin\gamma_0 \cos\sigma_0,$$

$$a_{\alpha R} = -2\frac{g_0}{R_0 V_0} \cos\gamma_0 \cos\sigma_0 + \frac{1}{mV_0} \left(\frac{1}{2} C_{L,0} S_{\text{ref}} V_0^2 \frac{\mathrm{d}\rho}{\mathrm{d}h} - \frac{\partial C_L}{\partial M} \frac{M_0^2}{V_0} \frac{\mathrm{d}a}{\mathrm{d}h} \bar{q}_0 S_{\text{ref}} \right),$$

$$a_{\alpha q} = 1,$$

$$a_{\alpha\alpha} = -\frac{1}{mV_0} \frac{\partial C_L}{\partial \alpha} \bar{q}_0 S_{\text{ref}},$$

$$a_{\alpha\sigma} = -\frac{g_0}{V_0} \cos\gamma_0 \sin\sigma_0,$$

$$a_{\alpha p} = a_{\alpha r} = a_{\alpha\beta} = 0.$$

$$a_{\beta V} = \frac{g_0}{V_0^2} \cos\gamma_0 \sin\sigma_0,$$

$$a_{\beta\gamma} = \frac{g_0}{V_0} \sin\gamma_0 \sin\sigma_0,$$

$$a_{\beta R} = 2\frac{g_0}{R_0 V_0} \cos\gamma_0 \sin\sigma_0,$$

$$a_{\beta p} = \sin\alpha_0,$$

$$a_{\beta r} = -\cos\alpha_0,$$

$$a_{\beta\beta} = -\frac{1}{mV_0} \frac{\partial C_S}{\partial \beta} \bar{q}_0 S_{\text{ref}},$$

$$a_{\beta\sigma} = -\frac{g_0}{V_0} \cos\gamma_0 \cos\sigma_0,$$

$$a_{\beta q} = a_{\beta\alpha} = 0.$$

$$a_{\sigma V} = \frac{\tan\gamma_0 \sin\sigma_0}{mV_0^2} \left(M_0 \frac{\partial C_L}{\partial M} + C_L \right) \bar{q}_0 S_{\text{ref}},$$

$$
\begin{aligned}
a_{\sigma\gamma} &= \frac{L_0}{mV_0}\sin\sigma_0,\\
a_{\sigma R} &= \frac{\tan\gamma_0\sin\sigma_0}{mV_0}\left(\frac{1}{2}C_{L,0}S_{\text{ref}}V_0^2\frac{\mathrm{d}\rho}{\mathrm{d}h} - \frac{\partial C_L}{\partial M}\,\frac{M_0^2}{V_0}\frac{\mathrm{d}a}{\mathrm{d}h}\,\bar{q}_0 S_{\text{ref}}\right),\\
a_{\sigma p} &= -\cos\alpha_0,\\
a_{\sigma r} &= -\sin\alpha_0,\\
a_{\sigma\alpha} &= \frac{\tan\gamma_0\sin\sigma_0}{mV_0}\frac{\partial C_L}{\partial\alpha}\,\bar{q}_0 S_{\text{ref}},\\
a_{\sigma\beta} &= \frac{\tan\gamma_0\cos\sigma_0}{mV_0}\frac{\partial C_S}{\partial\beta}\,\bar{q}_0 S_{\text{ref}} - \frac{L_0}{mV_0} + \frac{g_0}{V_0}\cos\gamma_0\cos\sigma_0,\\
a_{\sigma\sigma} &= \tan\gamma_0\cos\sigma_0\,\frac{L_0}{mV_0},\\
a_{\sigma q} &= 0.
\end{aligned}
$$

Since we are interested in the open-loop behaviour of the dynamic system, the input matrix B is not used in this chapter, but in Chapter 5 for the computing of the controller's gain by the LQR. Its coefficients are nevertheless reported here for completeness:

$$
\begin{aligned}
b_{Ve} &= b_{Va} = b_{Vr} = b_{Vx} = b_{Vy} = b_{Vz} = 0,\\
b_{\gamma e} &= b_{\gamma a} = b_{\gamma r} = b_{\gamma x} = b_{\gamma y} = b_{\gamma z} = 0,\\
b_{Re} &= b_{Ra} = b_{Rr} = b_{Rx} = b_{Ry} = b_{Rz} = 0,\\
b_{pa} &= \frac{1}{I_{xx}}\frac{\partial C_l}{\partial\delta_a}\,\bar{q}_0 S_{\text{ref}} b_{\text{ref}},\\
b_{px} &= \frac{1}{I_{xx}},\\
b_{pe} &= b_{pr} = b_{py} = b_{pz} = 0,\\
b_{qe} &= \frac{1}{I_{yy}}\frac{\partial C_m}{\partial\delta_e}\,\bar{q}_0 S_{\text{ref}} c_{\text{ref}},\\
b_{qy} &= \frac{1}{I_{yy}},\\
b_{qa} &= b_{qr} = b_{qx} = b_{qz} = 0,
\end{aligned}
$$

$$
\begin{aligned}
b_{ra} &= \frac{1}{I_{zz}} \frac{\partial C_n}{\partial \delta_a} \bar{q}_0 S_{\text{ref}} b_{\text{ref}}, \\
b_{rr} &= \frac{1}{I_{zz}} \frac{\partial C_n}{\partial \delta_r} \bar{q}_0 S_{\text{ref}} b_{\text{ref}}, \\
b_{rz} &= \frac{1}{I_{zz}}, \\
b_{re} &= b_{rx} = b_{ry} = 0, \\
b_{\alpha e} &= b_{\alpha a} = b_{\alpha r} = b_{\alpha x} = b_{\alpha y} = b_{\alpha z} = 0, \\
b_{\beta e} &= b_{\beta a} = b_{\beta r} = b_{\beta x} = b_{\beta y} = b_{\beta z} = 0, \\
b_{\sigma e} &= b_{\sigma a} = b_{\sigma r} = b_{\sigma x} = b_{\sigma y} = b_{\sigma z} = 0.
\end{aligned}
$$

Furthermore, in the following analysis all dependencies on air density and speed of sound are neglected.

3.4.2 Nominal mission

The nominal re-entry trajectory used in this work was reconstructed from plots by means of OCR/digitization. As a consequence, small discrepancies with respect to Mooij's reference trajectory are unavoidable (e.g., due to finite image resolution, axis scaling, and the smoothing/interpolation required to obtain a uniformly sampled time history). In line with Mooij's approach, the trajectory is then discretized into short time windows, within which the vehicle and atmospheric parameters are frozen and the dynamics are treated as a sequence of LTI systems. This "frozen-time" representation is sufficient for the purposes of modal analysis.
The reference mission of HORUS begins in low Earth orbit with a de-orbit burn followed by a ballistic coasting arc. The hypersonic re-entry phase is assumed to start at the atmospheric entry interface, taken here at an altitude of $h = 122$ km. At this point the initial conditions of the point-mass trajectory are

$$
\begin{aligned}
V &= 7435.5 \text{ m/s}, \\
\gamma &= -1.43^\circ, \\
\chi &= 70.75^\circ, \\
h &= 122 \text{ km}, \\
\tau &= -106.58^\circ, \\
\delta &= -22.3^\circ,
\end{aligned}
$$

where V is the inertial velocity magnitude, γ the flight–path angle, χ the heading angle, h the geodetic altitude, and τ and δ denote longitude and latitude, respectively. These conditions are used as the initial state for the numerical integration of the full non-linear 6-DOF model in the final chapter, in order to simulate the complete re-entry and analyse the resulting vehicle ground track with respect to the targeted landing site near Kourou.
Because eigenvalue/eigenvector trends depend primarily on the qualitative evolution of the flight conditions (mach number, dynamic pressure, bank angle, angle of attack), the digitization noise may slightly shift numerical values (e.g. frequencies and damping ratios) but does not alter the identity and ordering of the characteristic modes nor their qualitative behavior across the trajectory. In other words, the conclusions drawn from the eigenstructure—such as the emergence, disappearance, or strengthening/weakening of specific modes—remain valid.

Finally, any residual trajectory uncertainty is explicitly addressed at the control-design level. The controller is scheduled along the nominal trajectory and tuned for robustness, so that bounded perturbations in the reconstructed states and parameters are accommodated without loss of stability or performance. Hence, while the OCR process introduces modest quantitative deviations, the qualitative modal insights used to guide design remain reliable, and the controller's robustness margins cover the remaining uncertainty.

In the following images (from fig.3.2 to fig.5.5), the original trajectory and the interpolated one are reported.

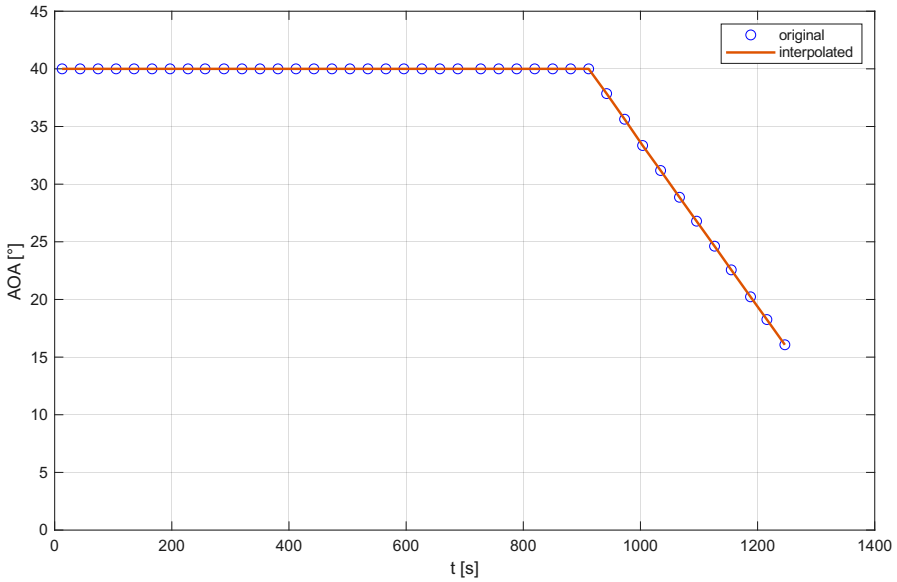

Figura 3.2: Angle of attack along the trajectory

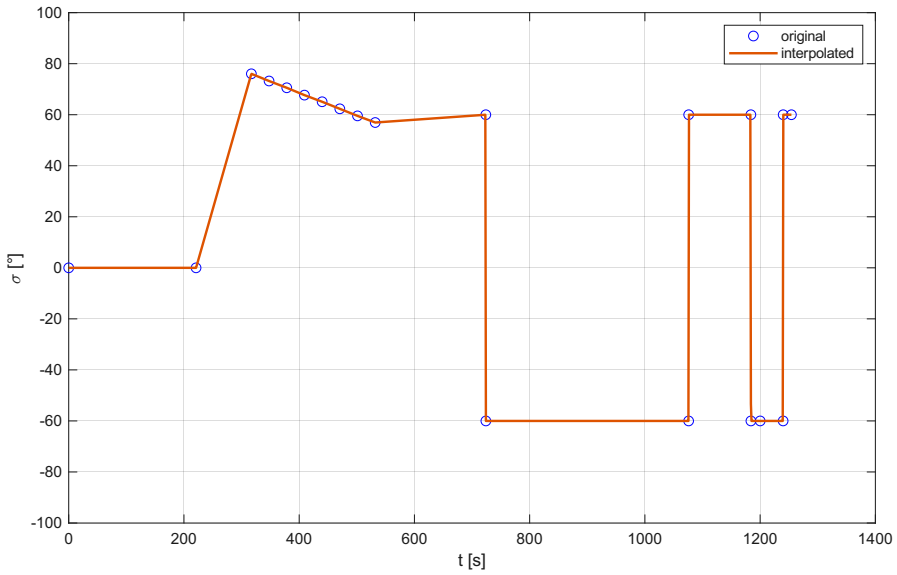

Figura 3.3: Bank angle along the trajectory

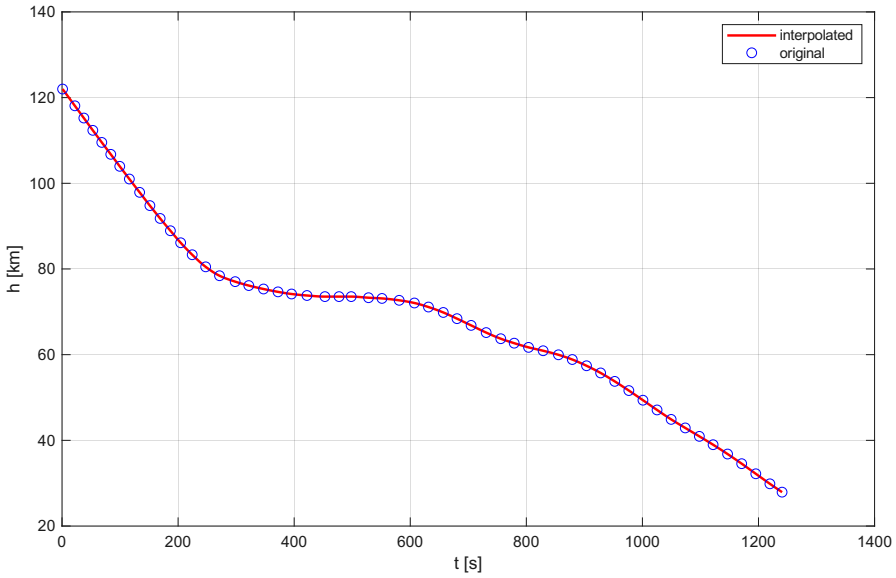

Figura 3.4: Height along the trajectory

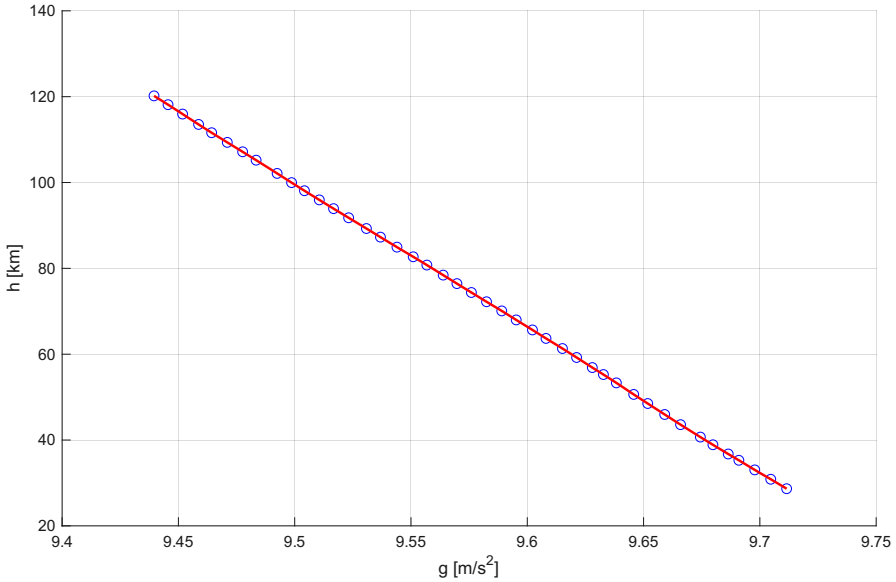

Figura 3.5: Height as a function of the gravitational acceleration

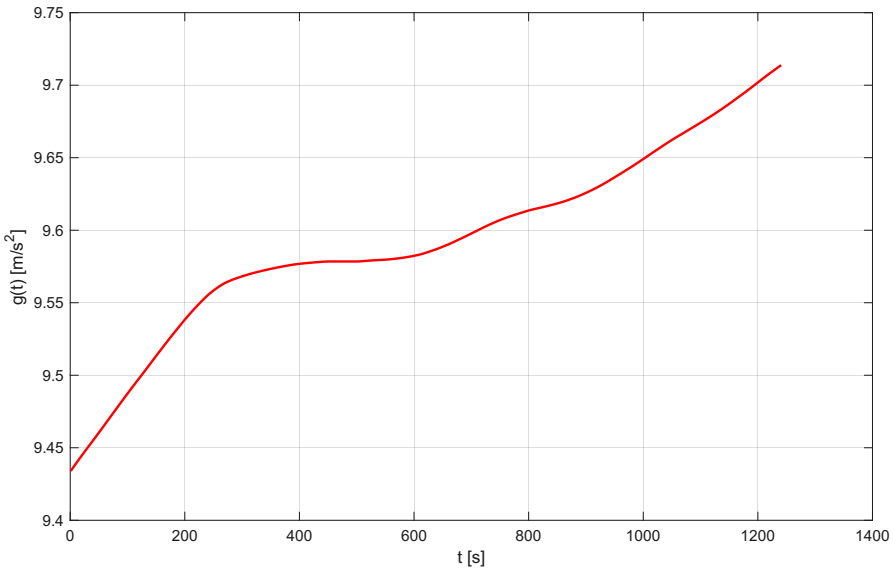

Figura 3.6: Gravitational acceleration along the trajectory

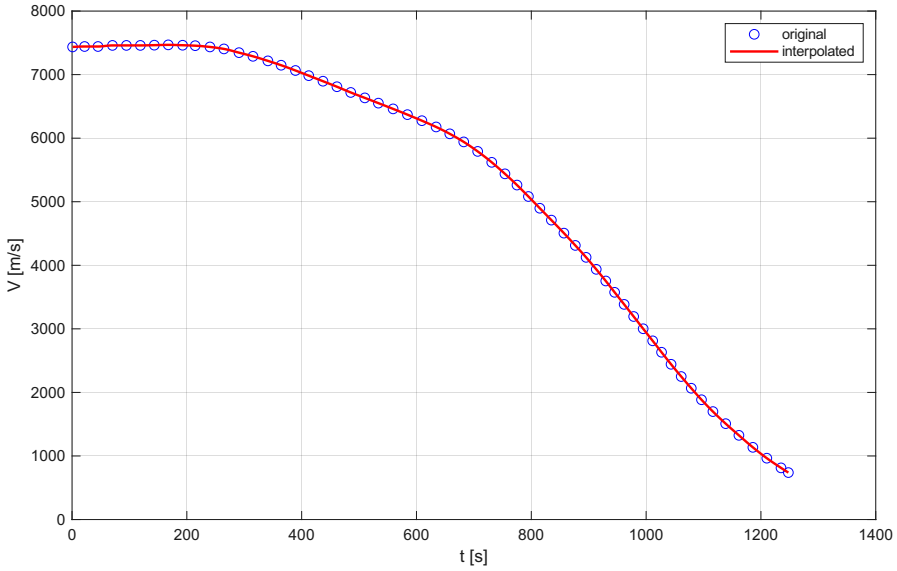

Figura 3.7: Velocity along the trajectory

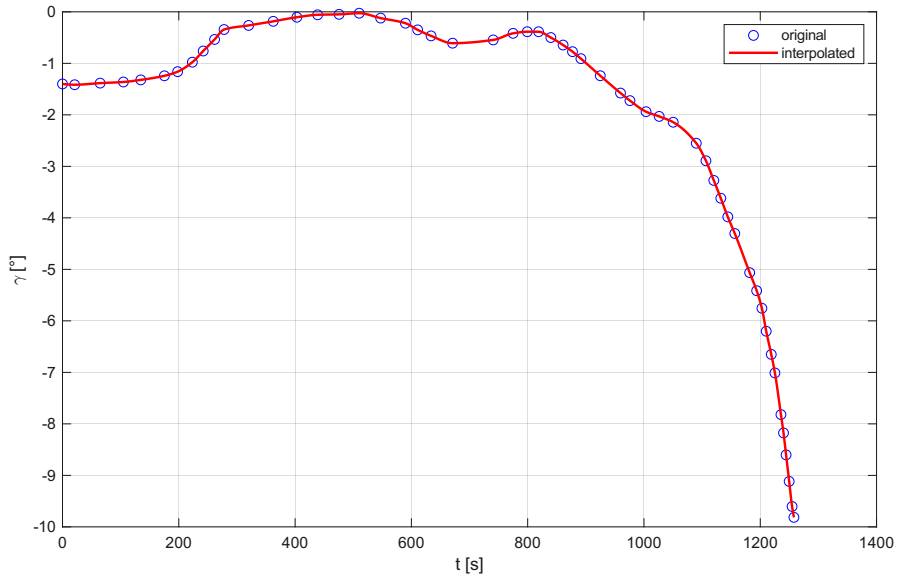

Figura 3.8: Flight path angle along the trajectory

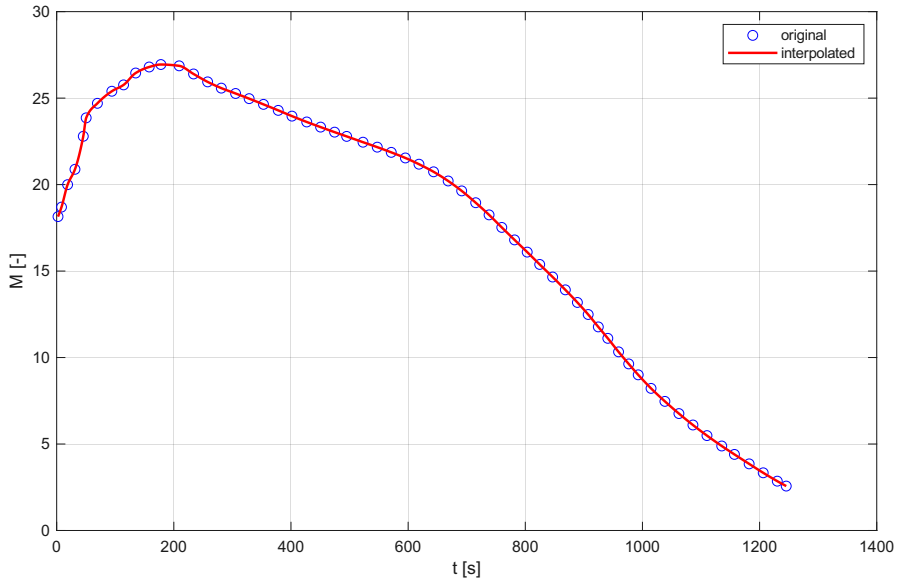

Figura 3.9: Mach number along the trajectory

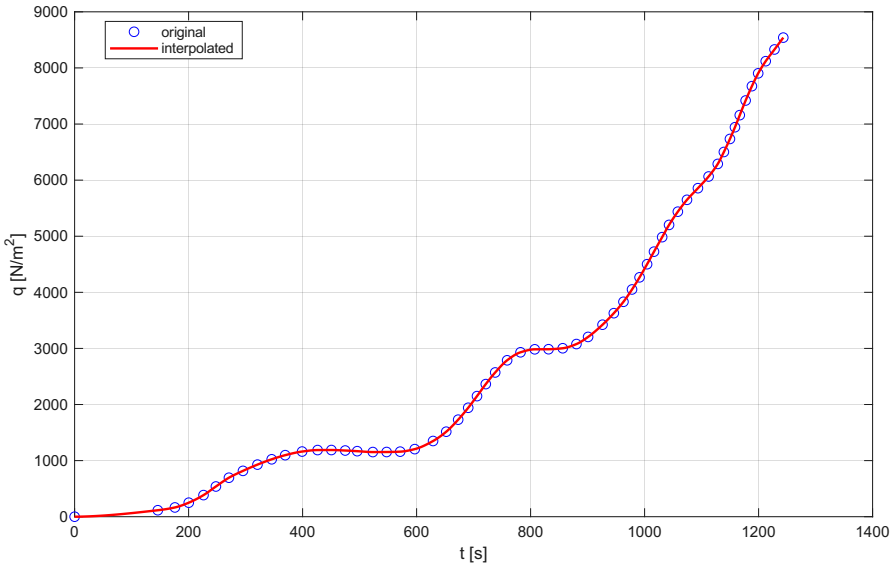

Figura 3.10: Dynamic pressure along the trajectory

As we can see for the gravitational acceleration (Fig.3.6) there is no original raw data. This is because the interpolated point came directly from the height along the trajectory (Fig.3.4) and the height along the gravitational acceleration (Fig.3.5).

- All data are interpolated by using *pchip* in MATLAB. This function generates a cubic spline in order to preserve the shape and trend of the raw data.
- The angle of attack (AOA) and the bank angle (σ) are interpolated using the *linear* shape. This is because the angle of attack is constant for most of the trajectory and then decreases linearly. The bank angle changes instantaneously, so the linear interpolation fits best.

3.4.3 Trim law

In order to analyze the open-loop behaviour of the vehicle, we need to ensure the equilibrium point for the linearization of the equations. This equilibrium is reached only by the pitch equilibrium [4]. So, the task is to first find the body-flap deflection that nulls the moment coefficient (C_m). If and when the body flap is saturated, the elevon compensates for the remaining pitching moment. The algorithm that provides equilibrium is very simple:

1. With M_0 and α_0 we find the function $C_m(\alpha_0, M_0, \delta_{bf})$ with δ_{bf} varying from $-20°$ to $30°$.
2. With Newton-tangent method (*fzero* in MATLAB) we find the $\delta^\star_{bf}$ solution of $C_m(\alpha_0, M_0, \delta^\star_{bf}) = 0$, with $\delta_{bf,0} = 0°$ as starting point.
3. Finally the following trajectory point generates new M_0 and new α_0 so the algorithm return to the point 1

Furthermore the pressure dynamic condition[3] is met:

- while $\bar{q} \leq 100\,\mathrm{N/m^2}$ the aerodynamic surfaces are de-activated

In figure 3.11 the bodyflap deflection range between $15°$ and $-20°$. The lasts two seconds the bodyflap reaches its boundary level and the elevon is activated (Fig.3.12). In figure 3.13 the pitch equilibrium is guaranteed.

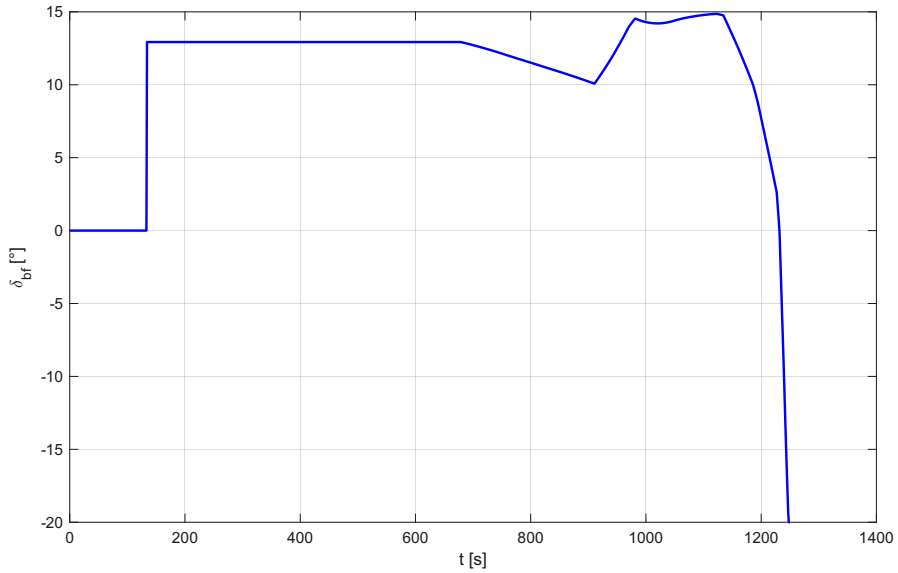

Figura 3.11: Body-flap deflection along the trajectory

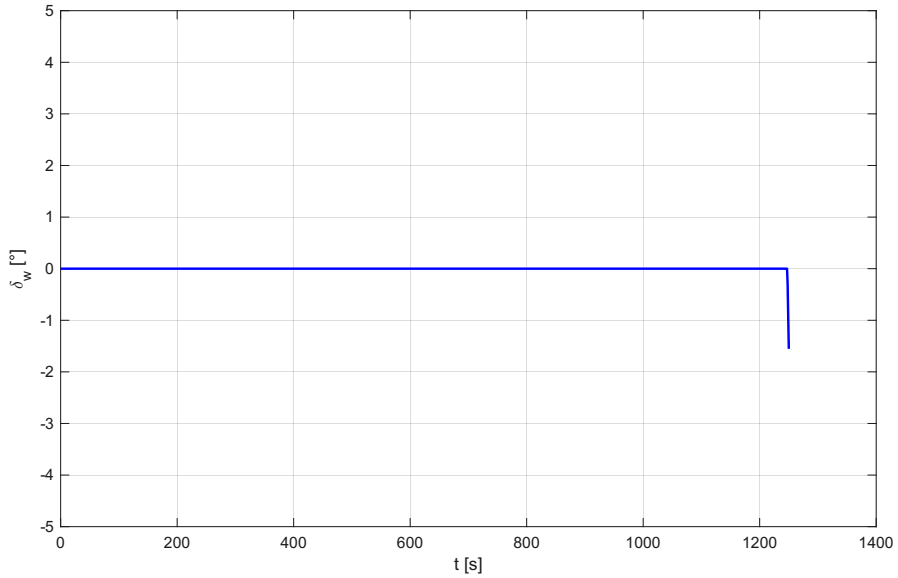

Figura 3.12: Elevon deflection along the trajectory

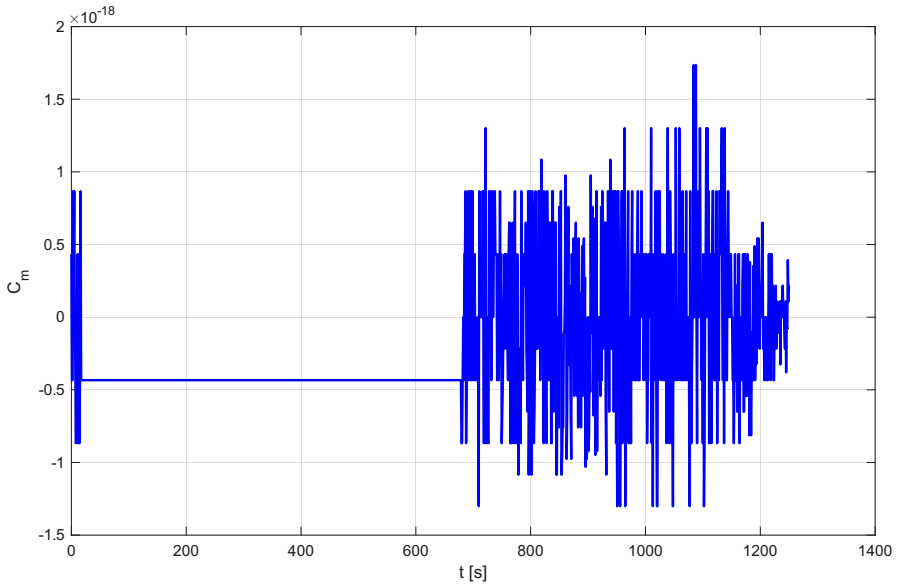

Figura 3.13: Pitch coefficient along the trajectory

3.4.4 HORUS Characteristic Motion

In order to properly interpret the open-loop behaviour of HORUS, it is first necessary to recall the classical dynamic modes of a conventional subsonic aircraft. These canonical eigenmotions provide the natural framework against which the eigenvalues and eigenvectors of HORUS can be compared, since in certain flight regimes we expect at least partial similarity between the two [3]. The purpose of the following discussion is to outline the fundamental relation between eigenvalues and eigenmotions and to establish a reference set of well-known aircraft modes that will serve as a benchmark for the subsequent results.
For a conventional subsonic aircraft in steady flight, five characteristic modes can be identified: two longitudinal and three lateral [3].

- **Longitudinal modes**
  - **Short period**: a fast, usually well-damped oscillation dominated by pitch rate, with large aerodynamic forces and nearly straight flight path; speed variations are negligible.
  - **Phugoid**: a very slow, lightly damped oscillation; gradual speed and altitude variations lead to small changes in dynamic pressure and aerodynamic forces; it can be interpreted as a continuous exchange between kinetic and potential energy, with negligible pitch rotation.
- **Lateral Modes**
  - **Lateral oscillation (Dutch roll)**: a relatively fast, generally well-damped oscillation, primarily due to yawing motion, accompanied by significant roll rate; the flight path and velocity remain essentially constant.
  - **Roll convergence (aperiodic roll)**: a strongly damped, aperiodic motion consisting of pure rolling about the longitudinal axis; the roll angle does not generate restoring moments, hence no oscillation occurs.
  - **Spiral mode**: mainly a yawing motion with some roll and nearly zero sideslip; aerodynamic forces are very small, leading to a large time constant; it is an aperiodic mode which can be either stable or unstable.

In conventional aircraft these longitudinal and lateral modes are weakly coupled and can typically be analysed as decoupled: symmetric perturbations do not significantly excite asymmetric motions, and vice versa [3]. For HORUS, the system matrix $A \in \mathbb{R}^{9x9}$ yields **nine** eigenvalues and associated eigenvectors. Inspection of A shows that there are non-negligible **coupling terms** between the so called symmetric variables $(\Delta V, \Delta\gamma, \Delta R, \Delta q, \Delta\alpha)$ and asymmetric variables $(\Delta p, \Delta r, \Delta\beta, \Delta\sigma)$. Thus, longitudinal and lateral motions are not perfectly decoupled, though decoupling may be a good approximation when these terms remain small[3].

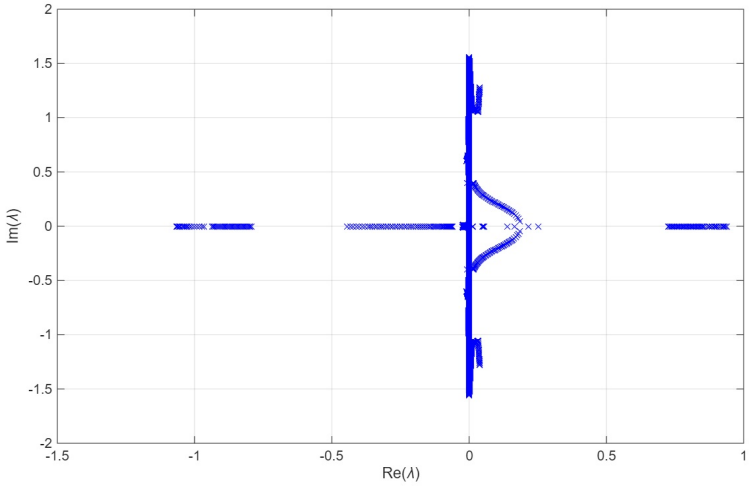

Figura 3.14: Eigenvalues along the trajectory

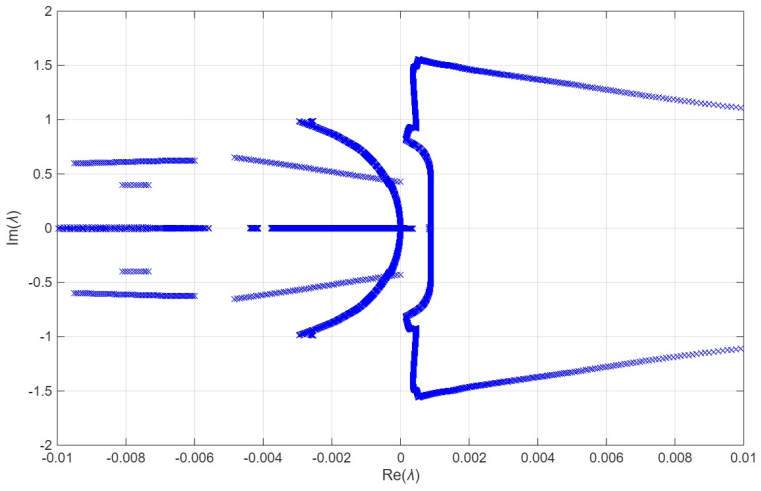

Figura 3.15: Eignevalues zoom around the origin

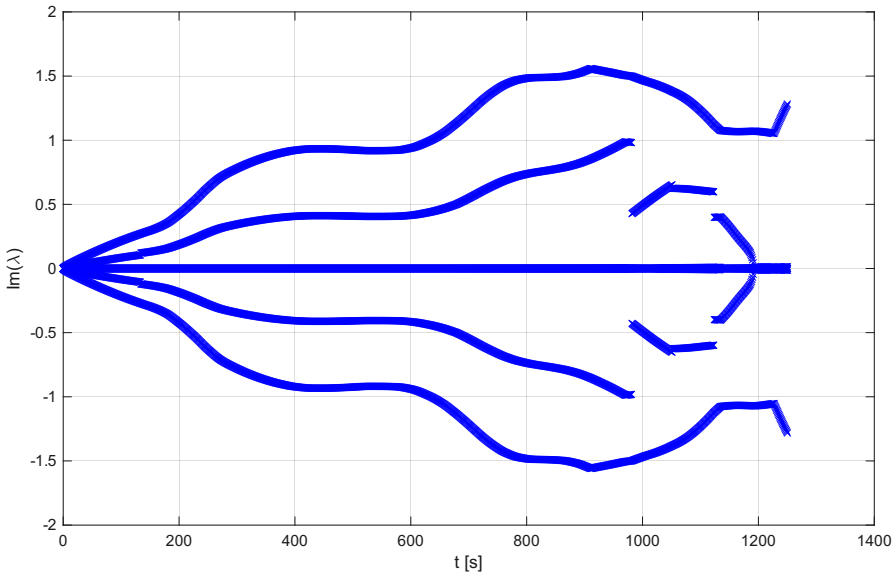

Figura 3.16: Imaginary parts along the trajectory

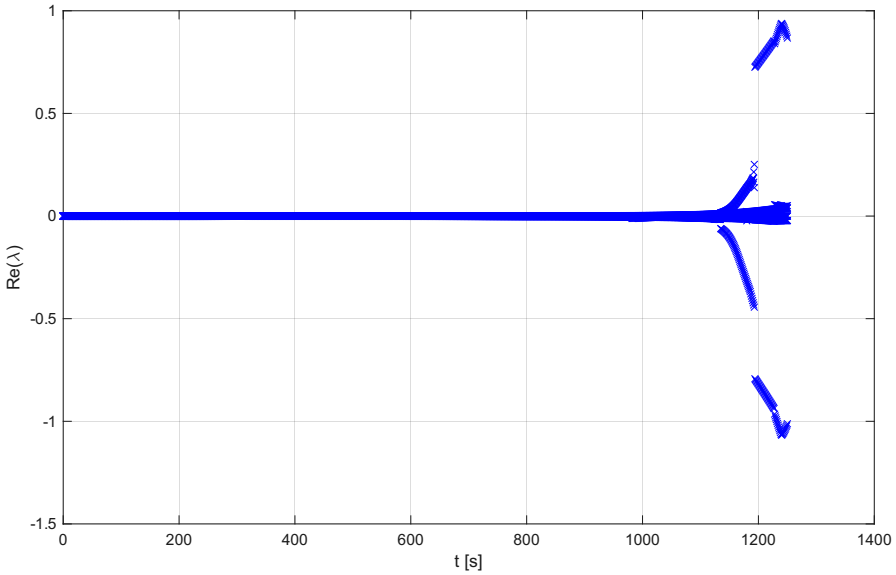

Figura 3.17: Real parts along the trajectory

Along the nominal trajectory, the eigenvalue diagrams (Fig.3.14, Fig.3.15, Fig.3.16, Fig.3.17) reveal a mixture of complex and real roots, indicating that both oscillatory and aperiodic modes are present. Maximum imaginary parts of about 1.5 rad/s imply rather short periods, while real parts between approximately -1 and 1 suggest that the modes can be either convergent or divergent. Two dominant oscillatory families emerge clearly, corresponding later to the lateral oscillation and the short-period oscillation. Discontinuities visible in some curves came from the linearisation of aerodynamic coefficients and table interpolation, which introduce jumps when changing database ranges [3]. For most of the trajectory the eigenmotions appear very lightly damped or undamped; only toward the end strong divergences or convergences arise because of the strong aerodynamic forces [3].

To study the eigenmotion of HORUS in more detail, we have selected several time points for which we will compute the characteristic values and for which we will try to identify the modes by studying the eigenvectors. The selected time points are 1 ($t = 5$ s), 50 (t= 196 s), 100 (t= 396 s), 150 (t= 596 s), 200 (t= 796 s), 250 (t = 996 s), 300 (t = 1196 s) and 314 (t = 1252 s). The numerical results are presented in Appendix A.
«In principle, we can trace the five motions, which we discussed before for conventional aircraft. However, due to the larger speed regime and due to the distinct nature of the nominal trajectory (large bank angles as compared with the steady cruise flight of subsonic aircraft), we find some differences. [...] Whereas in the aircraft case the height and velocity remained constant, it seems that here this is not the case, basically because of the much slower character of the re-entry short-period mode.»[3]. Here a comparison with Mooij's results:

- At start point all the results match with reference[3], except for the phugoid which is stable in this simulation.
- The period of longitudinal mode short period decreases as well. In the last phase of the trajectory the short period becomes aperiodic with two real eigenvalues, one stable and the other one unstable
- The phugoid damping ration increases and the period decreases
- The lateral motion is unstable for all the trajectory. The period decrease rapidly and there is coupling in the final part because the presence of the (large) bank angle
- The aperiodic roll mode changes into a single unstable periodic roll mode. At the next time point it changes in an aperiodic one dominated by the height variable. Later it returns to a stable periodic roll.

To demonstrate convergence, the time histories of key modal metrics as period, natural frequency, damping ratio, and halving time—between between this numerical solution and Mooij's reference results are compared. The overlaid curves are nearly coincident across the trajectory, confirming both the qualitative trends and the quantitative agreement which are reported in the following figures.
Moreover, a discrepancy was identified in the tabulated values reported by Mooij[3]. In particular, at ($t = 396$ s) and ($t = 596$ s) the damping ratio given in the table is not consistent with the value obtained from the corresponding real part and natural frequency. This is most likely a typographical error; in the following, the corrected damping values are used directly.

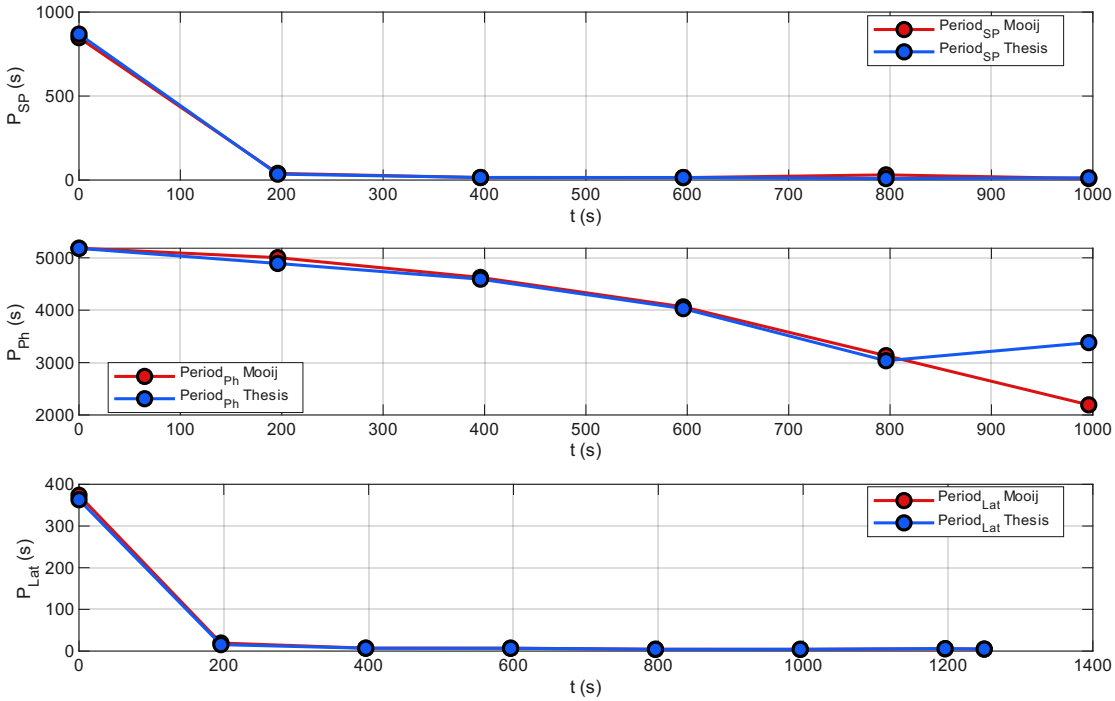

Figura 3.18: Periods along the trajectory

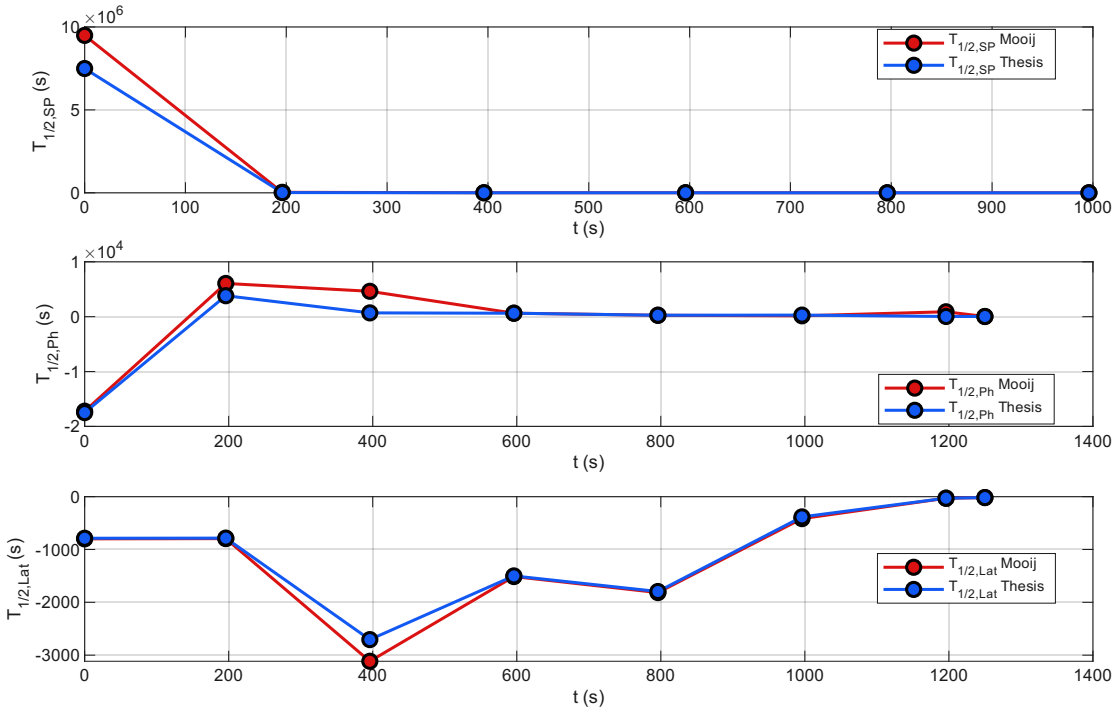

Figura 3.19: Halving time along the trajectory

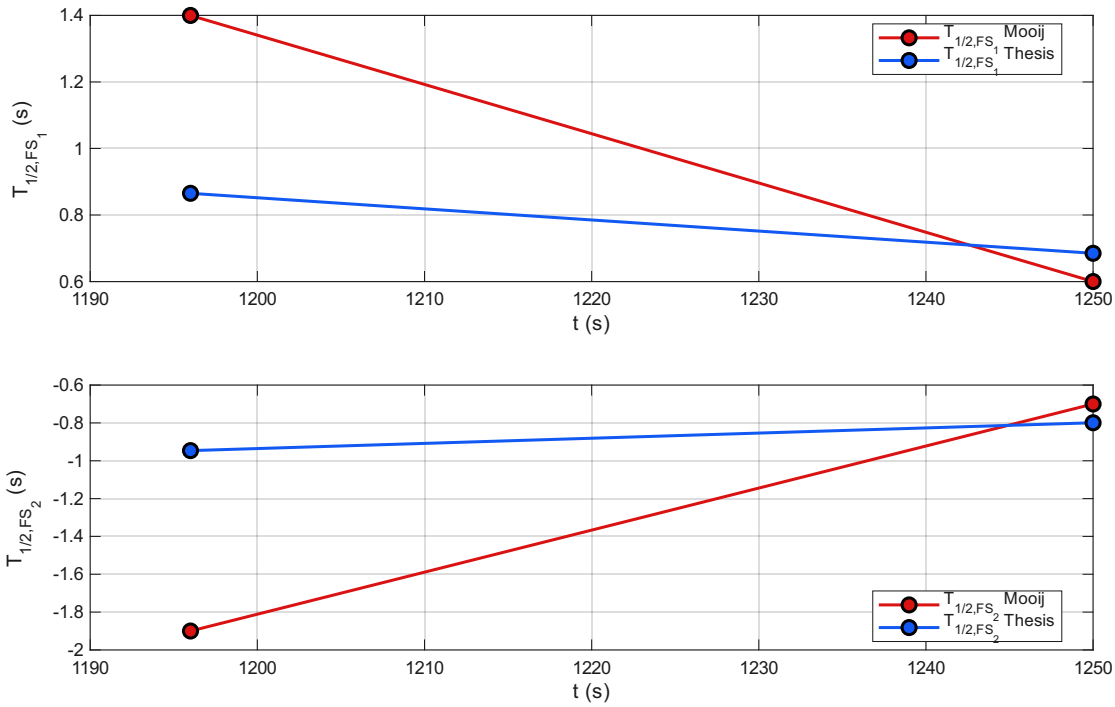

Figura 3.20: Halving time of the former short periods in the last two time points

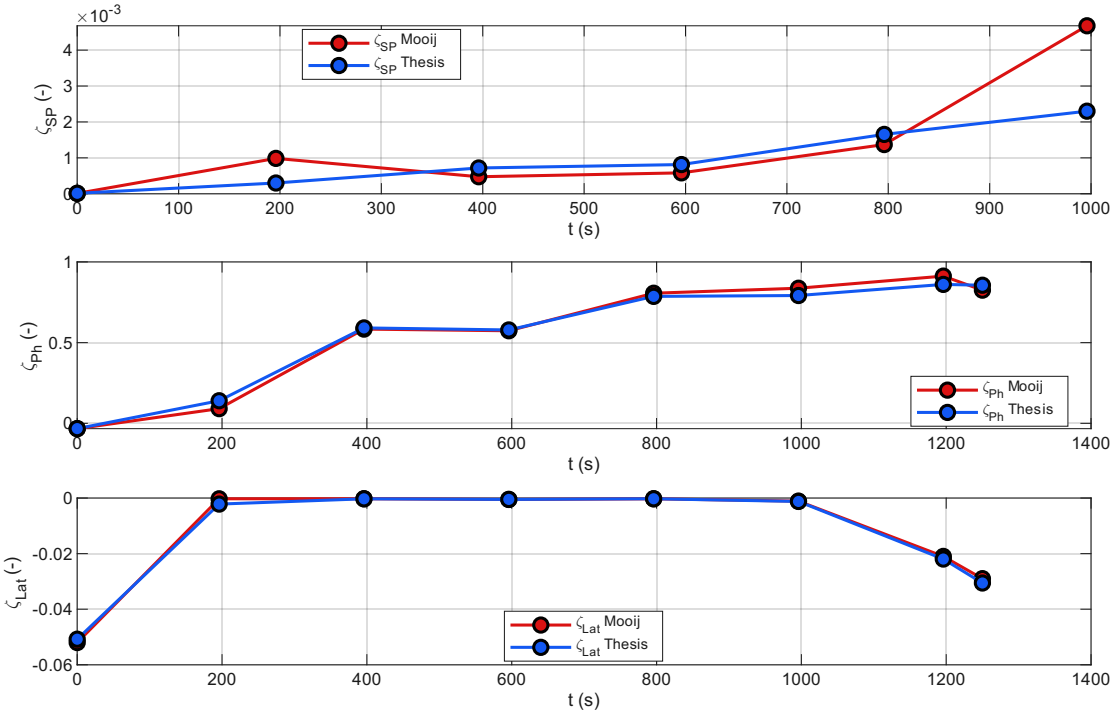

Figura 3.21: Damping along the trajectory

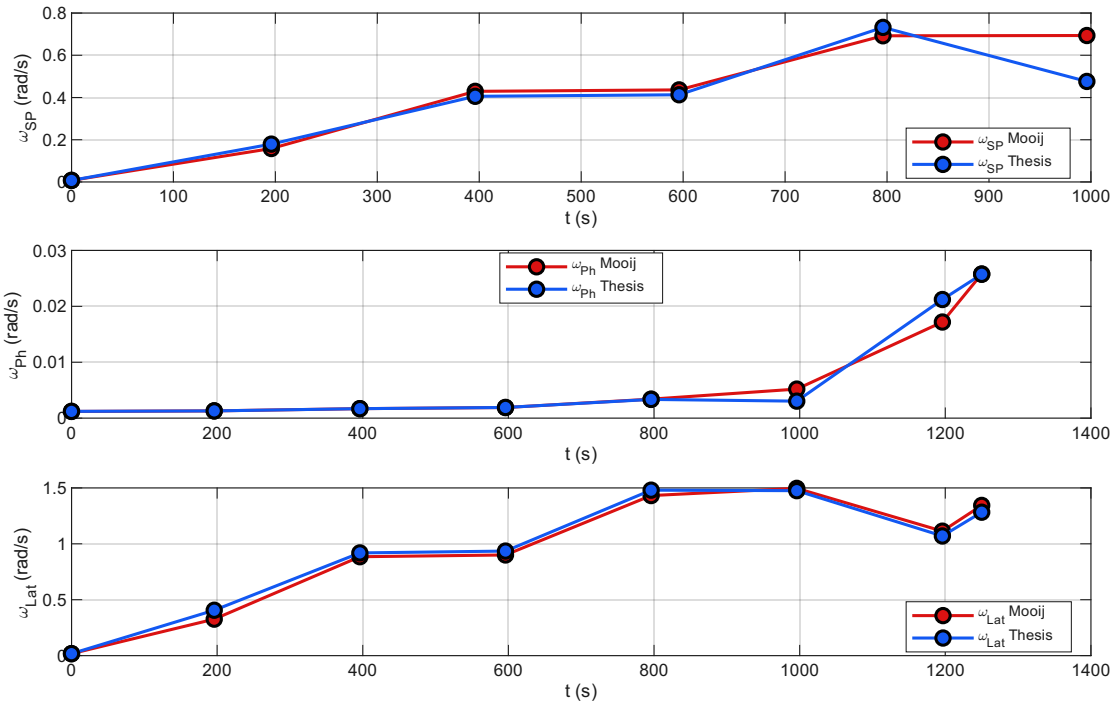

Figura 3.22: Natural frequency along the trajectory

Furthermore, the same eigenvalue pairs undergo a real–to–complex transition at coincident time points. In particular:

- From time point 50 (Tab.A.2) to time point 100 (Tab.A.3) the aperiodic-roll roots move from two distinct real values to a complex-conjugate pair, indicating the onset of a periodic roll divergence.
- From time point 150 (Tab.A.4) to time point 200 (Tab.A.5) the height/spiral mode exhibits an analogous real-to-complex transition, consistent with the emergence of a periodic roll mode.

3.5 Summary

Inspection of the matrix **A** shows that there are non-zero cross-coupling terms between the so-called symmetric variables V, γ, q, R, α and the asymmetric variables p, r, β, σ, implying that the corresponding motions are not fully decoupled. In chapter 5 we'll see decoupling is possible. In the present chapter, however, all coupling terms have been explicitly retained during the analysis and treated as non-zero, so that their influence on the dynamic behaviour is properly accounted for.

At this point, the qualitative behaviour of the modes matches the discussion given by Mooij[3][4], so the numerical implementation and the subsequent analysis can be considered reliable.

The **short–period** oscillation gradually changes character and becomes more similar to the short–period mode of a conventional aircraft. As the vehicle descends and aerodynamic forces grow, the mode becomes more heavily damped, while its period steadily decreases. Later along the trajectory, this oscillatory mode splits into two real (aperiodic) modes: one strongly damped and one strongly unstable. Towards the end of the flight, the influence of the bank angle on the short–period dynamics becomes increasingly pronounced, a trend that will also appear in the analysis of the phugoid mode.

The **phugoid** mode becomes progressively more damped along the trajectory, eventually behaving as a strongly damped oscillation, while its period steadily decreases. At the same time, the increasing use of bank angle for lateral-directional control causes its influence on the phugoid dynamics to become non-negligible. As a result, a small but appreciable coupling develops between the nominally symmetric phugoid motion and the asymmetric degrees of freedom.

The **lateral oscillation** is an unstable periodic mode, and it remains unstable over the entire trajectory. However, its characteristics evolve with time. At an intermediate stage the (negative) damping magnitude decreases, so the motion becomes less unstable for a while; later, the damping becomes more negative again

and the instability strengthens. Over the same interval, the oscillation period also undergoes a marked reduction.
The aperiodic **roll** modes switches into a single unstable periodic roll mode, weakly coupled to the angle of attack, and the perturbation in altitude becomes the dominant component. This transition occurs as soon as the vehicle starts banking. At the following analysis point, the mode splits again into two aperiodic modes, whose characteristics are very similar to those of the aperiodic height mode.

In this chapter, we analyzed the vehicle's open-loop dynamics. Our results reproduce those reported in the literature [4][3], with only minor differences attributable to trajectory uncertainty; the qualitative behavior remains unchanged. The next chapter examines the principal dynamic modes using literal approximations from the literature. This analysis is expected to corroborate the present results while clarifying which parameters most strongly influence the modes.

Capitolo 4

Model Approximations

This chapter develops literal (closed-form) approximations for the vehicle's principal dynamic modes, aiming to obtain analytical expressions for natural frequencies, damping ratios, and instability conditions. The approach relies on small-perturbation linearization and a frozen-time LTI representation along the trajectory, enabling transparent parameter dependencies on aerodynamic derivatives, inertial properties, and flight condition. After stating assumptions and the domain of validity, we derive approximations for the longitudinal and lateral–directional modes, identify the dominant terms, and assess the sensitivity to key parameters. A quantitative comparison with the numerical results of the previous chapter is then provided to evaluate accuracy, limitations, and predictive capability of the literal formulas.

First, the aerodynamic derivatives are scaled to ensure consistency with the equations of motion (EOM) adopted in the reference [6]. Throughout this chapter we employ the second-order formulation of the linearized EOM.
The resulting longitudinal equationsin second-order form appears as follows:

$$\begin{aligned} &\ddot{\Delta}V - X_u\dot{\Delta}V - (X_\alpha - g)\,\dot{\Delta}\alpha - (gZ_u/V_0)\,\Delta V - (gZ_\alpha/V_0)\,\Delta\alpha = 0 \\ &\ddot{\Delta}\alpha - (Z_u/V_0)\,\dot{\Delta}V - (M_q + Z_\alpha/V_0)\,\dot{\Delta}\alpha - [M_u - M_q\,(Z_u/V_0)]\,\Delta V \\ &- [M_\alpha - M_q\,(Z_\alpha/V_0)]\,\Delta\alpha = 0 \end{aligned} \tag{4.1}$$

The second-order equation for the lateral dynamics can be similarly derived as

follows:

$$
\begin{aligned}
\ddot{\Delta\beta} \;+\; & \Big[-\Big(N'_r\cos\alpha_0 - N'_p\sin\alpha_0\Big) - \frac{Y_\beta}{V_0}\Big]\dot{\Delta\beta} \\
+\; & \Big[\Big(N'_r\sin\alpha_0 + N'_p\cos\alpha_0\Big) - \frac{g}{V_0}\Big]\dot{\Delta\mu} \\
+\; & \Big[N'_\beta + \frac{Y_\beta}{V_0}\Big(N'_r\cos\alpha_0 - N'_p\sin\alpha_0\Big)\Big]\Delta\beta \\
+\; & \Big[\frac{g}{V_0}\Big(N'_r\cos\alpha_0 - N'_p\sin\alpha_0\Big)\Big]\Delta\mu \;=\; 0
\end{aligned}
\tag{4.2}
$$

$$
\begin{aligned}
\ddot{\Delta\mu} \;+\; & \Big[\Big(L'_r\cos\alpha_0 - L'_p\sin\alpha_0\Big)\Big]\dot{\Delta\beta} \;-\; \Big[\Big(L'_r\sin\alpha_0 + L'_p\cos\alpha_0\Big)\Big]\dot{\Delta\mu} \\
-\; & \Big[L'_\beta + \frac{Y_\beta}{V_0}\Big(L'_r\cos\alpha_0 - L'_p\sin\alpha_0\Big)\Big]\Delta\beta \\
-\; & \Big[\frac{g}{V_0}\Big(L'_r\cos\alpha_0 - L'_p\sin\alpha_0\Big)\Big]\Delta\mu \;=\; 0
\end{aligned}
$$

where

$$
\begin{aligned}
N'_\beta &= N_\beta\cos\alpha_0 - L_\beta\sin\alpha_0, \quad & L'_\beta &= L_\beta\cos\alpha_0 + N_\beta\sin\alpha_0, \\
N'_p &= N_p\cos\alpha_0 - L_p\sin\alpha_0, \quad & L'_p &= L_p\cos\alpha_0 + N_p\sin\alpha_0, \\
N'_r &= N_r\cos\alpha_0 - L_r\sin\alpha_0, \quad & L'_r &= L_r\cos\alpha_0 + N_r\sin\alpha_0.
\end{aligned}
\tag{4.3}
$$

Once the governing equations are established, the next step is to obtain the required aerodynamic derivatives by mapping the database coefficients into the coefficients

appearing in the EOM[7].

$$
\begin{aligned}
C_{X,0} &= -C_{D,0} \\
C_{X_u} &= -M \cdot C_{D_M} \\
C_{X_\alpha} &= -C_{D_\alpha}
\end{aligned}
$$

$$
\begin{aligned}
C_{Z,0} &= -C_{L,0} \\
C_{Z_u} &= -M \cdot C_{L_M} \\
C_{Z_\alpha} &= -C_{L_\alpha}
\end{aligned}
$$

$$
C_{m_u} = M \cdot C_{m_M}
$$

$$
\begin{aligned}
X_u &= \frac{q_{dyn}S}{mV_0}\left(2C_{X,0} + C_{X_u}\right) \\
X_w &= \frac{q_{dyn}S}{mV_0}C_{X_\alpha} \\
X_\alpha &= \frac{q_{dyn}S}{m}C_{X_\alpha}
\end{aligned}
\tag{4.4}
$$

$$
\begin{aligned}
Z_u &= \frac{q_{dyn}S}{mV_0}\left(2C_{Z,0} + C_{Z_u}\right) \\
Z_w &= \frac{q_{dyn}S}{mV_0}C_{Z_\alpha} \\
Z_\alpha &= \frac{q_{dyn}S}{m}C_{Z_\alpha}
\end{aligned}
$$

$$
\begin{aligned}
M_u &= \frac{q_{dyn}Sc}{I_yV_0}C_{m_u} \\
M_w &= \frac{q_{dyn}Sc}{I_yV_0}C_{m_\alpha} \\
M_\alpha &= \frac{q_{dyn}Sc}{I_y}C_{M_\alpha}
\end{aligned}
$$

$$Y_v = \frac{q_{dyn}S}{mV_0}C_{S_\beta}$$
$$L_v = \frac{q_{dyn}Sb}{I_xV_0}C_{l_\beta}$$
$$N_v = \frac{q_{dyn}Sb}{I_zV_0}C_{N_\beta}$$

All remaining derivatives vanish because, by assumption, the rate-damping coefficients are set to zero:

$$\begin{aligned} C_{l_p} &= 0 \\ C_{m_q} &= 0 \\ C_{n_r} &= 0 \end{aligned} \tag{4.5}$$

4.1 Stability criteria

We can observe the longitudinal static instability condition[6] S_{lon} during the trajectory.

$$(g/V_0)(Z_uM_\alpha - Z_\alpha M_u) = 0 \tag{4.6}$$

As shown in Fig.4.1, the static-instability indicator never crosses zero; hence no

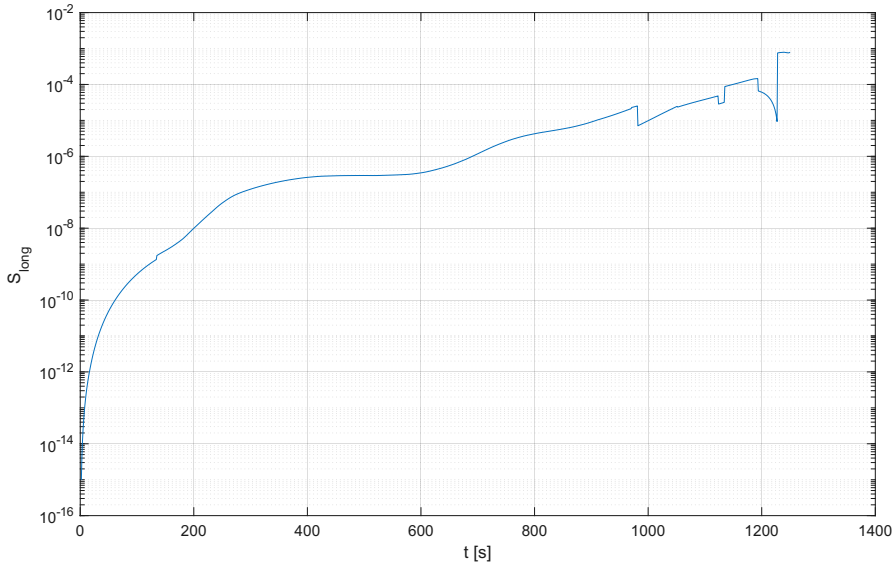

Figura 4.1: Static instability condition along the trajectory

onset of longitudinal static instability is predicted. Consistently, the eigenmotion analysis shows that both the short-period and phugoid modes remain dynamically stable (negative real parts). The small initial peak—approaching but not reaching

zero—coincides with the early segment where the phugoid exhibits a positive real part, i.e., a brief dynamic instability.
From the same reference[6], two static-instability criteria are available for the lateral dynamics.

$$\begin{aligned} S^1_{lat} &= (g/V_0)[(L'_\beta N'_r - N'_\beta L'_r)\cos\alpha_0 - (L'_\beta N'_p - N'_\beta L'_p)\sin\alpha_0] = 0 \\ S^2_{lat} &= (N'_\beta L'_p - L'_\beta N'_p)\cos\alpha_0 - (L'_\beta N'_r - N'_\beta L'_r)\sin\alpha_0 \\ &\quad + gL'_\beta/V_0 + (Y_\beta/V_0)(N'_r L'_p - L'_r N'_p) = 0 \end{aligned} \tag{4.7}$$

However, they cannot be applied here because, by hypothesis, all rate-damping derivatives are set to zero. (Under this assumption S^1_{lat} is always zero, while S^2_{lat} collapses to the trivial condition $gL'_\beta/V_0 = 0$).

4.2 Longitudinal modes

In this section, the principal features of the longitudinal motion are evaluated using literal approximations. Along the trajectory, some of the underlying assumptions are violated; where this occurs, discrepancies are expected and are discussed at the corresponding points.

- «It is next assumed that because the velocity varies per the slower phugoid mode, the rate of change of the perturbed velocity $\dot{\Delta}V$ during the short-period motion is negligible, that is, $\dot{\Delta}V \simeq 0$»[6]
- «However, if these two pairs of eigen- values (SP and P) approach each other in the complex plane,the assumption of zero rate of change of perturbed velocity will progressively worsen, and so will the accuracy of the literal approximation.»[6]

The short period damping and frequencies are given by:

$$\omega^2_{SP} = -[M_\alpha - M_q(Z_\alpha/V_0)], \quad 2\zeta_{SP}\omega_{SP} = -(M_q + Z_\alpha/V_0) \tag{4.8}$$

Under our assumptions they become

$$\omega_{SP} = \sqrt{-M_\alpha}, \quad \zeta_{SP} = -\frac{Z_\alpha/V_0}{2\omega_{SP}} \tag{4.9}$$

As we can observe in Fig.4.5 and Fig.4.6 the literal approximations reproduce the short-period behavior well, despite some violations of the above assumptions.
We now apply the same literal-approximation framework to the phugoid mode

$$\begin{aligned} \omega^2_P &= \frac{g(M_u Z_\alpha - M_\alpha Z_u)}{M_\alpha V_0 - M_q Z_\alpha} \\ 2\zeta_P\omega_P &= -X_u + (X_\alpha - g)\frac{M_u V_0 - M_q Z_u}{M_\alpha V_0 - M_q Z_\alpha} \end{aligned} \tag{4.10}$$

Under our assumptions they become

$$\begin{aligned} \omega_P^2 &= \frac{g(M_u Z_\alpha - M_\alpha Z_u)}{M_\alpha V_0} \\ 2\zeta_P \omega_P &= -X_u + (X_\alpha - g)\frac{M_u V_0}{M_\alpha V_0} \end{aligned} \tag{4.11}$$

As we can observe in Fig.4.7 and Fig.4.8 the literal approximations capture the phugoid behavior over most of the trajectory, with the exception of localized peaks in both the natural frequency and the damping ratio. For an oscillatory mode, the damping ratio must satisfy $0 \leq \zeta \leq 1$. The observed peaks likely stem from the absence of the damping derivatives, and their effect becomes more pronounced in the final portion of the trajectory, where aerodynamic forces increase.

At this point, since the literal approximation reproduces the short–period behaviour well even in the absence of an explicit damping coefficient, one may use the literal formula to determine the damping, taking as reference the results obtained from the modal analysis and from the inspection of matrix A. The idea is therefore to use $\omega_{SP,eig}$ in place of ω_{SP} so that from Eq.4.8 we obtain:

$$M_q = -2\zeta_{SP,eig}\omega_{SP,eig} - Z_\alpha/V_0 \tag{4.12}$$

The damping relation is chosen because it does not contain Z_α in the denominator; at the beginning of the trajectory is small and would make the result diverge. The evolution of this coefficient is shown in Fig.4.9.

4.3 Lateral Modes

For the lateral modes, the literal approximations are not used, since in this thesis the damping derivatives are assumed to be zero; however, these derivatives appear frequently in the literal formulae and would therefore lead to indeterminate or trivial solutions. Lateral stability is instead assessed by following the approach proposed by Connor S. Hoopes and Timothy T. Takahashi (Arizona State University, Tempe, AZ 85287)[1]. In that work, the so-called Evolved Bihrle–Weissman Chart (Fig.4.2) is employed, that is, a diagram in which the horizontal axis represents $C_{n_{\beta,dyn}}$ and the vertical axis represents the quantity $LCDP$. The former represents the dynamic directional stability, whereas the latter, the Lateral Control Departure Parameter (LCDP), is a measure of the effectiveness of the aerodynamic surfaces in providing lateral–directional control:

$$\begin{aligned} C_{n_{\beta DYN}} &= \frac{dC_n}{d\beta}\cos\alpha - \frac{dC_l}{d\beta}\left(\frac{I_{ZZ}}{I_{XX}}\right)\sin\alpha \\ LCDP &= \frac{dC_n}{d\beta} - \frac{dC_l}{d\beta}\cdot\frac{\frac{dC_n}{d\ aileron}}{\frac{dC_l}{d\ aileron}} \end{aligned} \tag{4.13}$$

An aircraft with positive directional static stability, $dC_n/d\beta > 0$, tends to cancel a lateral gust disturbance by generating a yawing moment. However, this response takes the aircraft away from straight-and-level flight. Therefore, the vehicle must also exhibit positive dynamic directional stability, $C_{n_{\beta DYN}} > 0$, producing a coupled roll–yaw response that slowly oscillates and brings the aircraft back to straight-and-level flight, thereby eliminating the lateral wind disturbance. Aircraft can exhibit

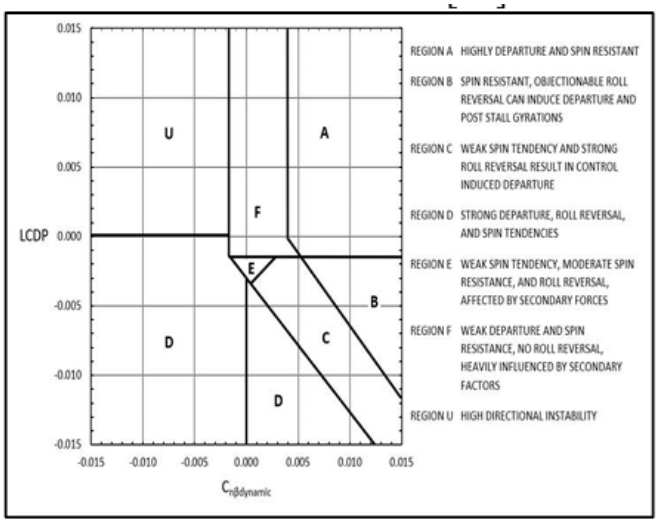

Figura 4.2: Evolved Bihrle–Weissman stability criteria screening chart. Red represents unfavorable flying qualities. Green represents favorable flying qualities. Yellow represents a region where secondary factors govern flying qualities.[1]

positive static but negative dynamic stability; this occurs when $dC_l/d\beta >> 0$. Conversely, they may have negative static but positive dynamic stability, i.e. $dC_l/d\beta << 0$, meaning that the dihedral effect is very strong. Since directional stability decreases with increasing Mach number, hypersonic configurations typically exploit a pronounced dihedral effect, characteristic of highly swept wings and high angle-of-attack flight.

To investigate the two coefficients, and in particular the LCDP, it is necessary to evaluate the derivatives of yawing and rolling moments with respect to aileron deflection. For the reference vehicle (HORUS2B), the elevons are used as ailerons. In the last part of the trajectory, however, the elevons are actually deflected symmetrically to compensate for trim that the body flap can no longer provide because it has reached its mechanical limit. For the present analysis the elevons are therefore assumed inactive ($\delta_e = 0°$) , and the derivatives are computed about this condition using the same procedure adopted in the previous chapter. Specifically, for each angle of attack and Mach number, a central difference is taken between $\delta_e = 10°$ and $\delta_e = -10°$. Figure 4.3 shows the results obtained from Space Shuttle

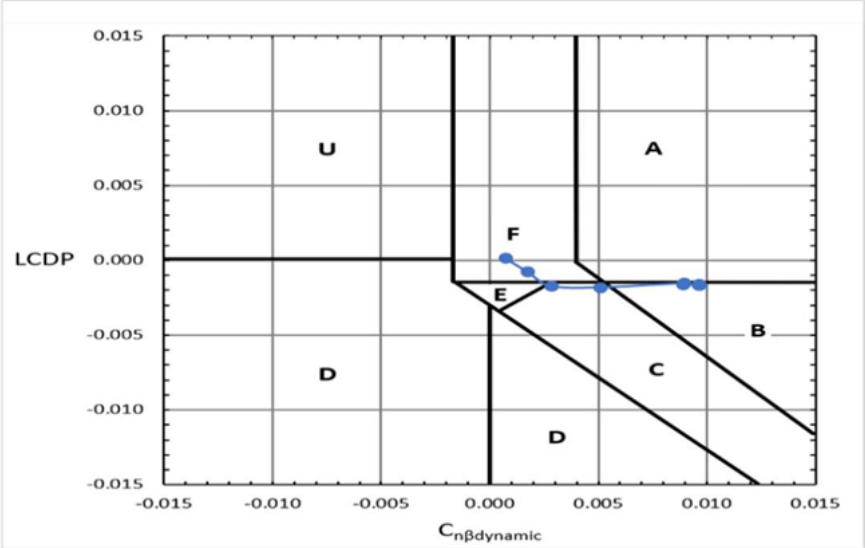

Figura 4.3: Evolved-Bihrle-Weissman Chart based on Shuttle Flight Test[1]

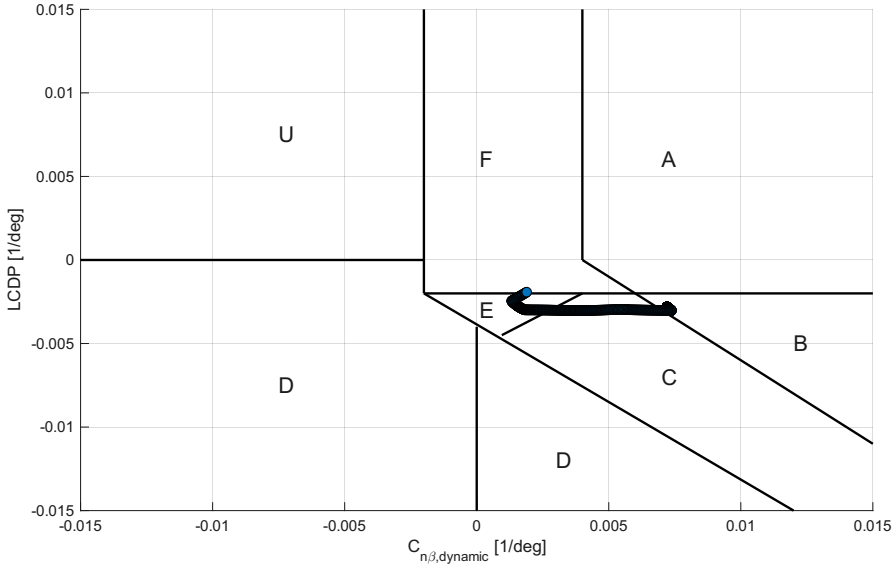

Figura 4.4: Evolved Bihrle-Weissman Chart based on HORUS2B

flight tests, whereas 4.4 presents the results derived in this thesis for the Horus2B vehicle. The qualitative behaviour is essentially the same and the same regions of the chart are traversed. This supports the validity of the present results, given the similarity between the two configurations (Space Shuttle and Horus2B):

- $I_z/I_x = 8.01$ for Space Shuttle [1]

- $I_z/I_x = 6.8$ for Horus2B

As we can see we find the same results of the reference[8]:

- At the highest Mach numbers, in the early part of re-entry when the dynamic pressure is low and the Orbiter is flown at a high nose-up attitude, the operating point lies close to the boundary between the stable region "A" and the unstable regions "B" and "C". In this regime $C_{n_{\beta,\mathrm{DYN}}}$ is strongly positive, whereas the open–loop (LCDP) is almost zero, indicating that closed–loop RCS control is required to maintain coordinated turns.

- As the vehicle decelerates and lowers its nose to enter the supersonic gliding phase, $C_{n_{\beta,\mathrm{DYN}}}$ decreases while (LCDP) remains close to zero. The operating point then moves along the boundary between the unfavourable regions "C" and "F", where large roll reversals can lead to control–induced departure or, at best, to only marginal departure and spin resistance.

The results obtained in this chapter are consistent with those presented in the previous and in the following chapters. In Chapter 3 a divergent lateral mode was observed along the entire trajectory. In the next chapter it will be shown that, for lateral control, the RCS thrusters must remain active throughout the trajectory in order to maintain adequate control of the vehicle.

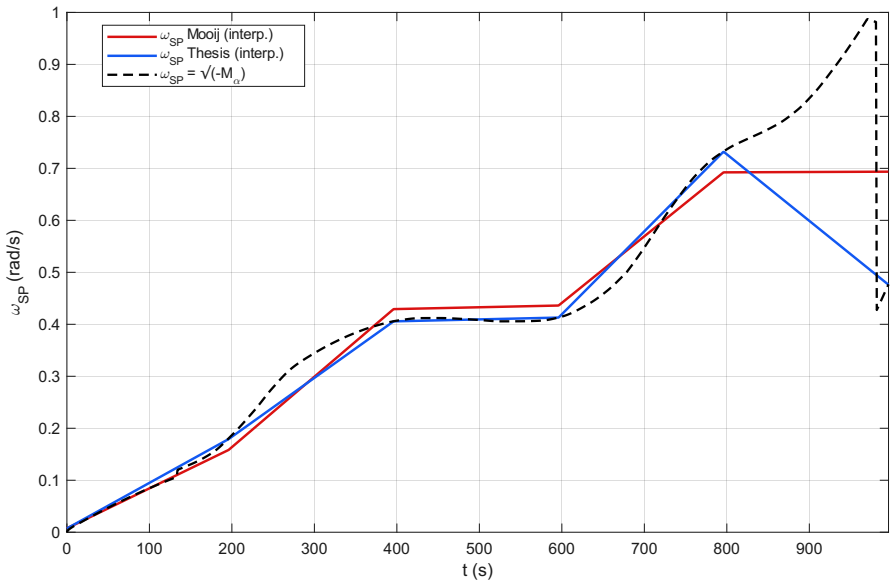

Figura 4.5: Short period frequency along the trajectory

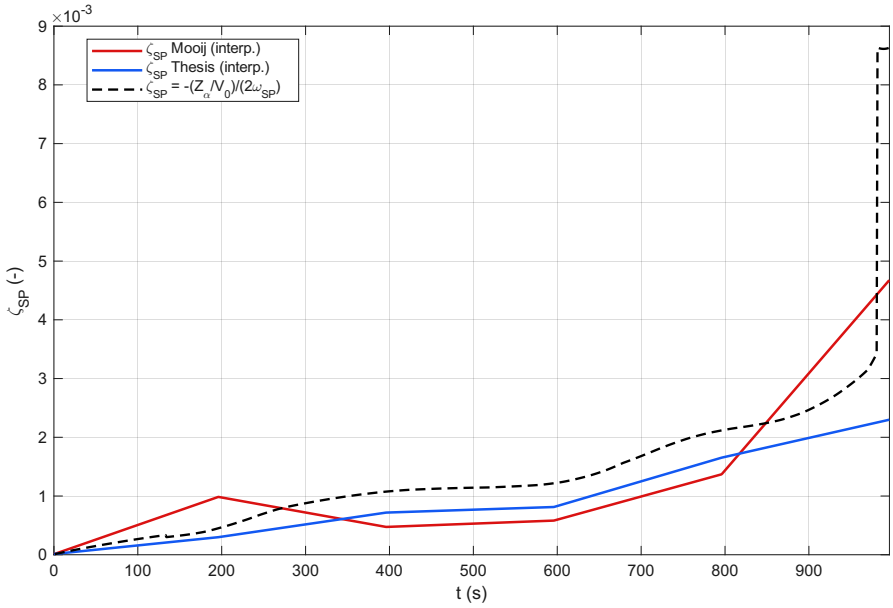

Figura 4.6: Short period damping along the trajectory

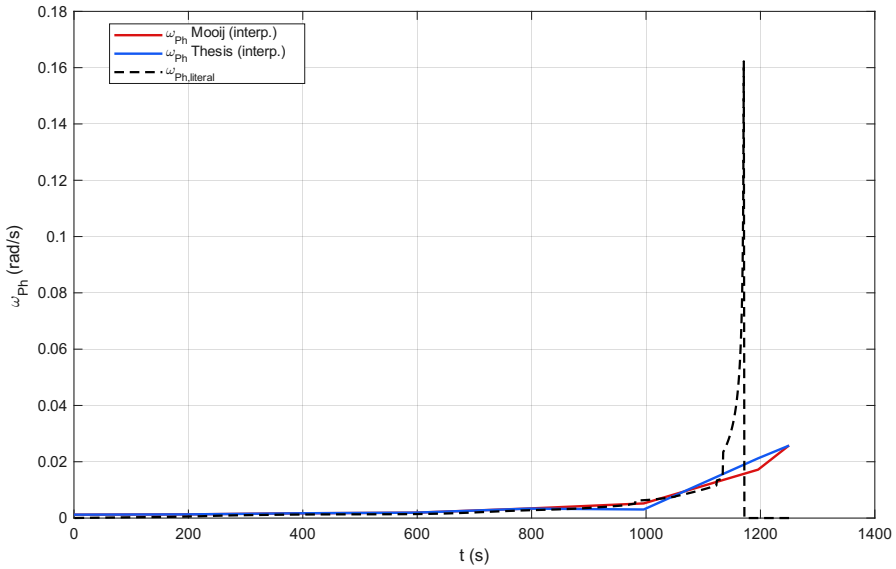

Figura 4.7: Phugoid frequency along the trajectory

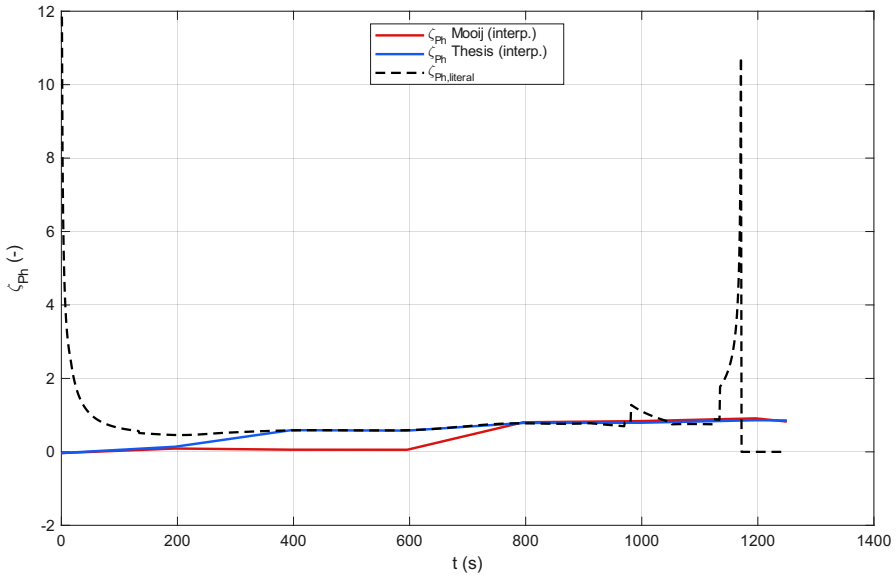

Figura 4.8: Phugoid frequency along the trajectory

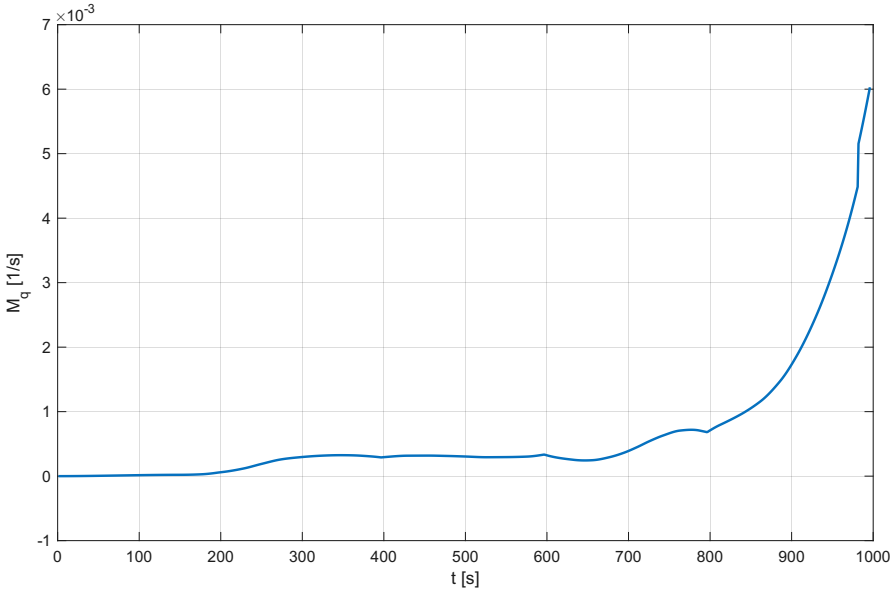

Figura 4.9: Pitch damping coefficient along the trajectory

Capitolo 5

LQR Control design

In this chapter, the vehicle controller will be analysed. First, the linearized and decoupled equations of the longitudinal and lateral–directional subsystems are derived and examined, and the feedback gains are computed by means of a Linear Quadratic Regulator (LQR). The response of the resulting linearized system is then analysed. Finally, the complete six-degree-of-freedom nonlinear model is implemented to investigate the behaviour of the vehicle along the reference trajectory.

5.1 Linear Quadratic Regulator (LQR)

Suppose[4], we have a state-space system given by

$$\begin{aligned} \dot{\mathbf{x}} &= A\mathbf{x} + B\mathbf{u} \\ \mathbf{y} &= C\mathbf{x} + D\mathbf{u} \end{aligned} \tag{5.1}$$

In case of state-feedback, the control law is given by

$$\mathbf{u} = -K\mathbf{x} \tag{5.2}$$

where K is a time independent feedback or gain matrix. This equations yields to

$$\dot{\mathbf{x}} = (A - BK)\,\mathbf{x} \tag{5.3}$$

The characteristic equation, which gives the eigenvalues and corresponding eigenmotion of the closed loop system is given by

$$det|A - BK - \lambda I| = 0 \tag{5.4}$$

As becomes obvious while studying the above equation, we can change the eigenvalues of the closed loop system by varying the gain matrix K. Whether the system will be controllable, however is not only depending on the values of these gains[4]. Let's break down two definitions:

- *Controllability*: Given a linear time-invariant system, the state $\mathbf{x}(\mathbf{t})$ is said to be controllable at $t = t_0$ if there exists a piece-wise continuous (and finite) input $\mathbf{u}(\mathbf{t})$ that will drive the state to any final state $\mathbf{x}(t_f)$ for a finite time $t_f \geq t_0$. If every state $\mathbf{x}(t_0)$ of the system is controllable in a finite time interval, the system is said to be completely state controllable or simply state controllable.

- *Observability*: Given a linear time-invariant system , the state $\mathbf{x}(t)$ is said to be observable if given any input $\mathbf{u}(t)$, there exist a finite time $t_f \geq t_0$ such that the knowledge of (i) $\mathbf{u}(t)$ for $t_0 \leq t < t_f$ (ii) the matrices $A,\ B,\ C$ and D and (iii) the output $\mathbf{y}(t)$ for $t_0 \leq t < t_f$, are sufficient to determine $\mathbf{x}(t_0)$. If every state of the system is observable for a finite time t_f , we say that the system is completely observable, or simply observable.

To check whether a system is controllable and observable, it is necessary and sufficient that the controllability matrix

$$[B, AB, A^2B, ..., A^{n-1}B] \tag{5.5}$$

and observability matrix

$$[C^T, A^TC^T, (A^T)^2C^T, ..., (A^T)^{n-1}C^T] \tag{5.6}$$

have a rank n, i.e., the dimension of the state vector $\mathbf{x}$. When not all of the eigenmotions are part of the observable and controllable state space, then only those eigenmotions that are part of it can be influenced by state feedback.
The gain matrix can be computed either by a direct method called *pole placement*, where the matrix K is computed such that closed loop performances are reached, or by an indirect method called *Quadratic Optimal Control* where a criterion cost matrix is minimised. In this thesis the last one is used.
The **cost matrix** is defined by

$$J = \int_0^\infty (\mathbf{x}^T Q\mathbf{x} + \mathbf{u}^T R\mathbf{u})\ dt \tag{5.7}$$

where the first term represents the control deviation end the second term represent the control effort. By varying Q and R more weight can be given to the control deviation, resulting in a faster response, or the control effort, giving smaller control signals. A good first choice is given by the *Bryson's Rule*:

$$\begin{aligned} Q &= diag\left[\frac{1}{\Delta x_{1_{max}}^2} + \frac{1}{\Delta x_{2_{max}}^2} + ... + \frac{1}{\Delta x_{n_{max}}^2}\right] \\ R &= diag\left[\frac{1}{\Delta u_{1_{max}}^2} + \frac{1}{\Delta u_{2_{max}}^2} + ... + \frac{1}{\Delta u_{n_{max}}^2}\right] \end{aligned} \tag{5.8}$$

where Δx_i is the maximum allowable amplitude of the i-th element of the state vector and Δu_i is the maximum allowable value of the j-th control.
To find an expression for K we substitute eq.5.2 in eq.5.7, which yields to

$$J = \int_0^\infty \mathbf{x}^T (Q + K^T R K)\mathbf{x}\ dt \tag{5.9}$$

To solve the above equation we treat the integrand as a fictious energy like

$$V(x) = \mathbf{x}^T P \mathbf{x} \tag{5.10}$$

Now by substituing and differentiating the above equations we get the final equation to get the matrix P, also known as the **Riccati equation** (all the mathematical details are reffered to [4]):

$$A^T P + PA - PBR^{-1}BP + Q = 0 \tag{5.11}$$

Once we get P, the matrix K follows from

$$P = Q + K^T R K \tag{5.12}$$

Fortunately, several software tools, such as MATLAB, can compute this equation once the matrices A, B, Q, and R are specified.

5.2 Longitudinal controller

To decouple the pitch motion from the lateral motion, the perturbations $\Delta\beta$ and $\Delta\sigma$ are set to zero. In addition, only the rotational dynamics are considered, so the contributions of ΔV, $\Delta\gamma$ and ΔR are neglected. This is justified because the translational dynamics evolve at much lower frequencies than the high-frequency rotational dynamics. Under these approximations, the following system is obtained

$$\begin{aligned}\Delta\dot{q} &= \frac{1}{I_y}\left(\frac{\partial C_m}{\partial\alpha}\Delta\alpha + \frac{\partial C_m}{\partial\delta_e}\Delta\delta_e\right) q_{dyn} S c + \frac{\Delta M_y}{I_y} \\ \Delta\dot{\alpha} &= \Delta q - \frac{1}{mV}\frac{\partial C_L}{\partial\alpha} q_{dyn} S \Delta\alpha\end{aligned} \tag{5.13}$$

The elevon deflection angle δ_e is defined as the symmetric combination of the left and right elevon, i.e.,

$$\delta_e = \frac{\delta_{e,l} + \delta_{e,r}}{2} \tag{5.14}$$

In the state-space form the above system can be written as

$$\begin{bmatrix}\Delta\dot{q} \\ \Delta\dot{\alpha}\end{bmatrix} = \begin{bmatrix}0 & \frac{1}{I_{yy}}\frac{\partial C_m}{\partial\alpha} q_{\text{dyn}} S_{\text{ref}} c_{\text{ref}} \\ 1 & -\frac{1}{mV_0}\frac{\partial C_L}{\partial\alpha} q_{\text{dyn}} S_{\text{ref}}\end{bmatrix}\begin{bmatrix}\Delta q \\ \Delta\alpha\end{bmatrix} + \begin{bmatrix}\frac{1}{I_{yy}}\frac{\partial C_m}{\partial\delta_e} q_{\text{dyn}} S_{\text{ref}} c_{\text{ref}} & \frac{1}{I_{yy}} \\ 0 & 0\end{bmatrix}\begin{bmatrix}\Delta\delta_e \\ \Delta T_y\end{bmatrix}. \tag{5.15}$$

so the matrices A and B are equal to

$$\begin{aligned}A &= \begin{bmatrix}0 & \frac{1}{I_{yy}}\frac{\partial C_m}{\partial\alpha} q_{\text{dyn}} S_{\text{ref}} c_{\text{ref}} \\ 1 & -\frac{1}{mV_0}\frac{\partial C_L}{\partial\alpha} q_{\text{dyn}} S_{\text{ref}}\end{bmatrix} \\ B &= \begin{bmatrix}\frac{1}{I_{yy}}\frac{\partial C_m}{\partial\delta_e} q_{\text{dyn}} S_{\text{ref}} c_{\text{ref}} & \frac{1}{I_{yy}} \\ 0 & 0\end{bmatrix}\end{aligned} \tag{5.16}$$

Recalling Chapter 3, where the eigenvalues of the homogeneous state equation were computed, the same analysis is now carried out for the simplified system , flying along the nominal trajectory. The results are reported in Figs.5.1-5.4. A comparison with the corresponding plots in chapter 3 reveals a similar behaviour of the eigenvalues, confirming that the decoupling of the two types of motion is justified. The eigenmotion shown in Fig. 5.1 corresponds to the short-period mode. Neglecting the translational motion has therefore not affected this mode, and the assumption of frequency separation is validated.

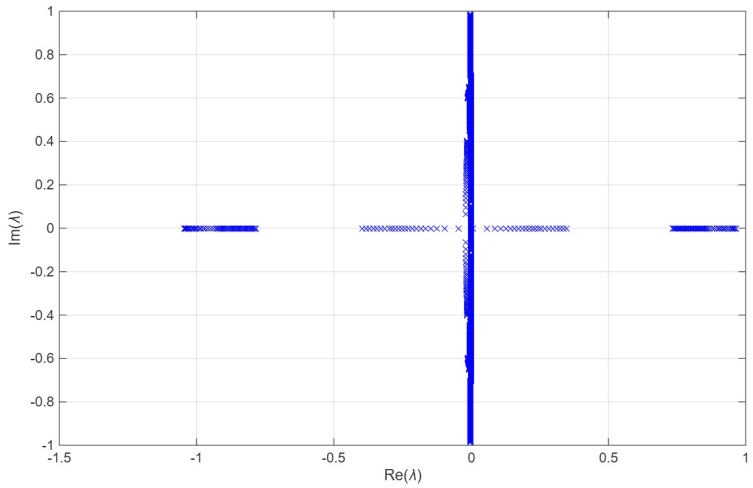

Figura 5.1: Variation of the eignevalues of longitudinal motion along the trajectory

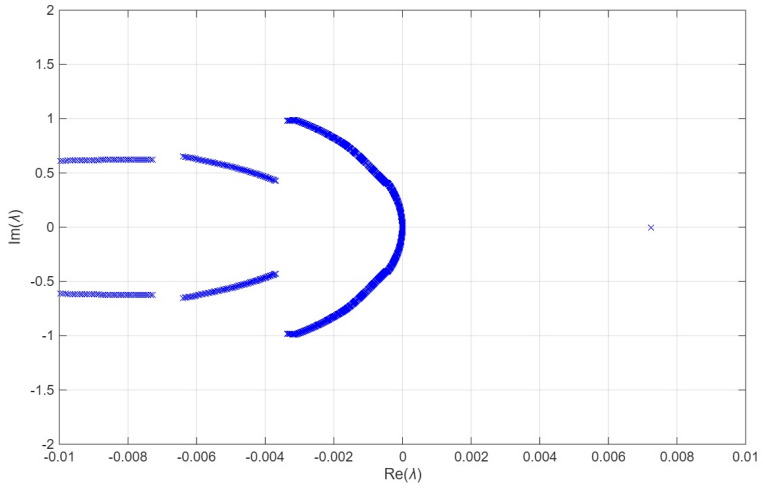

Figura 5.2: Details around the origin of the eignevalues of longitudinal motion along the trajectory

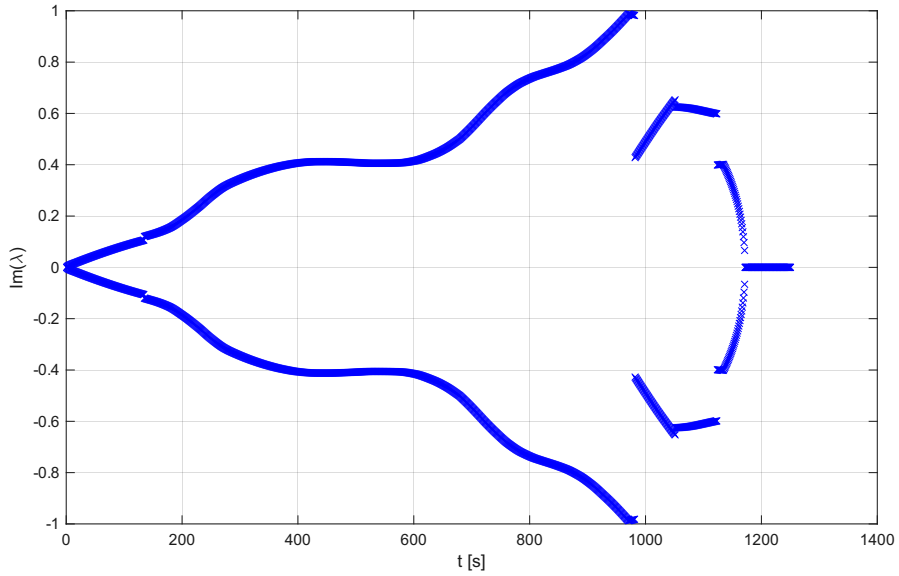

Figura 5.3: Variation of the imaginary parts of the eignevalues of longitudinal motion along the trajectory

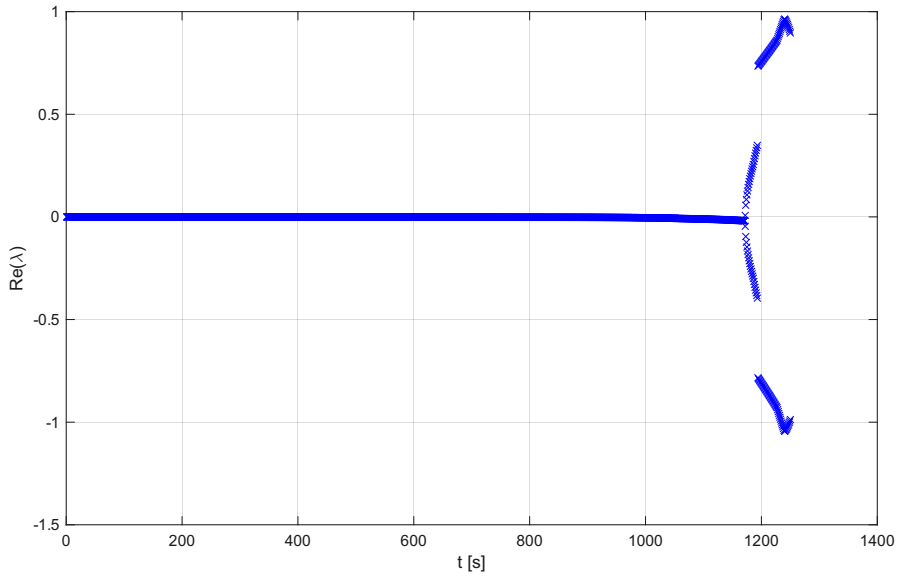

Figura 5.4: Variation of the real parts of the eignevalues of longitudinal motion along the trajectory

The selection of the control mode follows from dynamic pressure and Mach constraints (Fig.5.5). As we can see the yaw thrusters will always be avaible since in this thesis we never reach $M < 1$. Furthermore we use the cost criterion in table 5.1. We can individuate three phases for the control mode:

1. Only RCS control mode
2. Hybrid control mode
3. Only surfaces control mode

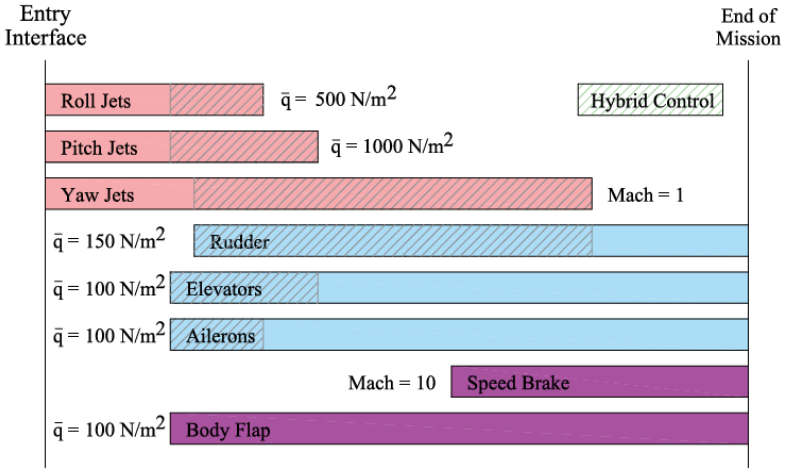

Figura 5.5: Entry control modes for HORUS[3]

	RCS	Hybrid	Aero
Δq_{max}	1.5 °/s	1.5 °/s	4 °/s
$\Delta \alpha_{max}$	1 °	2.5 °	2 °

Tabella 5.1: Cost criterion longitudinal controller

At this point we can compute the gains along the trajectory. This gains we'll be used for a simple proportional law of the form:

$$\Delta \mathbf{u} = -K \Delta \mathbf{x} \tag{5.17}$$

in particular

$$\begin{aligned} \Delta \delta_e &= -K_{e1} \Delta q - K_{e2} \Delta \alpha \\ \Delta M_{T,y} &= -K_{y1} \Delta q - K_{y2} \Delta \alpha \end{aligned} \tag{5.18}$$

where

$\Delta q = q - q_c \ (rad/s)$,
$\Delta \alpha = \alpha - \alpha_c \ (rad)$,

with q_c = commanded pitch rate and α_c = commanded angle of attack.

At this point, the gains can be computed along the trajectory. As shown in Figs. 5.6 and 5.7, these gains vary significantly due to the large variation in dynamic pressure. Therefore, the gain interpolation must be carried out carefully in order to avoid actuator command spikes and a potentially divergent control response.
To examine the behaviour of the linearized system, the vehicle is commanded to perform a 1° step increase in angle of attack at two different time instants, ($t_1 = 50\,\mathrm{s}$) and ($t_2 = 900\,\mathrm{s}$). The feedback gains are set to $K(t_1)$ and $K(t_2)$, respectively. As can be seen in Figs.5.8,5.9 the system responds very well, with a steady-state error of only $0.2\,^\circ$ and $0.1\,^\circ$ for time t_1 and t_2 respectively.

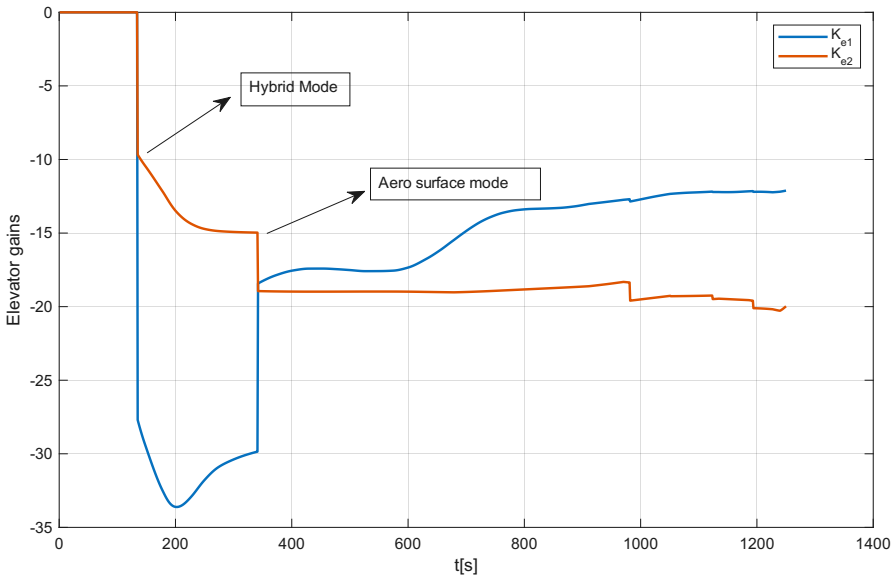

Figura 5.6: Elevator gains along the trajectory

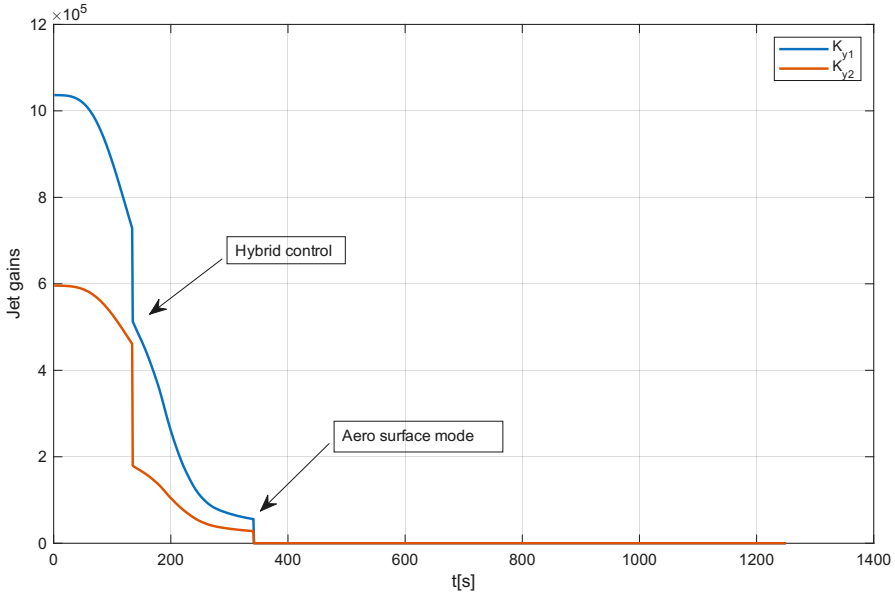

Figura 5.7: Jet gains along the trajectory

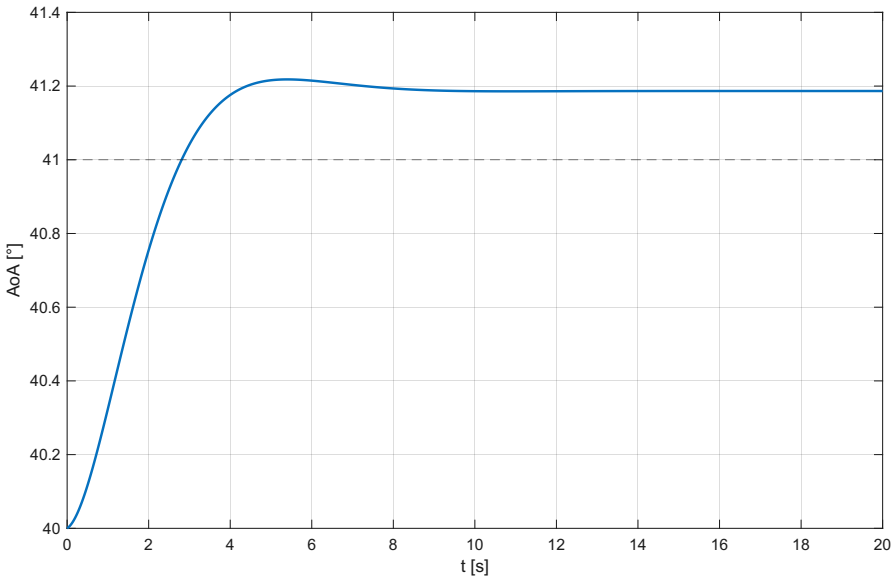

Figura 5.8: Step response at $t = 50\,\mathrm{s}$

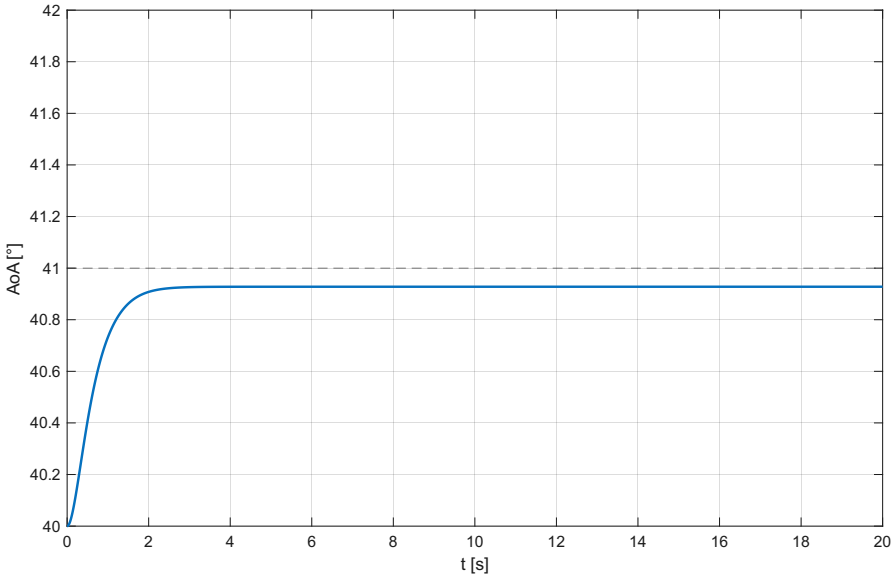

Figura 5.9: Step response at $t = 900\,\mathrm{s}$

5.3 Lateral controller

As for the longitudinal controller, the same type of analysis is now carried out for the lateral controller. To investigate the lateral rotational dynamics, i.e. the time evolution of β and σ, the symmetric motion (variation of α with time) is excluded by setting $\Delta\alpha = 0$ and neglecting the translational motion. The resulting system is

$$\Delta\dot{p} = \frac{1}{I_{xx}}\left(\frac{\partial C_l}{\partial\beta}\,\Delta\beta + \frac{\partial C_l}{\partial\delta_a}\,\Delta\delta_a\right)\bar{q}_e S_{\text{ref}} b_{\text{ref}} + \frac{\Delta M_{T,x}}{I_{xx}}, \tag{5.19}$$

$$\Delta\dot{r} = \frac{1}{I_{zz}}\left(\frac{\partial C_n}{\partial\beta}\,\Delta\beta + \frac{\partial C_n}{\partial\delta_a}\,\Delta\delta_a + \frac{\partial C_n}{\partial\delta_r}\,\Delta\delta_r\right)\bar{q}_e S_{\text{ref}} b_{\text{ref}} + \frac{\Delta M_{T,z}}{I_{zz}}, \tag{5.20}$$

$$\Delta\dot{\beta} = \sin\alpha_e\,\Delta p - \cos\alpha_e\,\Delta r - \frac{g_e}{V_e}\cos\gamma_e\cos\sigma_e\,\Delta\sigma, \tag{5.21}$$

$$\Delta\dot{\sigma} = -\cos\alpha_e\,\Delta p - \sin\alpha_e\,\Delta r + \left(\frac{g_e}{V_e}\cos\gamma_e\cos\sigma_e - \frac{L_e}{mV_e}\right)\Delta\beta + \frac{\tan\gamma_e}{mV_e}\cos\sigma_e L_e\,\Delta\sigma. \tag{5.22}$$

Since damping derivatives such as C_{l_p} and C_{n_r} are not included in the present aerodynamic model, the corresponding terms are absent from the equations, therefore there is no natural damping. The available controls consist of the aileron, rudder, roll jets and yaw jets.
The aileron deflection angle δ_a is defined as the asymmetric combination of the left and right elevon, i.e.,

$$\delta_a = \frac{\delta_{e,l} - \delta_{e,r}}{2} \tag{5.23}$$

The rudder deflection angle δ_r is modelled such that only one of the two rudders can move at a time, and only outward, corresponding to a positive deflection. In particular

$$\begin{cases} \text{if} & \delta_r < 0,\ \delta_r = \delta_{r,r} \\ \text{else} & \delta_r > 0,\ \delta_r = \delta_{r,l} \end{cases} \tag{5.24}$$

In the state-space form, the above equations are written as

$$\begin{bmatrix} \Delta\dot{p} \\ \Delta\dot{r} \\ \Delta\dot{\beta} \\ \Delta\dot{\sigma} \end{bmatrix} = \mathbf{A}\begin{bmatrix} \Delta p \\ \Delta r \\ \Delta\beta \\ \Delta\sigma \end{bmatrix} + \mathbf{B}\begin{bmatrix} \Delta\delta_a \\ \Delta\delta_r \\ \Delta T_x \\ \Delta T_z \end{bmatrix}. \tag{5.25}$$

with

$$\mathbf{A} = \begin{bmatrix} 0 & 0 & \frac{1}{I_{xx}}\frac{\partial C_l}{\partial \beta} q_{\text{dyn}} S_{\text{ref}} b_{\text{ref}} & 0 \\ 0 & 0 & \frac{1}{I_{zz}}\frac{\partial C_n}{\partial \beta} q_{\text{dyn}} S_{\text{ref}} b_{\text{ref}} & 0 \\ \sin\alpha_0 & -\cos\alpha_0 & 0 & -\frac{g_0}{V_0}\cos\gamma_0\cos\sigma_0 \\ -\cos\alpha_0 & -\sin\alpha_0 & \frac{g_0}{V_0}\cos\gamma_0\cos\sigma_0 - \frac{L_0}{mV_0} & \frac{\tan\gamma_0}{mV_0}\cos\sigma_0 L_0 \end{bmatrix}. \tag{5.26}$$

and

$$\mathbf{B} = \begin{bmatrix} \frac{1}{I_{xx}}\frac{\partial C_l}{\partial \delta_a} q_{\text{dyn}} S_{\text{ref}} b_{\text{ref}} & 0 & \frac{1}{I_{xx}} & 0 \\ \frac{1}{I_{zz}}\frac{\partial C_n}{\partial \delta_a} q_{\text{dyn}} S_{\text{ref}} b_{\text{ref}} & \frac{1}{I_{zz}}\frac{\partial C_n}{\partial \delta_r} q_{\text{dyn}} S_{\text{ref}} b_{\text{ref}} & 0 & \frac{1}{I_{zz}} \\ 0 & 0 & 0 & 0 \\ 0 & 0 & 0 & 0 \end{bmatrix}. \tag{5.27}$$

As done for the longitudinal motion, the eigenvalues of the lateral reduced system are now examined along the trajectory to see whether their evolution changes significantly. By comparing these eigenvalue histories with those of the full model, the assumption of decoupled symmetric and asymmetric motion can be validated. The differences between the corresponding eigenplots should be found in an absence of the symmetric motion and the neglected terms of the translational motion. The resulst are shown in figs.5.10-5.13.

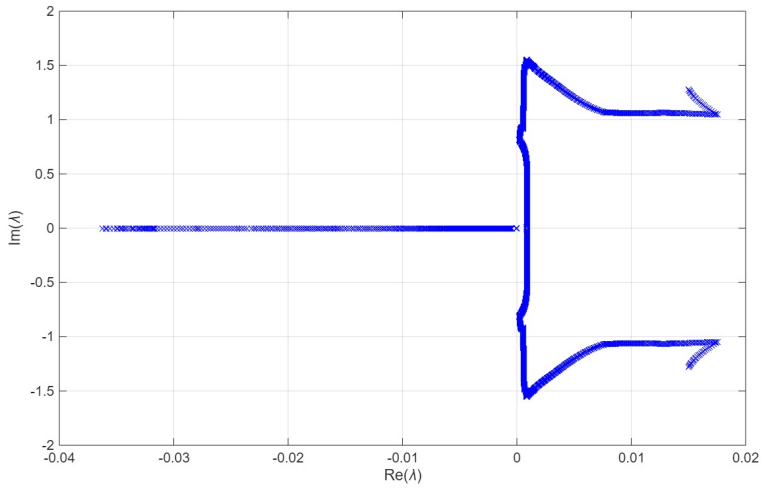

Figura 5.10: Variation of the eignevalues of lateral motion along the trajectory

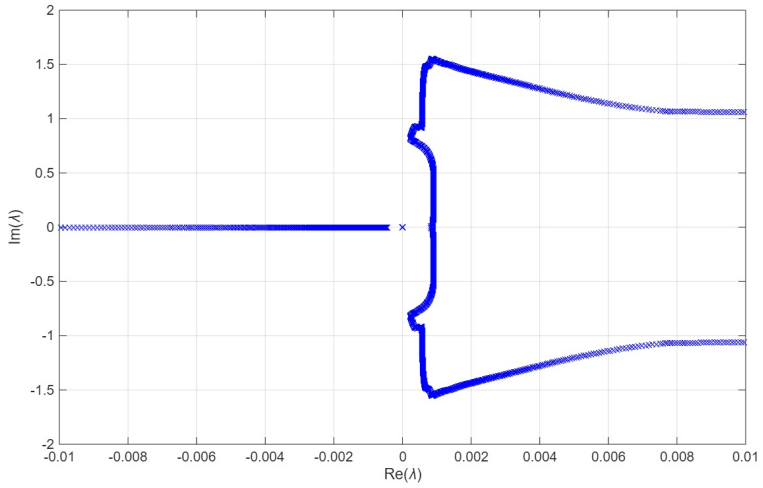

Figura 5.11: Details around the origin of the eignevalues of lateral motion along the trajectory

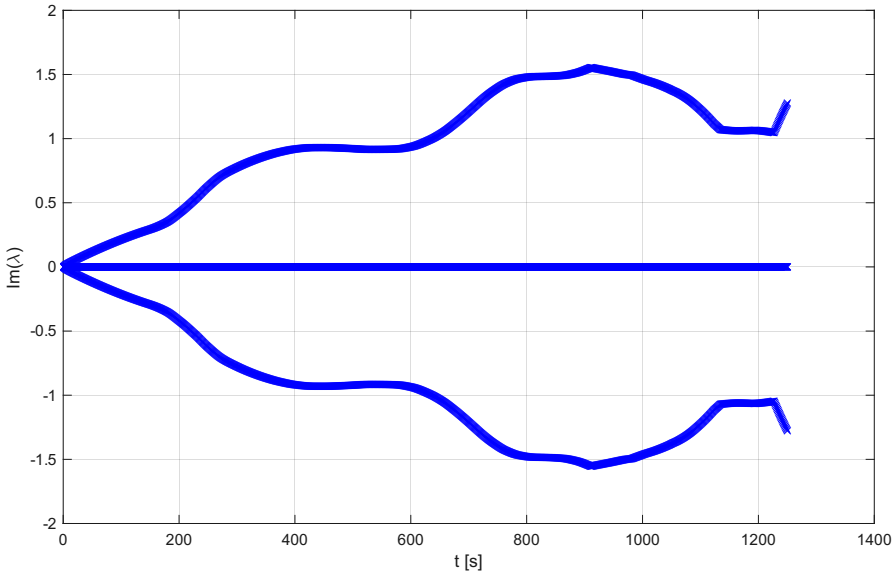

Figura 5.12: Variation of the imaginary parts of the eignevalues of lateral motion along the trajectory

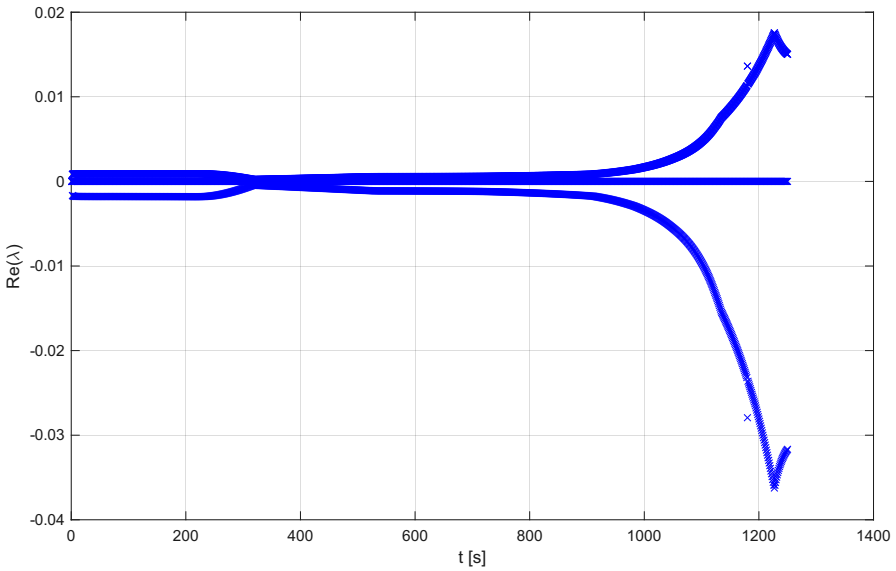

Figura 5.13: Variation of the real parts of the eignevalues of lateral motion along the trajectory

As we did for the longitudinal controller we can choose some constraints for the weigth matrices of the LQR (based on the literature[3]) Once the matrices

Tabella 5.2: Definition of weighting terms for the HORUS lateral controller

	Roll control		Yaw control	
	$\Delta p_{\max}$ (°/s)	$\Delta \sigma_{\max}$ (°)	$\Delta r_{\max}$ (°)	$\Delta \beta_{\max}$ (°)
RCS	1.5	4	0.5	2
Hybrid	4	4	5	2
Aero	10	10	5	2

A, B, Q, R have been defined, the LQR feedback gains can be computed. As shown in Figs. 5.14–5.17, these gains vary significantly along the trajectory, both because of the different control modes (RCS only, hybrid, and purely aerodynamic) and because of the strong variation in dynamic pressure. As in the longitudinal case, the interpolation of the controller gains must therefore be carried out carefully when selecting the gains to be used.

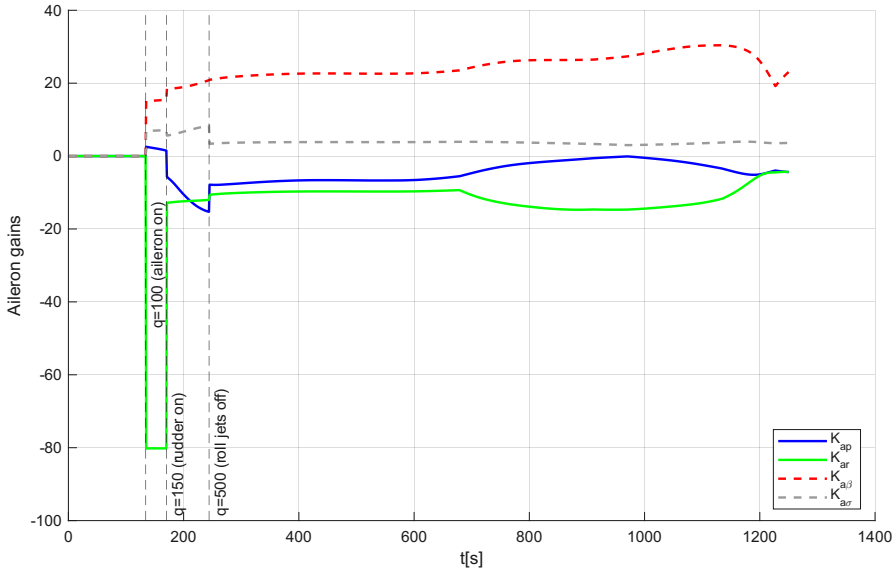

Figura 5.14: Ailerons gains along the trajectory

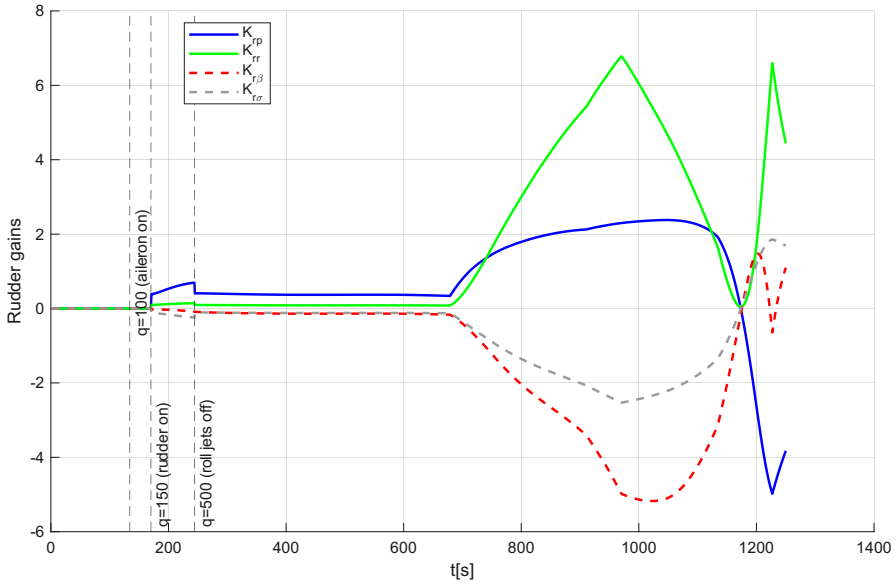

Figura 5.15: Rudders gains along the trajectory

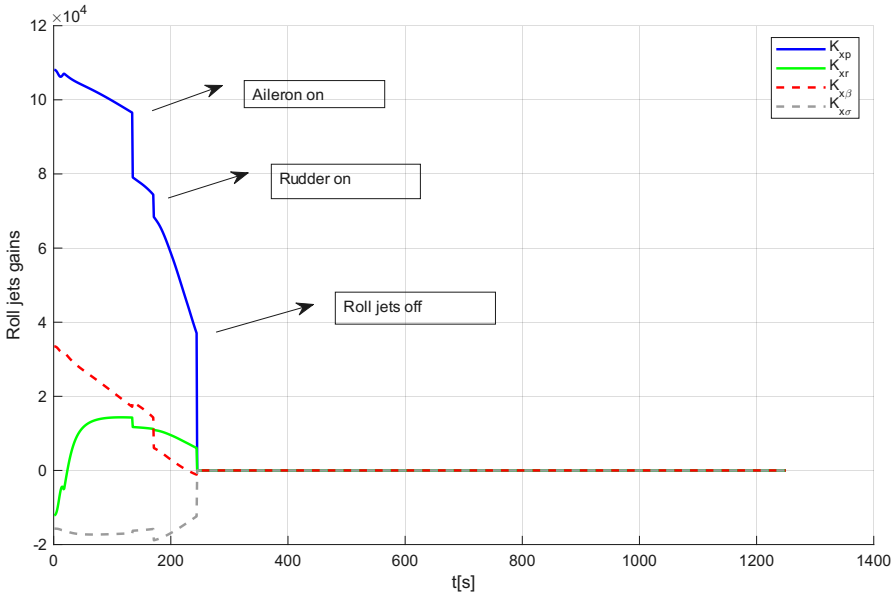

Figura 5.16: Roll jets gains along the trajectory

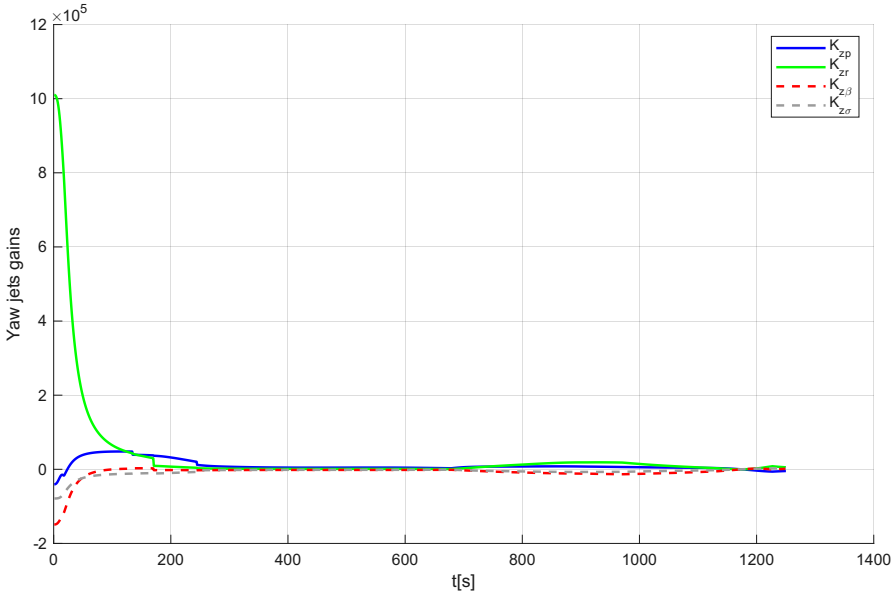

Figura 5.17: Yaw jets gains along the trajectory

Then we can implement a simple proportional control law like:

$$\begin{aligned}
\Delta\delta_a &= -K_{ap}\Delta p - K_{ar}\Delta r - K_{a\beta}\Delta\beta - K_{a\sigma}\Delta\sigma \\
\Delta\delta_r &= -K_{rp}\Delta p - K_{rr}\Delta r - K_{r\beta}\Delta\beta - K_{r\sigma}\Delta\sigma \\
\Delta M_{T,x} &= -K_{xp}\Delta p - K_{xr}\Delta r - K_{x\beta}\Delta\beta - K_{x\sigma}\Delta\sigma \\
\Delta M_{T,z} &= -K_{zp}\Delta p - K_{zr}\Delta r - K_{z\beta}\Delta\beta - K_{z\sigma}\Delta\sigma
\end{aligned} \tag{5.28}$$

or in matrix form

$$\begin{bmatrix} \Delta\delta_a \\ \Delta\delta_r \\ \Delta M_{T,x} \\ \Delta M_{T,y} \end{bmatrix} = - \begin{bmatrix} K_{ap} & K_{ar} & K_{a\beta} & K_{a\sigma} \\ K_{rp} & K_{rr} & K_{r\beta} & K_{r\sigma} \\ K_{xp} & K_{xr} & K_{x\beta} & K_{x\sigma} \\ K_{zp} & K_{zr} & K_{z\beta} & K_{z\sigma} \end{bmatrix} \begin{bmatrix} \Delta p \\ \Delta r \\ \Delta\beta \\ \Delta\sigma \end{bmatrix} \tag{5.29}$$

where

- $\Delta p = p - p_c$, with p_c commanded pitch rate
- $\Delta r = r - r_c$, with r_c commanded yaw rate
- $\Delta\beta = \beta - \beta_c$, with β_c commanded sideslip angle (nominally zero)
- $\Delta\sigma = \sigma - \sigma_c$, with σ_c commanded bank angle

As for the longitudinal controller, we now analyse the response of the lateral system to a step command of $\Delta\sigma = 1\,^\circ$. As shown in Figs. 5.18 and 5.19, the overshoot is reduced and the commanded bank angle is tracked accurately. However, a small steady-state error in β, remains, due to the low dynamic pressure and the weak aerodynamic damping. Conversely, in Figs. 5.20 and 5.21 a larger overshoot and a longer settling time are observed, although the commanded angle is eventually reached and the disturbance in β is eliminated.

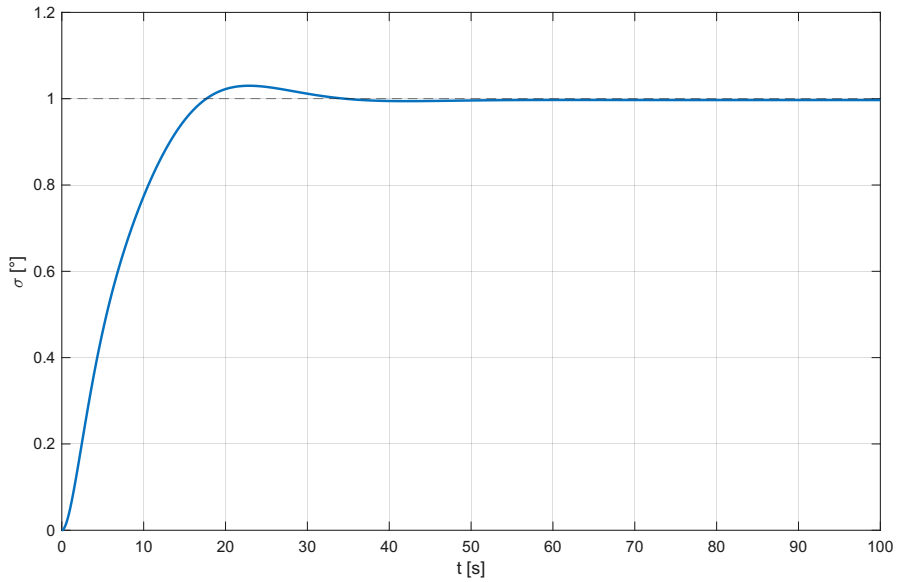

Figura 5.18: Step response at $t = 50\,\mathrm{s}$

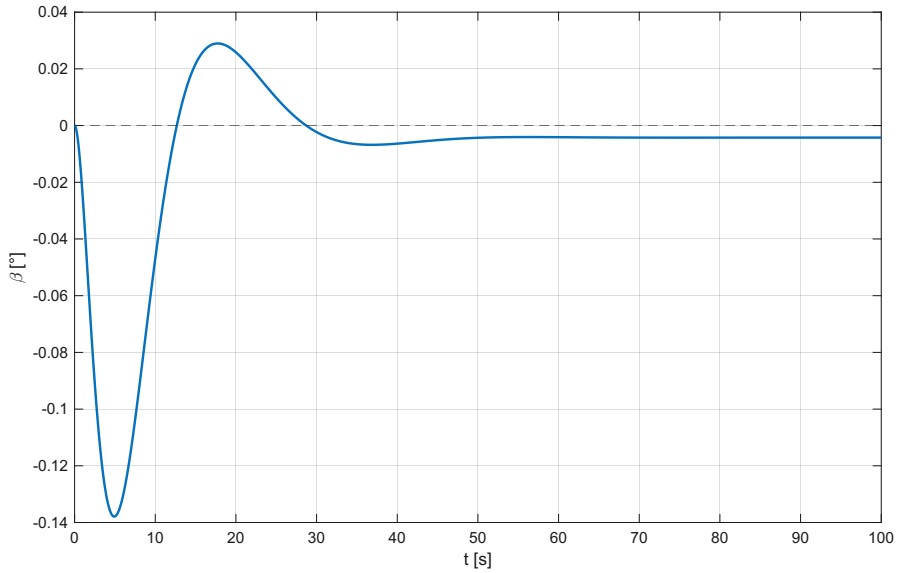

Figura 5.19: β response at $t = 50\,\mathrm{s}$

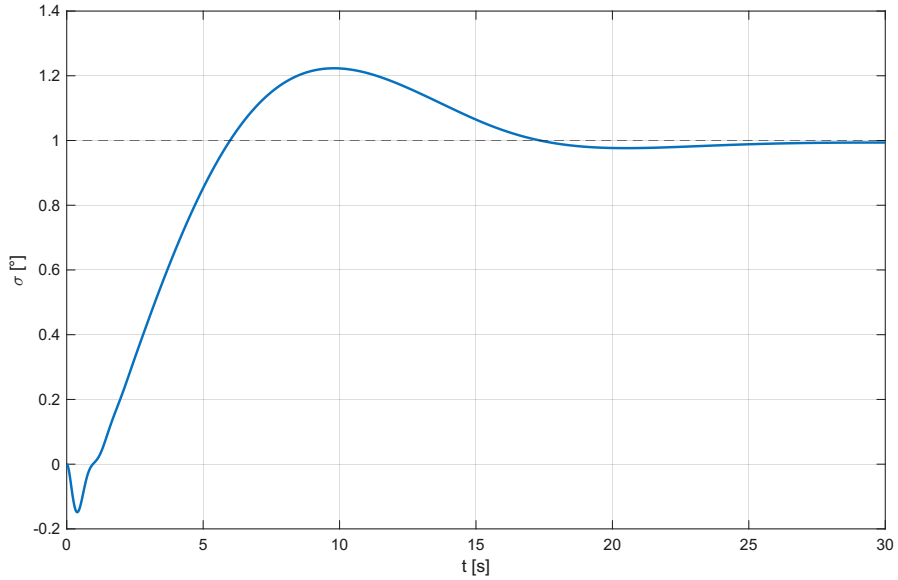

Figura 5.20: Step response at $t = 900\,\mathrm{s}$

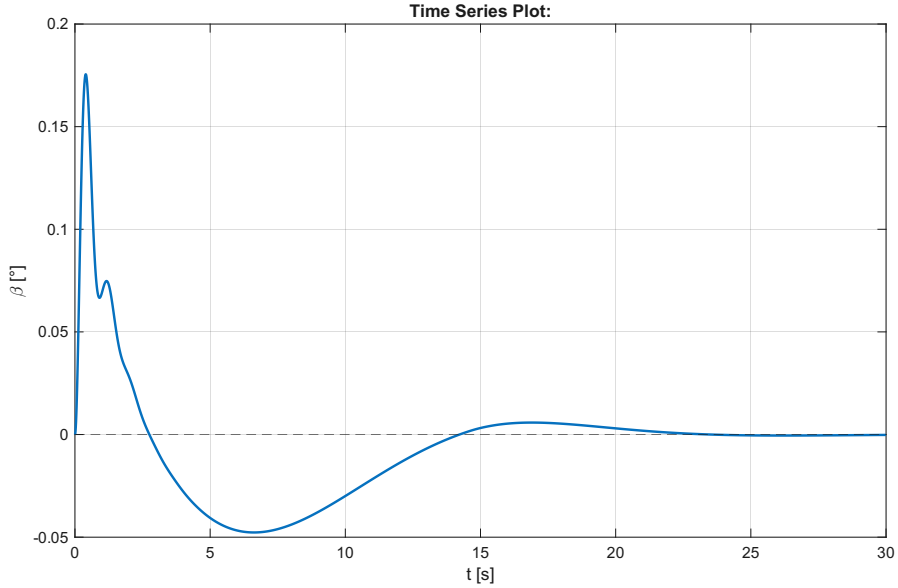

Figura 5.21: β response at $t = 900\,\mathrm{s}$

5.4 Results

In these sections, the complete nonlinear dynamic model of the vehicle is implemented. The full six–degree-of-freedom equations of motion are integrated, so that the closed-loop behaviour can be assessed along the entire reference trajectory. This allows one to verify the validity of the simplifying assumptions adopted in the linear analysis and to identify possible nonlinear effects, couplings, or actuator limitations that may degrade performance.

5.4.1 Constant control gains

It was observed that the gains taken directly from the linear analysis cannot be used as such for a gain-scheduled controller. In fact, the resulting control commands would be excessively aggressive, driving the system into the nonlinear regime that was intentionally neglected in the linear model, and causing the controller to diverge. In this first assessment, the gains were therefore fixed to constant values tuned by trial and error, while in the following section a variable-gain (scheduled) controller will be implemented, which provides superior performance. Consequently, the constant-gain controller presented in this section is included mainly to demonstrate that closed-loop control is feasible, although clearly not optimal.
The tuning process was iterative. As an initial guess, all gains were set equal to their values at the beginning of the trajectory. While this configuration provided acceptable performance in the early, high-altitude phase, it caused divergence in the final segment, where aerodynamic effects become dominant and the aerodynamic control surfaces can no longer be kept effectively inactive. The gains were then progressively modified, focusing on those values that triggered divergence in the first trials, until a compromise was found between stability, tracking performance, and control effort. The resulting gain configuration adopted in the following nonlinear simulations is reported in the table below. These are the gains selected for the controller; they are kept constant at these values over the entire trajectory. The corresponding time instants and dynamic pressures are reported only for completeness. Hence, as can be seen, a hybrid control strategy is adopted along the entire trajectory: throughout re-entry the aerodynamic surfaces and the RCS thrusters are used in synergy, in contrast with the approach adopted by Mooij. [3] (Fig.5.5)
The time histories reported in Figs. 3.2 and 5.23 show that the commanded angle of attack is tracked very closely and remains essentially equal to its nominal profile. Small spikes can be observed in the angle of attack; these are most likely associated with the instants in which a bank reversal is commanded. During these manoeuvres the elevons switch from a symmetric (elevator–like) to an asymmetric (aileron–like) configuration, so that the longitudinal control authority is temporarily reduced

before being rapidly recovered by the controller. Overall, we observe that the error in angle of attack ranges approximately between $+3^\circ$ and -1° (Fig.5.24). Moreover, we observe spikes in β as well, but the controller succeeds in cancelling the disturbance and driving the vehicle back to $\beta = 0$. Similar spikes are visible in the bank angle response, but their effect on the overall trajectory is limited, as evidenced by the ground track in Fig. 5.26, which closely follows the reference path. We also analyse the actuation of the aerodynamic surfaces and the RCS (Figs.5.27-5.28). Overall, the system is not subjected to persistently demanding commands but we have large oscillations; instead, the response is characterised by relatively steady behaviour with some peaks. In a more refined implementation, the continuous RCS torque commands should be shaped by an appropriate modulation scheme, such as Pulse-Width Pulse-Frequency (PWPF) modulation, while the sudden deflections of the aerodynamic surfaces should be passed through suitable actuator and command filters. This would smooth the control inputs and yield a more realistic representation of both jet firing patterns and surface motion, as expected in an actual flight control system.

Tabella 5.3: Controller gains and corresponding operating points.

Gain	Value	t (s)	q_{dyn} (N/m^2)
K_{e1}	-12.711	1000	4324.2
K_{e2}	-19.507	1000	4324.2
K_{y1}	1.02×10^6	50	19.01
K_{y2}	5.88×10^5	50	19.01
K_{ap}	-0.47481	1000	4324.2
K_{ar}	-14.416	1000	4324.2
K_{ab}	28.159	1000	4324.2
K_{as}	30.894	1000	4324.2
K_{rp}	-0.5524	1180	7329.4
K_{rr}	0.13557	1180	7329.4
K_{rb}	0.38057	1180	7329.4
K_{rs}	0.28242	1180	7329.4
K_{xp}	1.04×10^5	50	19.01
K_{xr}	11581	50	19.01
K_{xb}	27107	50	19.01
K_{xs}	-17231	50	19.01
K_{zp}	-40575	50	19.01
K_{zr}	1.01×10^6	50	19.01
K_{zb}	1.49×10^5	50	19.01
K_{zs}	-78755	50	19.01

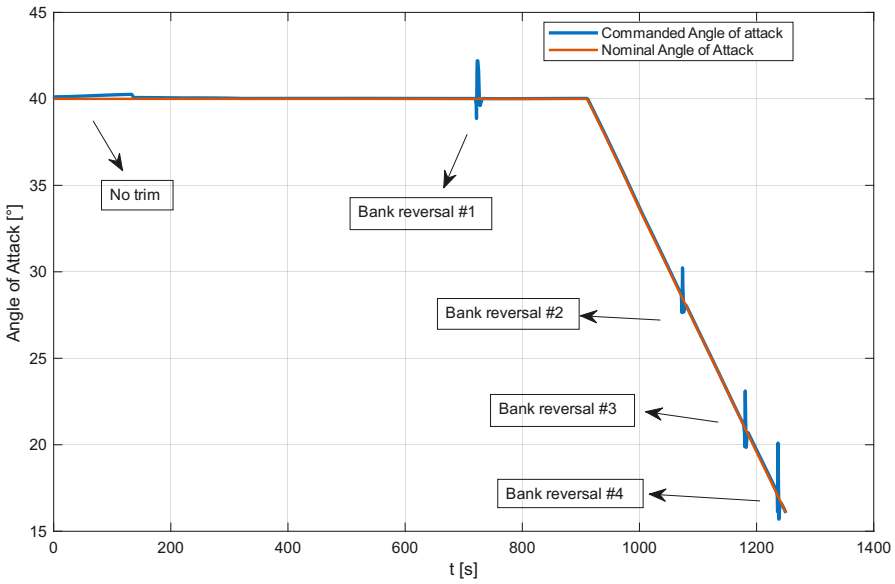

Figura 5.22: Commanded Angle of attack along the trajectory

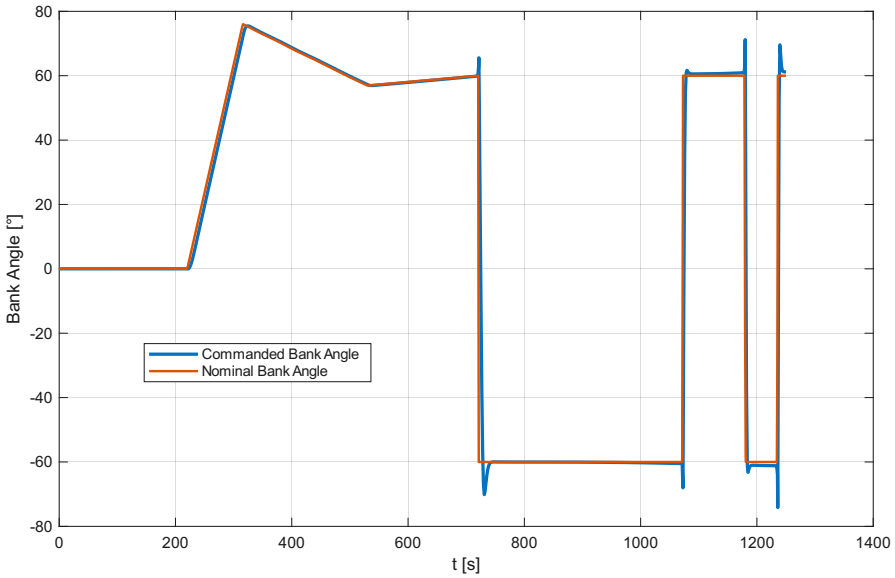

Figura 5.23: Commanded bank angle along the trajectory

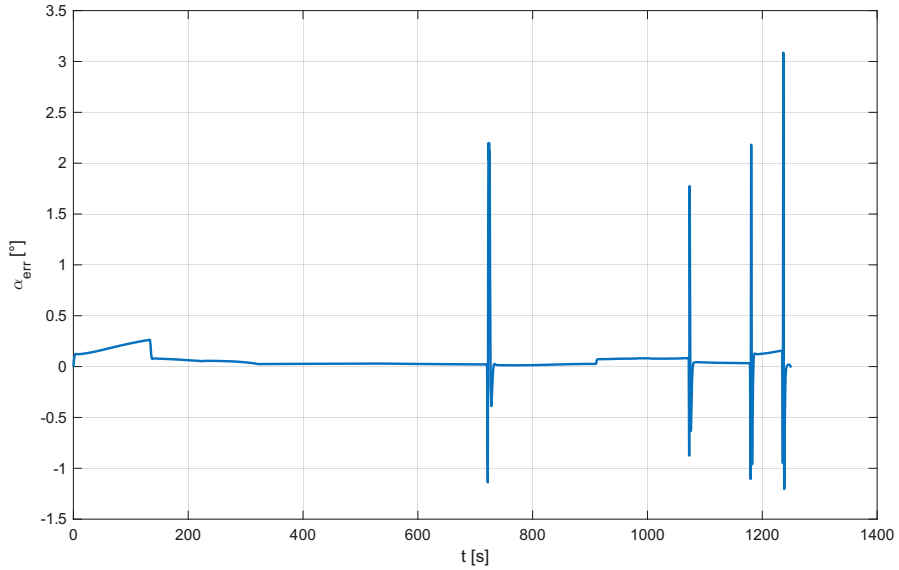

Figura 5.24: Angle of attack error along the nominal trajectory

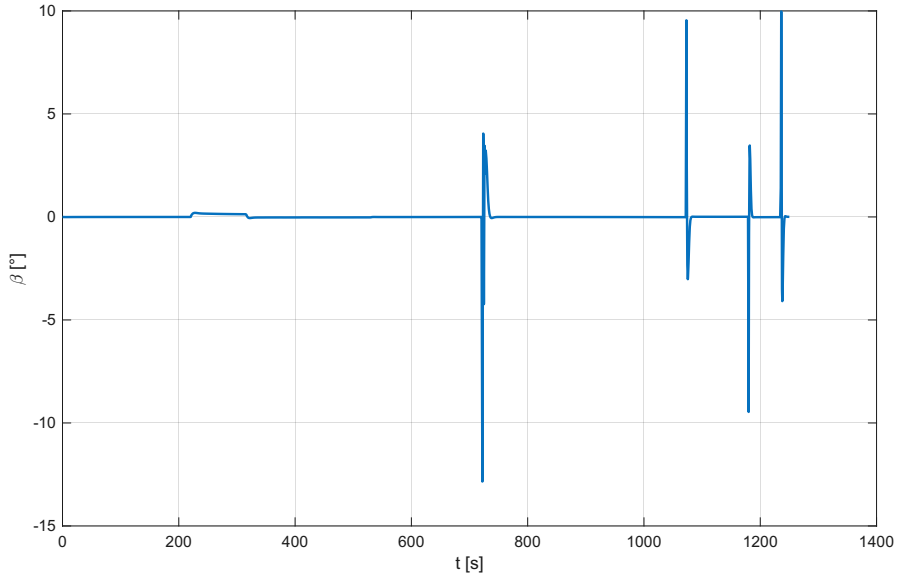

Figura 5.25: Angle of side slip along the nominal trajectory

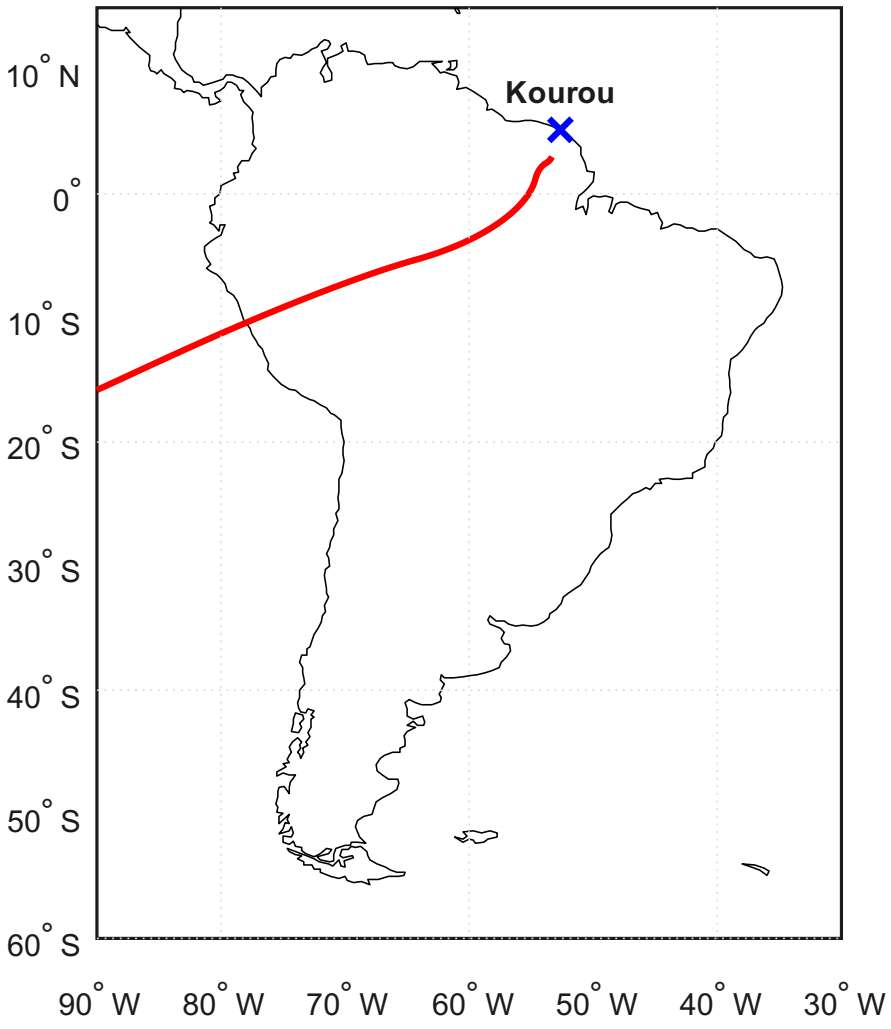

Figura 5.26: Vehicle ground track

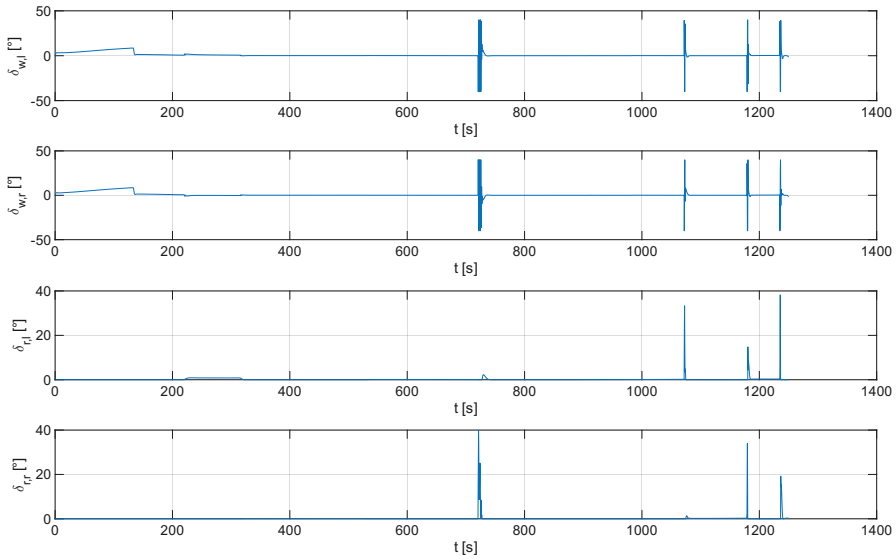

Figura 5.27: Surface deflection along the trajectory

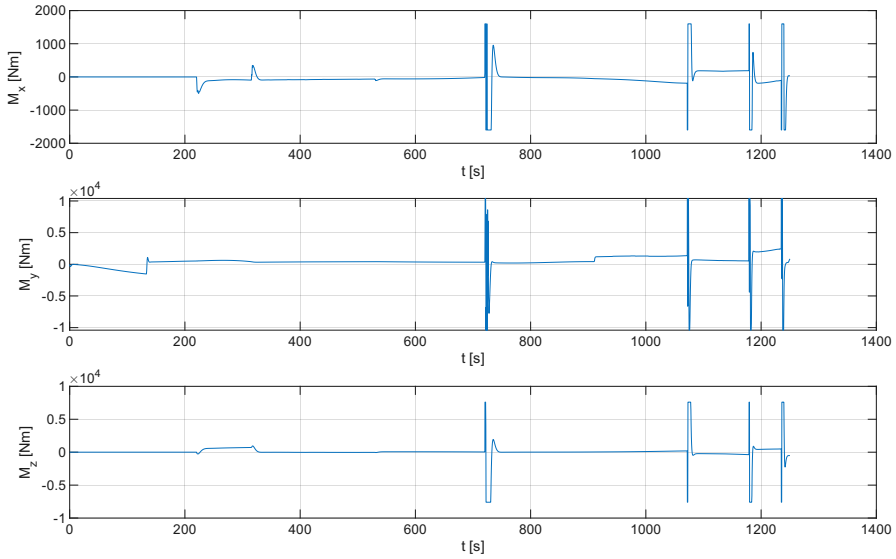

Figura 5.28: Reaction Control System along the trajectory

5.4.2 Gain scheduling

As discussed in the previous section, the use of constant feedback gains may provide acceptable performance, but it leads to overly aggressive control commands and does not yield an optimal solution. In particular, keeping the gains constant would require the RCS thrusters to be employed along the entire trajectory, resulting in an increased propellant requirement. In this section, trajectory-dependent gains computed a priori from the linearized model (gain scheduling) are implemented.

First, the weighting matrices Q and R had to be modified. For the longitudinal channel they were left unchanged, so the corresponding gains exhibit the same trends as in the previous section (Fig.5.6-5.7). Conversely, for the lateral–directional control a larger weight was assigned to the control-effort matrix R. Since the initial divergence of the controller was mainly caused by overly aggressive commands, the most natural place to intervene is precisely in R, by penalizing surface deflections more strongly so as to limit actuator activity and keep the response closer to the regime assumed in the linear model.
In particular, the R matrix of the lateral–directional controller takes the form

$$R = diag(1 \times 10^7 \cdot [1/\Delta\delta^2_{a,max},\ 1/\Delta\delta^2_{r,max},\ 1/\Delta M^2_{x,max},\ 1/\Delta M^2_{z,max}]) \qquad (5.30)$$

where all the coefficients have been scaled by a factor of 1×10^7.
Subsequently, it was found that this modification alone was sufficient to drive the vehicle along the desired commands; however, the response exhibited excessive jitter. This was mainly due to the aileron command still being somewhat too weak, while the rudder contribution was almost negligible and the RCS thrusters were effectively unused. The control inputs were therefore further rescaled, by trial and error, by the following factors:

$$\begin{aligned} K_{a,i} &= 50 \cdot K_{a,i} \\ K_{r,i} &= 1 \times 10^4 \cdot K_{r,i} \\ K_{x,i} &= 1 \times 10^5 \cdot K_{x,i} \\ K_{z,i} &= 1 \times 10^5 \cdot K_{z.i} \end{aligned}$$

with $i = [p,\ r,\ \beta,\ \sigma]$. As can be seen, the first step was to force the LQR controller to be very conservative with the control effort by scaling the R matrix by a large factor (Eq.5.30). The resulting gains were then increased again, since the initial penalization had effectively made the commands too "cheap" to be useful. A more balanced choice would probably have been to adopt slightly more aggressive commands from the outset, for instance by scaling R by a smaller factor, which might have avoided the need for this additional manual rescaling of the gains.

Nevertheless, this is the tuning process adopted in the present work, and since it leads to satisfactory performance (as shown in the following results), it has been retained in this form.
Finally, the resulting gains were parameterized with respect to the dynamic pressure. Since the trajectory provides the dynamic pressure as a function of time and the LQR design yields the gains as a function of time, the gains can be stored as functions of dynamic pressure and subsequently used for gain scheduling (Fig.5.29). To make the simulation more realistic, the aerodynamic control surfaces were modeled with both rate limiting ($20°/s$) and saturation, in accordance with the guidelines suggested by Mooij[3].

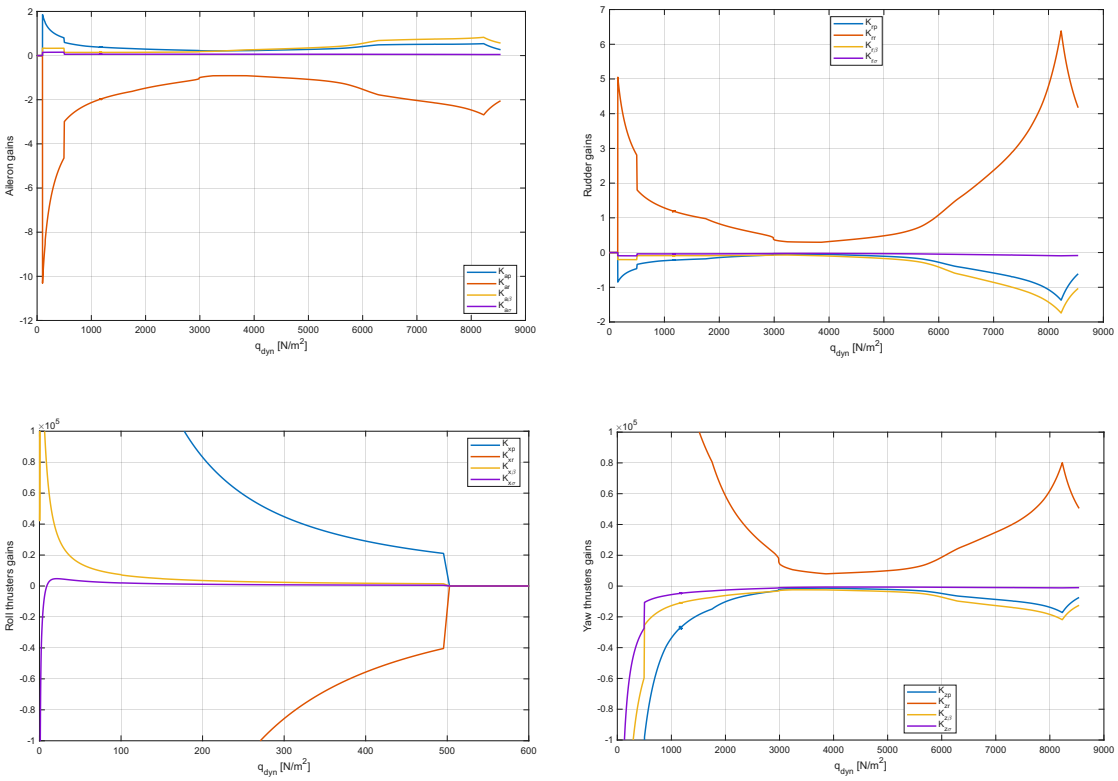

Figura 5.29: Lateral controller gains as function of dynamic pressure

As shown in Fig.5.30, the angle of attack is accurately tracked, while the bank angle exhibits a slight delay. Nevertheless, Fig.5.31 indicates that the errors remain small, on the order of 1.2° for the angle of attack, while for the bank angle we can see an error of higher magnitude (120°) because the reversals are made with some delay, but this won't affect the trajectory.
As can also be observed here, small spikes appear in the angle of attack, although with a smaller amplitude than in the constant–gain case. These spikes occur in correspondence with the bank reversals. The sideslip angle β is kept close to zero for most of the trajectory and is excited only during the bank reversals, after which it is driven back to zero with some oscillations. In terms of magnitude, the disturbance in β is reduced with respect to the constant–gain controller.

We also observe that the commanded surface deflections now have a smaller magnitude, which results in a smoother and more stable vehicle response. The moments generated by the RCS thrusters are likewise less aggressive, except in the initial phase, where the thrusters about the y- and z-axes briefly reach saturation. Furthermore, the roll and pitch thrusters are switched off in accordance with the scheduled gains and the evolution of the dynamic pressure, whereas the yaw thrusters remain available throughout the trajectory, since the Mach number never drops below unity.

Finally, Fig. 5.36 shows that the final destination, Kourou, is reached without difficulty.

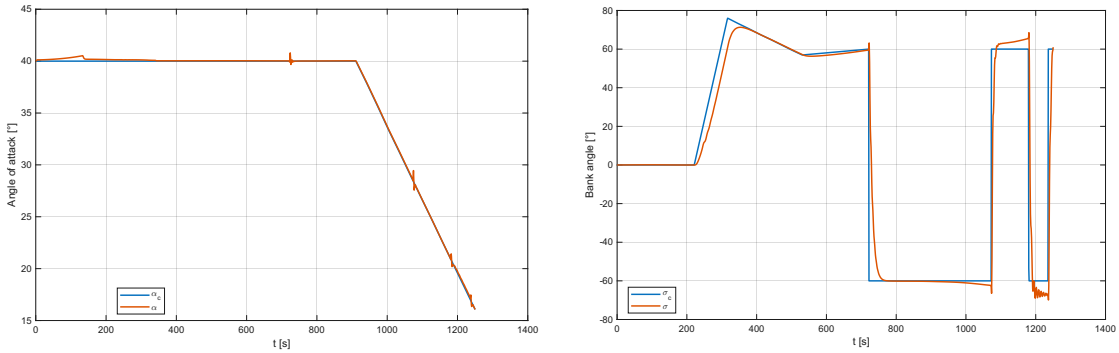

Figura 5.30: Angle of Attack and bank angle along the trajectory

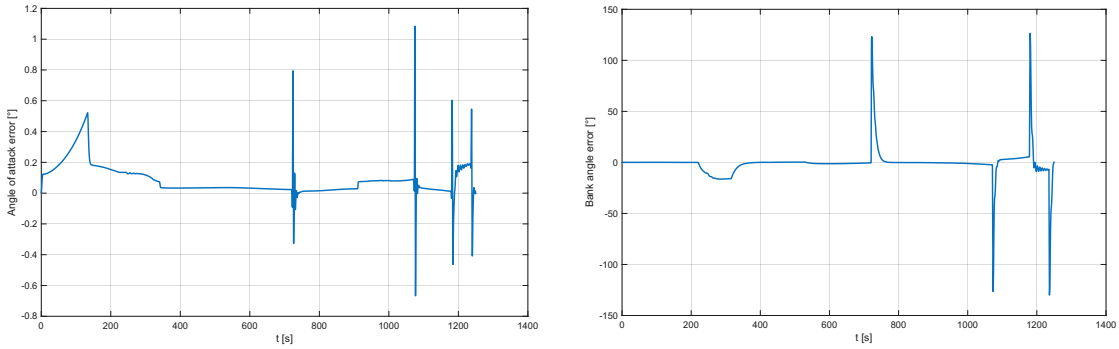

Figura 5.31: Angle of Attack error and bank angle error along the trajectory

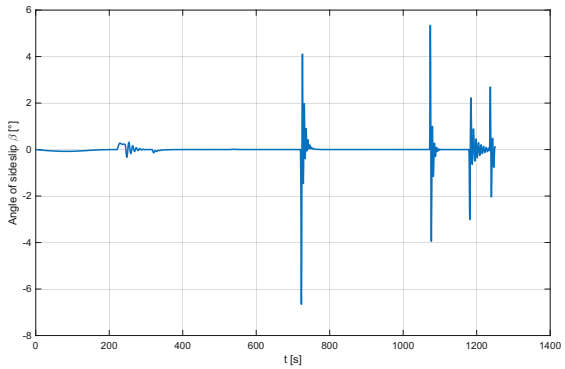

Figura 5.32: Angle of sideslip along the trajectory

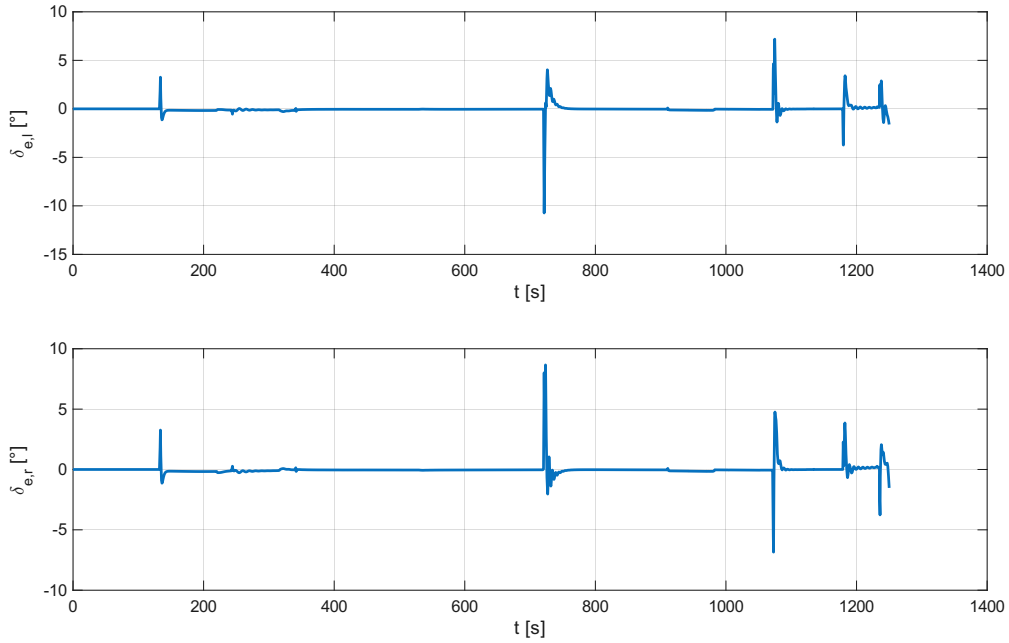

Figura 5.33: Elevons deflection along the trajectory

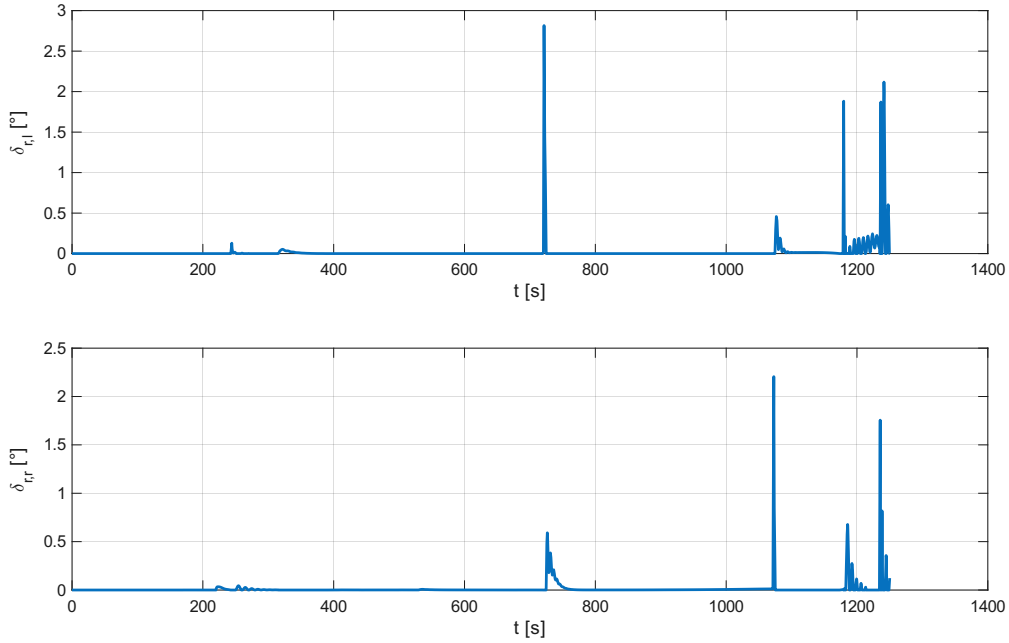

Figura 5.34: Rudders deflection along the trajectory

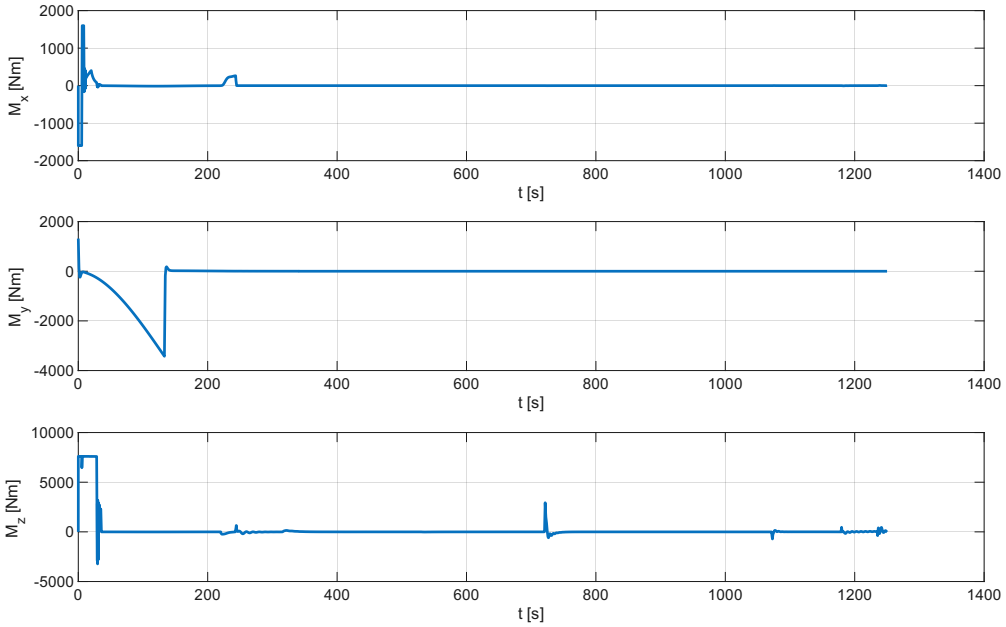

Figura 5.35: RCS Thrusters along the trajectory

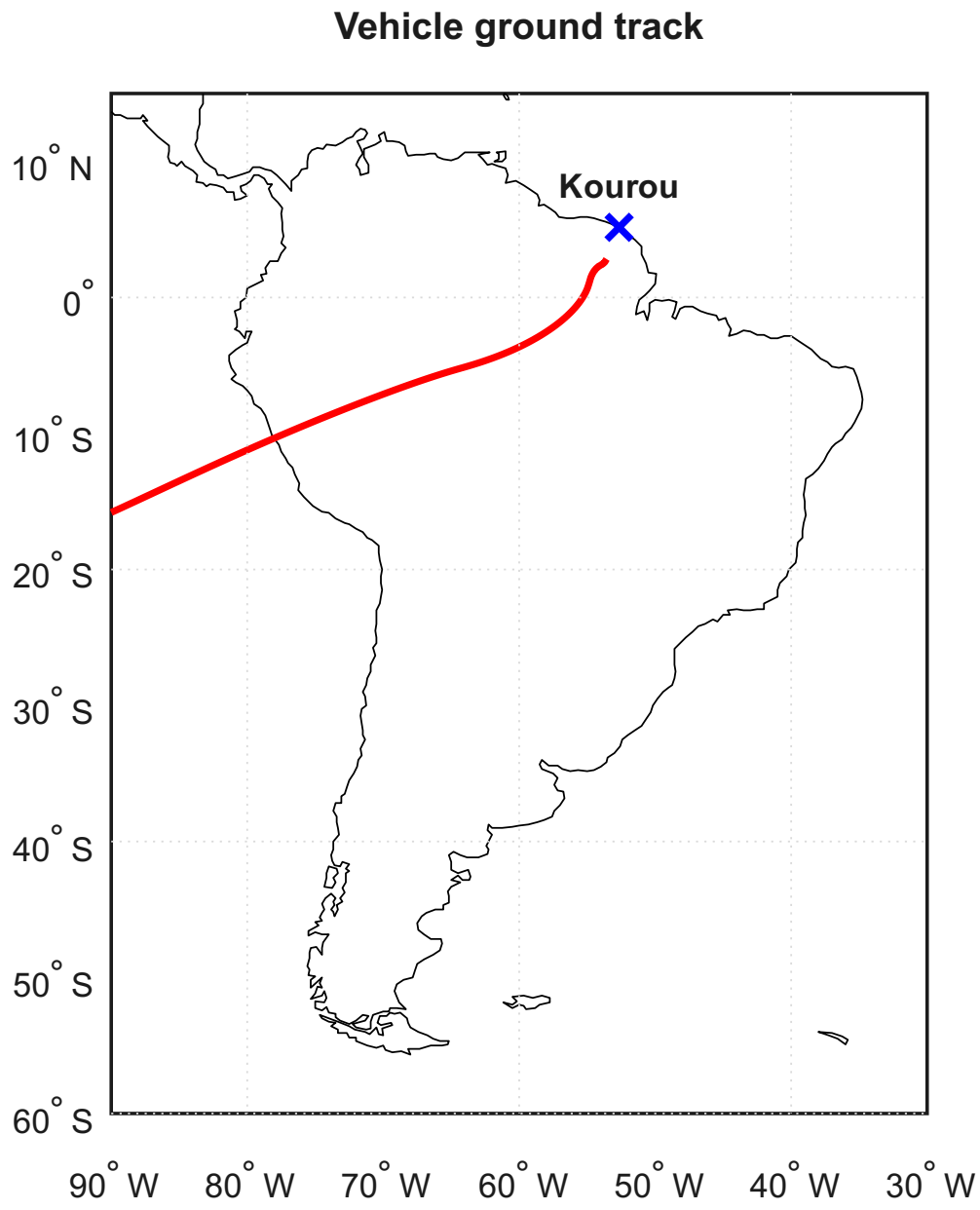

Figura 5.36: Vehicle ground tracking

Capitolo 6

Conclusions

This thesis has investigated the lateral–directional stability and control of a hypersonic re-entry vehicle, using the HORUS-2B configuration as reference. Starting from a well-established mission profile towards Kourou, a comprehensive analysis framework has been developed, ranging from open-loop mode identification to the implementation of literal approximations and the design of an LQR-based attitude controller embedded in a full 6-DOF simulation.

In the first part of the work, the open-loop dynamic behaviour of HORUS-2B has been characterised along the reference re-entry trajectory. The evolution of the main longitudinal and lateral–directional modes has been analysed, highlighting those regions where the vehicle approaches critical stability margins or exhibits strong coupling between roll, yaw, and sideslip dynamics.

The central contribution of this thesis has been the implementation and evaluation of literal (closed-form) approximations of the lateral-directional modes and longitudinal modes originally developed for aircraft operating in more conventional flight regimes. These approximations have been adapted to the specific geometry and hypersonic operating conditions of HORUS-2B, and then quantitatively compared with the "exact" eigenstructure obtained from the linearised 6-DOF model along the trajectory. Within the range of conditions where their underlying assumptions remain valid, the literal models have shown a good capability to reproduce the qualitative behaviour and, in many cases, the quantitative trends of the full system. This suggests that, when used carefully, such approximations can serve as useful tools for preliminary design, parametric studies, and the formulation of departure criteria for Shuttle-class and Space-Rider-class vehicles. At the same time, the analysis has also clarified their limitations, in particular in those regions where strong cross-coupling and rapid parameter variations violate the simplifying hypotheses.

In the final part of the thesis, an LQR-based attitude controller has been designed for the reference vehicle, following the general control architecture previously proposed in the literature but adopting an alternative tuning and scheduling of the feedback gains. Although the controller explicitly targets attitude variables, its performance has been assessed within a fully non-linear 6-DOF simulation. The resulting vehicle ground track confirms that, under the adopted assumptions and modelling choices, the controlled vehicle is able to follow the reference mission and reach the vicinity of Kourou, thereby linking the attitude-control design to tangible trajectory- and mission-level outcomes.

Overall, the work carried out in this thesis demonstrates that literal approximations, when properly adapted and validated, can provide a compact and insightful representation of hypersonic lateral-directional and longitudinal dynamics, complementing more detailed numerical models. The LQR-based attitude control study shows that relatively simple linear techniques, embedded in a suitable gain-scheduling framework, can still play a significant role in the guidance and control of modern reusable re-entry vehicles. Nonetheless, the results should be interpreted in the light of the simplifying assumptions adopted, in particular regarding aerodynamic modelling, actuator dynamics, and the absence of model uncertainty and disturbances in the control design.

6.1 Future works

Future work should first address the main limitation of the present analysis, namely the lack of reliable aerodynamic damping derivatives in the model. In this thesis these derivatives were set to zero, which is acceptable for a first-order assessment but becomes critical when applying literal approximations to the dynamic modes and to departure criteria, where damping terms play a central role in determining modal damping and wing–rock onset.[6] A natural extension would therefore be to obtain consistent estimates of the damping derivatives—either from high-fidelity CFD and forced-oscillation wind-tunnel campaigns to re-evaluate the literal approximations and stability margins for HORUS-2B in the relevant hypersonic regime. In parallel, the LQR attitude controller should be exercised in a more realistic environment by introducing actuator and surface-deflection dynamics (rate limits, position limits and appropriate filters such as PWPF for the RCS), as well as sensor noise and trajectory perturbations modelled through Monte-Carlo campaigns; this would allow a statistical assessment of robustness and a more faithful representation of the closed-loop 6-DOF behaviour. Finally, a systematic parametric study of mass properties, with particular emphasis on centre-of-gravity location, should be

performed to quantify its impact on trim, body-flap deflection and available control authority. Since trim strategy directly modifies the effective flight condition on the Bihrle–Weissman diagram[8] and can introduce non-trivial lateral–directional control-coupling effects, as recently highlighted for the Space Shuttle Orbiter, an analogous analysis for HORUS-2B would clarify how sensitive its departure boundaries and handling qualities are to CG shifts and alternative pitch-trim solutions.

Appendice A

Eigenmotion results

In the following tables the eigenmotion main characteristics of the vehicle are reported.

λ_i	Short-period oscillation		Phugoid		Lateral oscillation		Aperiodic roll modes		Height mode
Re	$-9.2491e-08$		$3.9638e-05$		$8.8016e-04$		$-1.7604e-03$	$-3.1190e-19$	$-8.2686e-05$
Im	$7.2299e-03$		$1.2129e-03$		$1.7307e-02$		–	–	–
P (s)	869.05		5180.1		363.04		∞	∞	∞
$T_{1/2}$ (s)	$7.4942e+06$		-17487		-787.52		393.75	$2.2223e+18$	8382.8
ζ (–)	$1.2793e-05$		-0.032662		-0.05079		–	–	–
ω_n (rad/s)	0.0072299		0.0012136		0.017329		––	––	––
$\boldsymbol{\mu_i}$	z	θ (°)	z	θ (°)	z	θ (°)	z	z	z
ΔV	0.0105	56.3714	0.0013	-1.1604	0.0000	-3.2285	0.0000	0.0000	0.0007
$\Delta\gamma$	0.0000	-88.8341	0.0000	89.5987	0.0000	-34.7483	0.0000	0.0000	0.0000
ΔR	0.9997	0	1.0000	0	0.0000	-14.0133	0.0000	0.0000	1.0000
Δp	0.0000	-78.7837	0.0000	14.6665	0.0171	84.0822	0.0022	0.0008	0.0000
Δq	0.0001	62.2814	0.0000	-13.0250	0.0000	-4.7477	0.0000	0.0000	0.0000
Δr	0.0000	-56.4521	0.0000	86.4048	0.0014	84.0822	0.0002	0.0010	0.0000
$\Delta\alpha$	0.0202	-27.7172	0.0000	5.9171	0.0000	88.7277	0.0000	0.0000	0.0000
$\Delta\beta$	0.0000	33.5486	0.0000	43.4686	0.5829	-8.8291	0.0075	0.0000	0.0000
$\Delta\sigma$	0.0000	9.0043	0.0000	45.9907	0.8123	0	1.0000	1.0000	0.0000

Tabella A.1: HORUS eigenvalues and corresponding characteristic values for time point 1 ($t = 5\,\mathrm{s}$).

λ_i	Short-period oscillation		Phugoid		Lateral oscillation		Aperiodic Roll mode		Height mode
Re	$-5.3615e-05$		$-1.8155e-04$		$8.8295e-04$		$-1.8008e-03$	$-1.8466e-17$	$1.4312e-04$
Im	0.17917		$1.2844e-03$		0.40565		–	–	–
P (s)	35.069		4891.9		15.489		∞	∞	∞
$T_{1/2}$ (s)	12928		3817.9		-785.03		384.92	$3.7536e+16$	-4843.3
ζ (–)	$2.9924e-04$		0.13996		$-2.1766e-03$		–	–	–
ω_n (rad/s)	0.17917		0.0012972		0.40566		–	–	–
$\boldsymbol{\mu_i}$	z	θ (°)	z	θ (°)	z	θ (°)	z	z	z
ΔV	0.2729	88.5546	0.0013	8.7379	0.0000	-88.4558	0.0000	0.0000	0.0006
$\Delta\gamma$	0.0000	-89.9340	0.0000	-80.7978	0.0000	89.8002	0.0000	0.0000	0.0000
ΔR	0.9617	0	1.0000	0	0.0000	89.5820	0.0000	0.0000	1.0000
Δp	0.0000	0.8716	0.0000	0.5903	0.3747	89.7569	0.0022	0.0008	0.0000
Δq	0.0045	88.7348	0.0000	-25.8441	0.0000	-89.3471	0.0000	0.0000	0.0000
Δr	0.0000	0.8716	0.0000	0.5903	0.0302	89.7569	0.0002	0.0010	0.0000
$\Delta\alpha$	0.0249	-1.2310	0.0000	8.7494	0.0000	-0.7940	0.0000	0.0000	0.0000
$\Delta\beta$	0.0000	0.8716	0.0000	0.5903	0.5366	-0.3678	0.0000	0.0000	0.0000
$\Delta\sigma$	0.0000	0.8716	0.0000	0.5903	0.7555	0	1.0000	1.0000	0.0000

Tabella A.2: HORUS eigenvalues and corresponding characteristic values for time point 50 ($t = 196\,\mathrm{s}$).

λ_i	Short-period oscillation		Phugoid		Lateral oscillation		Periodic Roll divergence		Height/Spiral mode
Re	$-2.9118e-04$		$-1.0027e-03$		$2.5617e-04$		$6.6490e-05$		$-1.8370e-16$
Im	0.40565		$1.3683e-03$		0.91843		$5.5494e-04$		–
P (s)	15.489		4591.9		6.8413		11322		∞
$T_{1/2}$ (s)	2380.5		691.28		-2705.8		-10425		$3.7732e+15$
ζ (–)	$7.1781e-04$		0.59108		$-2.7893e-04$		-0.11896		–
ω_n (rad/s)	0.40565		0.0016964		0.91843		0.00055891		–
$\boldsymbol{\mu_i}$	z	θ (°)	z	θ (°)	z	θ (°)	z	θ (°)	z
ΔV	0.8761	0	0.0017	43.6477	0.0063	0.1698	0.0006	58.7925	0.0000
$\Delta\gamma$	0.0000	1.5839	0.0000	-53.6558	0.0001	89.9849	0.0000	83.2143	0.0000
ΔR	0.4806	-88.4713	1.0000	0	0.8904	0	1.0000	0	1.0000
Δp	0.0000	0.1983	0.0000	-32.4381	0.3069	-89.9745	0.0000	31.2391	0.0000
Δq	0.0144	-0.1245	0.0000	62.6002	0.0001	0.1187	0.0000	-43.7505	0.0000
Δr	0.0000	0.1983	0.0000	-32.4381	0.0248	-89.9745	0.0000	31.2391	0.0000
$\Delta\alpha$	0.0354	89.9575	0.0000	43.6452	0.0005	-89.8750	0.0000	58.7892	0.0000
$\Delta\beta$	0.0000	-89.7606	0.0000	-86.2044	0.1941	0.0096	0.0000	-65.5931	0.0000
$\Delta\sigma$	0.0000	-77.6792	0.0000	29.4287	0.2733	0.0391	0.0000	-45.6694	0.0000

Tabella A.3: HORUS eigenvalues and corresponding characteristic values for time point 100 ($t = 396\,\mathrm{s}$).

λ_i	Short-period oscillation		Phugoid		Lateral oscillation		Height/Spiral mode			
Re	$-3.3571e-04$		$-1.1062e-03$		$4.6200e-04$		$2.5078e-04$	$-5.3349e-04$		$-7.4602e-15$
Im	0.41292		$1.5594e-03$		0.93489		–	–		–
P (s)	15.216		4029.3		6.7208		∞	∞		∞
$T_{1/2}$ (s)	2064.7		626.6		-1500.3		-2763.9	1299.3		$9.2912e+13$
ζ (–)	$8.1300e-04$		0.57859		$-4.9417e-04$		–	–		–
ω_n (rad/s)	0.41292		0.0019119		0.93489		–	–		–
$\boldsymbol{\mu_i}$	z	θ (°)	z	θ (°)	z	θ (°)	z	z		z
ΔV	0.7819	0	0.0018	44.6782	0.0069	0.2203	0.0002	0.0009		0.0000
$\Delta\gamma$	0.0000	1.1043	0.0000	-54.3917	0.0001	89.9740	0.0000	0.0000		0.0000
ΔR	0.6225	-88.9583	1.0000	0	0.8699	0	1.0000	1.0000		1.0000
Δp	0.0000	0.2867	0.0000	-39.0428	0.3357	-89.9826	0.0000	0.0000		0.0000
Δq	0.0128	-0.1209	0.0000	71.0657	0.0001	0.1687	0.0000	0.0000		0.0000
Δr	0.0000	0.2867	0.0000	-39.0428	0.0271	-89.9826	0.0000	0.0000		0.0000
$\Delta\alpha$	0.0310	89.9719	0.0000	44.6759	0.0005	-89.8343	0.0000	0.0000		0.0000
$\Delta\beta$	0.0000	-89.6667	0.0000	86.3085	0.2086	-0.0110	0.0000	0.0000		0.0000
$\Delta\sigma$	0.0000	-63.6786	0.0000	23.5622	0.2937	0.0533	0.0000	0.0000		0.0000

Tabella A.4: HORUS eigenvalues and corresponding characteristic values for time point 150 ($t = 596\,\mathrm{s}$).

λ_i	Short-period oscillation		Phugoid		Lateral oscillation		Periodic Roll		Height/Spiral Mode
Re	$-1.2103e-03$		$-2.6360e-03$		$3.8613e-04$		$-7.1901e-05$		$9.0316e-16$
Im	0.73214		$2.0702e-03$		1.4799		$1.0771e-03$		–
P (s)	8.5819		3035		4.2456		5833.5		∞
$T_{1/2}$ (s)	572.73		262.95		-1795.1		9640.3		$-7.6747e+14$
ζ (–)	0.001653		0.78645		$-2.6092e-04$		0.066607		–
ω_n (rad/s)	0.73214		0.0033518		1.4799		0.0010795		–
$\boldsymbol{\mu_i}$	z	θ (°)	z	θ (°)	z	θ (°)	z	θ (°)	z
ΔV	0.9220	0	0.0025	86.6201	0.0082	0.3362	0.0005	78.2106	0.0000
$\Delta\gamma$	0.0001	0.6939	0.0000	-37.9075	0.0002	89.9876	0.0000	-86.1335	0.0000
ΔR	0.3858	-89.4161	1.0000	0	0.8293	0	1.0000	0	1.0000
Δp	0.0000	0.2012	0.0000	-60.2373	0.4614	-89.9208	0.0000	6.9412	0.0000
Δq	0.0188	-0.2739	0.0000	-79.2781	0.0001	0.2204	0.0000	-35.4305	0.0000
Δr	0.0000	0.2012	0.0000	-60.2373	0.0380	-89.9208	0.0000	6.9412	0.0000
$\Delta\alpha$	0.0257	89.8739	0.0000	86.6178	0.0004	-89.7621	0.0000	78.2075	0.0000
$\Delta\beta$	0.0000	-89.7041	0.0000	81.6178	0.1807	0.0643	0.0000	-79.2396	0.0000
$\Delta\sigma$	0.0000	-44.8041	0.0000	-61.3829	0.2553	0.0651	0.0000	-27.5094	0.0000

Tabella A.5: HORUS eigenvalues and corresponding characteristic values for time point 200 ($t = 796\,\mathrm{s}$).

λ_i	Short-period oscillation		Phugoid		Lateral oscillation			Height/Spiral	
Re	-0.0010947		-0.0024088		0.0018081		-0.0098543	-0.0016234	$-1.0526e-14$
Im	0.47606		0.0018583		1.4753		–	–	–
P (s)	13.198		3381.2		4.2589		∞	∞	∞
$T_{1/2}$ (s)	633.17		287.76		-383.35		70.339	426.97	$6.5849e+13$
ζ (–)	0.0022996		0.79177		-0.0012256		–	–	–
ω_n (rad/s)	0.47606		0.0030423		1.4753		–	–	–
$\boldsymbol{\mu_i}$	z	θ (°)	z	θ (°)	z	θ (°)	z	z	z
ΔV	0.7921	0	0.0009	-47.9520	0.0118	0.6206	0.0100	0.0004	0.0000
$\Delta\gamma$	0.0001	1.3319	0.0000	-37.5458	0.0005	89.9462	0.0000	0.0000	0.0000
ΔR	0.6103	-88.9221	1.0000	0	0.9433	0	1.0000	1.0000	1.0000
Δp	0.0000	0.4337	0.0000	-56.0907	0.2721	89.9799	0.0000	0.0000	0.0000
Δq	0.0048	-1.4245	0.0000	-13.5359	0.0001	0.1553	0.0000	0.0000	0.0000
Δr	0.0000	0.4337	0.0000	-56.0907	0.0358	89.9799	0.0000	0.0000	0.0000
$\Delta\alpha$	0.0102	89.4325	0.0000	-47.9532	0.0003	-89.6003	0.0000	0.0000	0.0000
$\Delta\beta$	0.0000	-89.4345	0.0000	86.2605	0.0829	-0.0903	0.0000	0.0000	0.0000
$\Delta\sigma$	0.0000	-27.9168	0.0000	34.0775	0.1666	-0.0034	0.0000	0.0000	0.0000

Tabella A.6: HORUS eigenvalues and corresponding characteristic values for time point 250 ($t = 996\,\mathrm{s}$).

λ_i	Former Short-period		Phugoid		Lateral oscillation		Height		
Re	-0.8011	0.73236	-0.018269		0.023486		0.014822	-0.00010996	$-4.9178e-15$
Im	–	–	0.010809		1.0698		–	–	–
P (s)	∞	∞	581.27		5.8733		∞	∞	∞
$T_{1/2}$ (s)	0.86524	-0.94645	37.942		-29.513		-46.765	6303.4	$1.4095e+14$
ζ (–)	–	–	0.86063		-0.021949		–	–	–
ω_n (rad/s)	–	–	0.021227		1.07		–	–	–
$\boldsymbol{\mu_i}$	z	z	z	θ (°)	z	θ (°)	z	z	z
ΔV	0.5866	0.5608	0.0074	-5.6742	0.0175	1.2962	0.0136	0.0001	0.0001
$\Delta\gamma$	0.0005	0.0005	0.0000	-29.7864	0.0010	88.8373	0.0000	0.0000	0.0000
ΔR	0.8096	0.8277	1.0000	0	0.9945	0	0.9999	1.0000	1.0000
Δp	0.0000	0.0000	0.0000	-79.4899	0.0746	87.2728	0.0000	0.0000	0.0000
Δq	0.0128	0.0118	0.0000	-83.2276	0.0002	3.2005	0.0000	0.0000	0.0000
Δr	0.0000	0.0000	0.0000	-79.4899	0.0134	87.2728	0.0000	0.0000	0.0000
$\Delta\alpha$	0.0171	0.0150	0.0000	-5.7864	0.0003	89.9803	0.0000	0.0000	0.0000
$\Delta\beta$	0.0000	0.0000	0.0000	69.8975	0.0119	-3.9849	0.0000	0.0000	0.0000
$\Delta\sigma$	0.0001	0.0001	0.0000	-65.2260	0.0698	-1.5089	0.0000	0.0000	0.0000

Tabella A.7: HORUS eigenvalues and corresponding characteristic values for time point 300 ($t = 1{,}196\,\mathrm{s}$).

λ_i	Former Short-period		Phugoid		Lateral oscillation		Height		
Re	-1.012	0.86726	-0.022021		0.03921		0.050527	-0.00014497	$3.7727e-16$
Im	–	–	0.013327		1.2821		–	–	–
P (s)	∞	∞	471.46		4.9008		∞	∞	∞
$T_{1/2}$ (s)	0.68493	-0.79924	31.476		-17.678		-13.718	4781.4	$-1.8373e+15$
ζ (–)	–	–	0.85553		-0.030569		–	–	–
ω_n (rad/s)	–	–	0.02574		1.2827		–	–	–
$\boldsymbol{\mu_i}$	z	z	z	θ (°)	z	θ (°)	z	z	z
ΔV	0.6950	0.6474	0.0055	-18.5345	0.0280	1.6123	0.0526	0.0000	0.0000
$\Delta\gamma$	0.0008	0.0008	0.0000	-30.7376	0.0017	88.4632	0.0001	0.0000	0.0000
ΔR	0.7186	0.7619	1.0000	0	0.9889	0	0.9986	1.0000	1.0000
Δp	0.0000	0.0000	0.0000	-80.9396	0.1149	86.6969	0.0000	0.0000	0.0000
Δq	0.0168	0.0140	0.0000	49.3462	0.0003	6.1426	0.0000	0.0000	0.0000
Δr	0.0000	0.0000	0.0000	-80.9396	0.0078	86.6969	0.0000	0.0000	0.0000
$\Delta\alpha$	0.0183	0.0146	0.0000	-18.6084	0.0005	89.9603	0.0001	0.0000	0.0000
$\Delta\beta$	0.0000	0.0000	0.0000	67.8783	0.0190	-5.0548	0.0000	0.0000	0.0000
$\Delta\sigma$	0.0002	0.0003	0.0000	-77.7289	0.0878	-1.5576	0.0001	0.0000	0.0000

Tabella A.8: HORUS eigenvalues and corresponding characteristic values for time point 350 ($t = 1{,}250\,\mathrm{s}$).

Bibliografia

[1] Connor S. Hoopes e Timothy T. Takahashi. «Lateral-Directional Controllability Impacts of Longitudinal Pitch Trim Strategies on the Space Shuttle Orbiter». In: *AIAA SCITECH 2024 Forum*. DOI: 10.2514/6.2024-2318. eprint: https://arc.aiaa.org/doi/pdf/10.2514/6.2024-2318. URL: https://arc.aiaa.org/doi/abs/10.2514/6.2024-2318 (cit. alle pp. 2, 3, 49–51).

[2] Erwin Mooij. «The Horus-2B reference vehicle». In: *Delft University of Technology, Faculty of Aerospace Engineering, memorandum m-692* (mag. 1995) (cit. a p. 3).

[3] Erwin Mooij. *Re-entry Systems*. English. Springer Aerospace Technology. Springer, 2024. ISBN: 978-3-031-62173-4. DOI: 10.1007/978-3-031-62174-1 (cit. alle pp. 4, 5, 7–10, 12–14, 17, 19, 21, 32, 35, 38, 39, 42, 43, 62, 70, 76, 84).

[4] Erwin Mooij. «Linear quadratic regulator design for an unpowered, winged re-entry vehicle». In: *Delft University of Technology, Faculty of Aerospace Engineering, Report LR-806* (dic. 1997) (cit. alle pp. 4, 15, 16, 21, 32, 42, 43, 56, 58).

[5] N.X. Vinh. «OPTIMAL TRAJECTORIES IN ATMOSPHERIC FLIGHT». In: *Space Mankind's Fourth Environment*. A cura di L.G. NAPOLITANO. Pergamon, 1982, pp. 449–468. ISBN: 978-0-08-028708-9. DOI: https://doi.org/10.1016/B978-0-08-028708-9.50036-1. URL: https://www.sciencedirect.com/science/article/pii/B9780080287089500361 (cit. a p. 10).

[6] N. Ananthkrishnan e Suraj Unnikrishnan. «Literal Approximations to Aircraft Dynamic Modes». In: *Journal of Guidance, Control, and Dynamics* 24.6 (2001), pp. 1196–1203. DOI: 10.2514/2.4835. eprint: https://doi.org/10.2514/2.4835. URL: https://doi.org/10.2514/2.4835 (cit. alle pp. 44, 47, 48, 91).

[7] Aircraft Flight Mechanics. *Nondimensional Stability Derivatives*. https://www.aircraftflightmechanics.com/Linearisation/Nondimensional.html (cit. a p. 46).

[8] Timothy Takahashi, Jack Griffin e Ramana Grandhi. «High-Speed Aircraft Stability and Control Metrics». In: *Aerospace* 12 (dic. 2024), p. 12. DOI: 10.3390/aerospace12010012 (cit. alle pp. 52, 92).